ANL-IFR-149

Integral Fast Reactor Program Annual Progress Report FY 1990

Argonne National Laboratory, Argonne, Illinois 60439
operated by The University of Chicago
for the United States Department of Energy under Contract W-31-109-Eng-38

Argonne National Laboratory, with facilities in the states of Illinois and Idaho, is owned by the United States government, and operated by The University of Chicago under the provisions of a contract with the Department of Energy.

May 1991 ANL-IFR-149

INTEGRAL FAST REACTOR PROGRAM
ANNUAL PROGRESS REPORT
FY 1990

Argonne National Laboratory
9700 South Cass Avenue
Argonne, IL 60439

Y. I. Chang	General Manager, IFR Program
L. C. Walters	Director, Fuels and Processing Division
J. E. Battles	Associate Director, Chemical Technology Division
D. R. Pedersen	Associate Director, Reactor Engineering Division
D. C. Wade	Director, Reactor Analysis Division
M. J. Lineberry	Director, Fuel Cycle Facility Division

IFR TECHNICAL MEMORANDUM NO. 149

TABLE OF CONTENTS

TABLE OF CONTENTS
(Contd.)

TABLE OF CONTENTS
(Contd.)

LIST OF FIGURES

LIST OF FIGURES
(Contd.)

LIST OF FIGURES
(Contd.)

LIST OF TABLES

INTEGRAL FAST REACTOR
ANNUAL PROGRESS REPORT
FY 1990

ABSTRACT

This report summarizes highlights of the technical progress made in the Integral Fast Reactor (IFR) Program in FY 1990. Technical accomplishments are presented in the following areas of the IFR technology development activities: (1) metal fuel performance, (2) pyroprocess development, (3) safety experiments and analyses, (4) core design development, (5) fuel cycle demonstration, and (6) LMR technology R&D.

I. IFR PROGRAM OVERVIEW

The Integral Fast Reactor (IFR) development covers the entire reactor system, not only the reactor itself, but also its fuel cycle, both fuel refining and fabrication, and waste management as well. The goal is to develop a reactor system that answers the questions facing the next generation of nuclear power plants with respect to economics, safety, and waste disposal. As such, the program emphasis has shifted each year as the development has proceeded.

Initially, the focus was placed on demonstration of passive safety characteristics. The loss-of-flow without scram and loss-of-heat-sink without scram tests at EBR-II were a spectacular demonstration of the inherent passive safety potential of the IFR concept. The emphasis then shifted to development of a fuel performance and pyroprocessing technology data base, and a rapid progress has been made during the past year.

The high burnup potential of the new IFR fuel alloys has been demonstrated. EBR-II is now fully converted with the IFR fuel alloys and statistically significant fuel performance data are being generated. A new whole-pin furnace experimental facility was installed during the past year, which permits in-depth evaluation of fuel failure mechanisms over a broad range of temperatures and transient conditions to establish the safety data base required for licensing. Electrorefining experiments are routinely carried out on a 10-kg engineering scale. Anodic dissolution was successfully demonstrated during the past year, speeding dissolution, which had previously slowed the rates in the IFR pyroprocesses.

The focus is now on the demonstration of the entire IFR fuel cycle. The next key milestone is to complete the refurbishment of the original EBR-II Fuel Cycle Facility. During the past year all environmental permit processes have been successfully completed. Rapid progress is being made on the facility modifications as well as the fabrication of process equipment modules. The initial startup testing is scheduled to begin in October 1991.

Completing the technology development phase, the IFR Program is now entering Phase III, the demonstration phase. The demonstration phase will be

completed by the end of FY 1995. Priority during this phase will be given to the following tasks:

- Completion of Fuel cycle Facility refurbishment and subsequent operation for prototype demonstration of the entire IFR fuel cycle.

- Conceptual design of commercial-scale fuel cycle facility.

- Development of waste processing technology and initiation of the NRC certification process.

- Fuel performance demonstration of recycled IFR fuel alloys up to 15% burnup.

- Development of safety licensing data base and demonstration tests at EBR-II, as required.

During the past year, a new R&D effort was spun off. In IFR pyroprocessing, minor actinides accompany the plutonium product stream. Therefore, actinide recycling occurs naturally in the IFR. A logical question is whether the pyroprocessing approach can be extended to extract actinides from LWR spent fuel. And, in fact, it turns out that there is an extensive experience base at Argonne in applying pyrochemical processes to oxide fuel.

In the late 1960s, the EBR-II Fuel Cycle Facility operated for about five years using a simple drossing process, known as melt refining. In this process the electropositive fission products were separated from the fuel by reaction with a zirconium oxide crucible. The volatile elements were released and collected on a fume trap or condensed cryogenically from the cell atmosphere.

A pyrochemical process for recovering the actinides occluded with the dross, or crucible skull, was developed and demonstrated on the engineering scale with simulated fuel. This skull reclamation process employed liquid zinc-magnesium and molten chloride salt as process solvents. Also a blanket process for recovery of plutonium from metallic uranium blankets was demonstrated on a bench scale. This process involved the selective extraction of plutonium from molten uranium into an immiscible magnesium phase.

The techniques developed to process EBR-II skulls and blankets were then extended to processing uranium oxide and mixed oxide fast reactor fuels. Rapid methods for reducing these dense oxide fuels were demonstrated, and a liquid metal-fused salt extraction step was developed for isolating the uranium, plutonium, and fission products. This "salt transport process" was demonstrated on a laboratory scale, but funding was terminated before a planned pilot plant demonstration could be completed.

The earlier pyrochemical process development efforts were discontinued because there was no clear advantage to producing a pure plutonium product stream over the traditional Purex process. Today, however, the processing goal has changed. In traditional reprocessing based on Purex, the goal was to produce a highly decontaminated, pure Pu product stream. However, when LWR processing is viewed as a waste management strategy, the goal is quite different. Neither a pure Pu product stream nor a high decontamination factor is required. In fact, just the opposite is desirable. The new process goals, when LWR spent fuel processing is viewed as a waste management strategy, are as follows:

- Direct extraction of all actinides (Pu, Np, Am, Cm, etc.) from the spent fuel as a single product stream.

- An actinide recovery target of 99.9% to 99.99%.

- The process should be incapable of producing pure Pu product.

- The process should be incapable of achieving a high decontamination factor for fission products.

- The process should be simple enough to achieve acceptable economics.

A preliminary assessment has been made to investigate the feasibility of using pyrochemical processes for directly extracting actinides from LWR spent fuel, satisfying the new process goals discussed above. It appears that the pyrochemical processes are exactly compatible with the new process goals and two promising flowsheet options have been identified: (1) a salt transport process and (2) a magnesium extraction process.

The pyrochemical processes fit naturally to the LWR actinide extraction application and should provide significant advantages over the traditional Purex-based processes.

First, potentially all actinide elements are extracted in a single product stream, along with most rare earth fission products. A pure plutonium product is not possible. The product is highly radioactive and is not much more attractive than the original spent fuel as far as the diversion risk is concerned. The process as such therefore provides some nonproliferation protection.

Second, in these processes uranium remains as metal ingots with some noble fission product contamination. In this form the uranium can be easily stored for later recovery and use in the IFRs. The actinide extraction processes deal with only 1 or 2% of the total heavy metal. This small mass flow and the few process steps involved lead to compact equipment systems and small facility size, and portend favorable economics.

A small-scale R&D program has been initiated to develop the necessary data base to judge technical feasibility of the proposed flowsheets by the end of FY 1995.

II. METAL FUEL PERFORMANCE

A. Steady-state U-Pu-Zr Fuel Performance to >15 at.% Burnup

1. Introduction

The four lead IFR subassemblies (X419, X420, X421, and X425) each consisted of 61 elements ~63.8 cm (~25.1 in.) long which were clad in the austenitic alloy 20% cold-worked D9 (X419, X420, and X421) or in HT9 (X425), a martensitic stainless steel. Each subassembly contained a complement of U-xPu-10Zr fuel (where x = 0, 8, and 19 wt %). The fuel slugs were one piece solid cylinders 34.3 cm (13.50 in.) long x 0.434 cm (0.171 in.) in diameter, irradiated in the as-injection-cast condition.

The elements were sodium bonded at ~500°C (932°F) for no less than 1 h. The cladding outer diameter was 0.584 cm (0.230 in.) with a 0.381 mm (0.015 in.) wall thickness. The as-built fuel to plenum volume ratio was approximately unity. A 0.107 cm (0.042 in.) diameter spacer wire was welded to each end plug with a 15.24 cm (6.0 in.) pitch. The closure welds were of the TIG type. Each experiment bore a unique tag gas mixture to aid in breach identification. The beginning-of-life peak inside cladding temperatures ranged from ~540°C (1004°F) to ~590°C (1094°F) in the four bundles. The three fuel types were suitably enriched in U-235 to operate in the range of ~377 W/cm to 475 W/cm (~11.5 kW/ft to ~14.5 kW/ft).

2. Fuel Swelling and Fission Gas Release

Interlinkage of gas bubbles and rapid gas release at 1 to 2 at.% burnup mitigates fuel-clad mechanical interaction because the porous fuel is so plastically compliant at temperature. Radial fuel growth dominates the swelling process; at ~2 at.% burnup cladding contact causes frictional forces to impede further axial growth. The initial apparent anisotropy has been related to radial gradients in creep strength and irradiation growth of non-cubic phases in the fuel.[1]

At high burnup (between 15 and 18 at.% burnup) a gap between fuel (especially U-19Pu-10Zr) and cladding tends to reestablish itself near core midplane due to the high swelling nature of the austenitic, D9 cladding at this fluence. Note that the cladding strain in HT9-clad fuel is much less at high burnup, and a gap is therefore less likely to form. Axial growth is an approximately linear function of burnup beyond 2 at.% burnup. Figure II.1 shows the average length change as a function of peak burnup in the three fuel types. The 19% Pu fuel shows the greatest degree of anisotropy, due in part to fuel slug cracking which accompanies constituent redistribution during the free-swelling regime below 2 at.% burnup.

The molar quantity of fission gas released to the plenum is nearly linear with burnup. As a consequence, at high burnup the fractional release asymptotically approaches 80% of that generated. This behavior can be seen in Fig. II.2 for the three alloys tested. Consistent with its higher axial growth, and therefore greater volumetric swelling, the binary alloy shows slightly higher rates of gas release beyond about 10 at.% burnup.

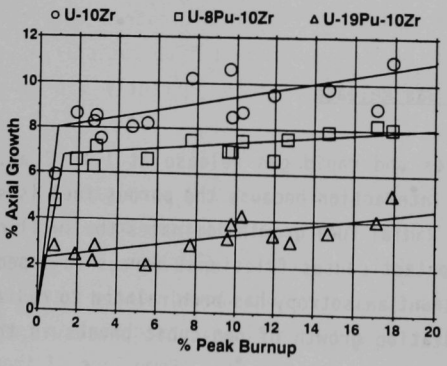

Fig. II.1. Burnup Dependence of the Average Axial Fuel Elongation

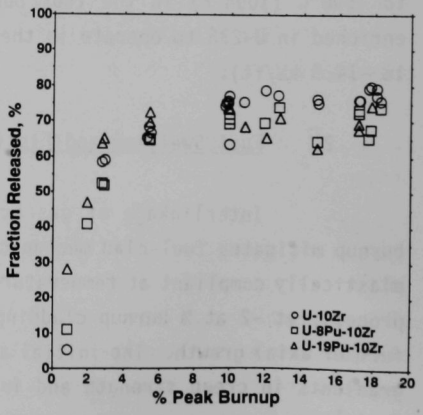

Fig. II.2. Burnup Dependence of the Fission Gas Release Fraction

3. Cladding Performance

The 20% cold-worked D9 cladding performed satisfactorily to the peak exposure reached (~19x 10^{22} n/cm^2 fast fluence). Peak diametral strain (creep plus swelling) ranged from an average of ~1% at 10 at.% burnup to 7% at 18 at.% burnup as shown in Fig. II.3. Because fuel/cladding mechanical interaction is minimized by the low planar smeared density, the high fuel-to-plenum volume ratio promotes fission gas loading as the principal source of stress. The LIFE-METAL fuel performance computer code was fairly successful in predicting the cladding response in spite of the uncertainties of in-reactor operating conditions, and the fact that high fluence swelling and creep correlations for this heat of steel are not particularly well-defined. These predictions are shown in Fig. II.4 for the case of U-10Zr fuel.

As asserted above, fuel/clad mechanical interaction was found to contribute little to the total creep strain at the burnup levels modeled for the D9-clad elements. For the high burnup case, LIFE-METAL predicted that ~80% of the total strain is due to creep, and 20% due to swelling. Post-irradiation examinations of the high burnup fuel from X420 and X421 are continuing and will serve to benchmark the LIFE-METAL code predictions with immersion density measurements to derive cladding swelling values.

The cladding strain for HT9-clad elements was ~1% at 16 at.% burnup, presumably all produced by creep. In terms of the large neutron fluences expected for innovative reactor designs, where fluence-to-burnup ratios can be >3 x 10^{22} n x cm^2/% burnup, the martensitic cladding is currently the only option.

Fuel-clad chemical interaction in D9-clad was most prominent at the hotter elevations of the elements and at 17 at.% to 18 at.% burnup took the form of a non-uniform transgranular layer <0.1 mm deep. Electron microprobe examinations of sibling fuel at 5 at.% to 10 at.% burnup showed nearly complete depletion of nickel (from ~16 wt % to ~1 wt %) and significant enrichment in rare earth fission products (~23 wt % of Nd, Ce, Sm, Pr, and La). Some loss of iron had also occurred but no change in chromium content was found. This layer was extremely hard with low ductility at hot-cell temperatures and was about three

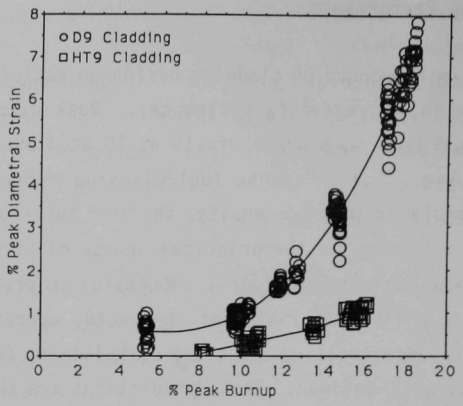

Fig. II. 3. Burnup Dependence of the Maximum Cladding Strain in the Experimental Fuel Elements

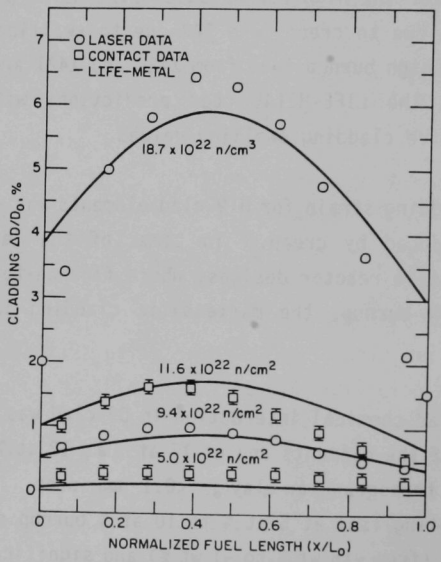

Fig. II.4. Comparison between LIFE-METAL Predictions and Data for Cladding Diametral Strain Profiles at Peak Burnups of 5.4 at.%, 9.7 at.%, 11.8 at.%, and 17.9 at.%

times deeper in the 19% plutonium fuel than the binary fuel. The migration of the rare-earth fission products is enhanced in the coarse porosity of the ternary alloys and tends to agglomerate near the cladding inner surface within pre-existing cavities. Two major rare-earth phases have been observed, differing mainly in their palladium content. Their approximate compositions (wt %) at 17 at.% burnup are: a) 33 Nd, 24 La, 18 Ce, 16 Pd, 4 Pr, 3 Pu, and 2 U; and b) 34 Nd, 28 Ce, 28 La, 6 Pu, and 4 Pr.

The chemical interactions which have been observed between U-Pu-Zr and HT9 cladding have been less extensive and more difficult to characterize. The enhancement of interaction at high burnup will be investigated during the next year, but is also not expected to be as prevalent as the swelling of cladding away from the fuel should not occur with HT9, and therefore fission products will have less space to accumulate.

4. Chemical Redistribution

Multiphase boundaries present in the fuel during operation lead to annular zones which differ in swelling properties and composition, most prominent in the 19% Pu fuel.[2] By 2 at.% burnup, an interchange between zirconium and uranium occurs. Depending on fuel temperatures, this leaves either a zirconium-depleted shell (<2 wt %) at mid-radius surrounding a zirconium-rich core or a zirconium-depleted nugget at slug center encircled by zirconium-rich fuel. Wedge-shaped cracks seen in transverse sections are common at the earliest stages of redistribution but are completely "healed" by fuel growth by 10 at.% burnup. Little redistribution occurs in the other alloys at low burnup. Preliminary electron microprobe data on U-19Pu-10Zr fuel at 18 at.% burnup showed the typical three-zone structure. The central zone had approximately (wt %) 14% Pu, 16% Zr (remainder U and fission products). This region was surrounded by a shell with 11% Pu, and only 4% Zr. The outermost region was particularly inhomogeneous with typical compositions of 18% Pu and 24% Zr. A qualitative analysis of a U-10Zr fuel slug at 18% burnup showed a factor of 2 higher in zirconium content at slug centerline vs. fuel surface.

B. Fuel/Cladding Compatibility in Irradiated Metallic Fuel Pins at Elevated Temperatures

More than 50 fuel/cladding compatibility tests on irradiated metallic fuel specimens have been conducted in an in-cell facility at elevated temperatures. At temperatures below 700-725°C, no fuel/cladding interaction was noted in tests of up to 7.0 h. Liquid-phase cladding penetration occurred in some of the tests at temperatures above 725-750°C. The effective rates of liquid-phase cladding penetration of six different fuel/cladding combinations during 1.0-h testing are reported. After the initial liquefaction at the fuel/cladding interface, which may be affected by solid-state diffusional interaction during steady-state irradiation, the rate of further cladding penetration remained constant or decreased with time. There was no runaway cladding penetration in the latter part of the heating cycle.

The U and Pu constituents in the metallic fuel, and the rare-earth fission products generated during irradiation can interact metallurgically with the stainless steel cladding at elevated temperatures.[3,4] During steady-state irradiation, solid-state interdiffusion may occur across the fuel/cladding interface. If the fuel element is then subjected to a high-temperature, off-normal reactor event, the interdiffusion layers on the fuel and the inside surface of the cladding may liquefy, thus dissolving additional fuel and causing liquid-phase penetration into the cladding. To assess the effects of such interactions on the performance reliability of IFR fuel elements under off-normal reactor conditions, it is necessary to determine a) the temperature above which liquid-phase cladding penetration would occur and b) the rate of such penetration into the cladding.

This section summarizes the ongoing experimental effort to study the compatibility between the irradiated metallic fuel and cladding at elevated temperatures. An underlying objective of the work has been to support the development of driver fuels for the Experimental Breeder Reactor-II (EBR-II) and the PRISM advanced liquid metal reactor concept.[5] Currently, the driver fuel for the EBR-II is U-10 wt % Zr binary alloy clad in either 316, D9 or HT9 stainless steels; that for the PRISM design is a U-26 wt % Pu-10 wt % Zr fuel clad in HT9 steel.

1. Experimental

All of the data presented in this section were generated in an in-cell facility called the fuel behavior test apparatus (FBTA).[6] The specimens used in the tests were obtained from fuel elements irradiated under steady-state conditions in EBR-II.

A quad-elliptical radiant furnace, powered by four longitudinal infrared filaments, heats the specimen isothermally. The test specimen is usually a short section of an irradiated fuel element placed inside a slightly taller tantalum cup. Shaped and highly reflective surfaces behind the filaments focus the radiant energy onto the centerline of the furnace, where the specimen cup is located. A single, bare-wire Pt/Pt-Rh thermocouple welded onto the outside of the specimen cup monitors the specimen temperature. The output from the thermocouple is used to control the furnace, via a microcomputer and a feedback algorithm, to maintain the desired test temperature. Due to the negligible thermal inertia of the infrared filaments and the strong focusing of the radiant energy, the specimen is typically heated to the desired test temperature in less than 1 min. Because heat is externally provided to the specimen, once the desired test temperature is reached, no significant radial temperature gradient exists in the fuel or the cladding.

After the test, the specimen is metallographically examined to collect evidence of fuel/cladding interaction and to determine the maximum depth of cladding penetration. From the collected data, the liquid-phase-formation temperature and the maximum cladding penetration rates are derived. Selected specimens are further examined with a shielded electron microprobe and scanning electron microscope (SEM) to delineate the constituent distribution in phases formed in the fuel/cladding interaction zone.

2. Test Results and Discussion

More than 50 tests have been conducted on U-26Pu-10Zr/316SS, U-19Pu-10Zr/HT9, U-19Pu-10Zr/D9, U-10Zr/HT9, U-10Zr/D9 and U-10Zr/316SS specimens. Fuel burnups were between 3 and 17 at.%. All tests are of the constant-temperature

type; the temperature and duration of the tests ranged from 700 to 850°C and 0.1 to 7.0 h, respectively. The test matrix is given in Table II.1.

3. Types of Fuel/Cladding Interaction

At temperatures below ~700-725°C, no liquid-phase fuel/cladding interaction was observed in FBTA tests of up to 7.0 h. In the temperature range of ~725-750°C, solid-state diffusional interaction was occasionally noted, mostly in low-burnup fuel with austenitic stainless steel cladding (Type-316 and D9). The reaction resulted in an austenitic-to-ferritic transformation due to the loss of Ni to the fuel. The diffusion of Cr and Fe away from the cladding matrix was not as noticeable. Diffusion of fuel components, including fission products, into the cladding also appeared to be relatively slow. A section of the Type-316 stainless steel cladding that incurred diffusional reaction after the 88-27 test (740°C for 7.0 h) is shown in Fig. II.5. Hardness measurements inferred no significant loss of ductility in the affected cladding.

At temperatures of ~725°C and above, interaction between fuel and cladding may result in liquid-phase cladding penetration. Two types of such interaction, i.e., grain boundary penetration and matrix dissolution, have been found. Liquid-phase grain boundary penetration occurs predominantly in high-burnup fuel. Figure II.6 shows a section of the D9 cladding from the 90-01 test affected by grain boundary interaction. The liquid phase on the cladding grain boundary consists mainly of the fission product lanthanides, i.e., La, Pr, Nd, and Ce. The content of fuel constituents U and Pu in the liquid phase was minor. Cladding grains surrounded by the liquid phase appear to undergo an austenitic-to-ferritic transformation. Diffusion of Fe into the fuel matrix appears to be minor. Currently, no FBTA test data are available on high-burnup fuels with HT9 cladding.

In lower-burnup fuels, cladding penetration in the form of matrix dissolution prevailed. The dissolved cladding components, mainly Fe (and Ni in the case of austenitic cladding steel), reacted with the fuel and caused fuel liquefaction. Figure II.7 shows a transverse section of the U-10Zr/HT9 specimen after the 800°C, 1.0-h test, 88-04. A section of the reacted cladding, in the as-polished condition, is shown in Fig. II.8. The reacted cladding is brittle

TABLE II.1. FBTA Compatibility Test Matrix

Test No.	Fuel/Cladding	Pin No.	EBR-II Assembly	Peak Burnup (a/o)	Axial Loc. X/L	Test Temp. (°C)	Test Time (h)
87-74	U-19Pu-10Zr/HT9	T459	X425	3	0.69	700	1.0
87-75	U-19Pu-10Zr/HT9	T459	X425	3	0.71	750	1.0
87-76	U-19Pu-10Zr/HT9	T459	X425	3	0.74	780	1.0
88-01	U-10Zr/HT9	T437	X425	3	0.85	800	1.0
88-02	U-10Zr/HT9	T437	X425	3	0.87	850	1.0
88-03	U-10Zr/HT9	T437	X425	3	0.89	750	1.0
88-04	U-10Zr/HT9	T437	X425	3	0.46	800	1.0
88-05	U-10Zr/HT9	T437	X425	3	0.48	750	1.0
88-06	U-10Zr/HT9	T437	X425	3	0.52	700	1.0
88-13	U-10Zr/HT9	T437	X425	3	0.56	725	1.0
88-07	U-10Zr/D9	T224	X420	6	0.93	800	1.0
88-08	U-10Zr/D9	T224	X420	6	0.91	750	1.0
88-09	U-10Zr/D9	T224	X420	6	0.89	725	1.0
88-11	U-10Zr/D9	T248	X421	10	0.76	750	1.0
88-12	U-10Zr/D9	T248	X421	10	0.78	800	1.0
88-14	U-10Zr/D9	T248	X421	10	0.74	800	1.0
88-15	U-10Zr/HT9	T619	X429	8	0.46	800	1.0
88-16	U-10Zr/HT9	T619	X429	8	0.55	800	0.5
88-17	U-10Zr/HT9	T619	X429	8	0.23	800	2.0
88-18	U-10Zr/HT9	T619	X429	8	0.20	800	1.0
88-19	U-10Zr/HT9	T619	X429	8	0.25	800	0.5
88-20	U-10Zr/HT9	T619	X429	8	0.27	800	0.1
88-21	U-10Zr/HT9	T619	X429	8	0.30	800	0.2
88-22	U-26Pu-10Zr/316	T326	X423	5	0.54	700	1.0
88-23	U-26Pu-10Zr/316	T326	X423	5	0.60	750	1.0
88-24	U-26Pu-10Zr/316	T326	X423	5	0.57	800	1.0
88-25	U-26Pu-10Zr/316	T326	X423	5	0.45	670	7.0
88-26	U-26Pu-10Zr/316	T326	X423	5	0.63	850	1.0
88-27	U-26Pu-10Zr/316	T326	X423	5	0.48	740	7.0
88-28	U-26Pu-10Zr/316	T326	X423	5	0.40	710	7.0
89-01	U-26Pu-10Zr/316	T326	X423	5	0.42	770	7.0
89-02	U-10Zr/316SS	T536	X421	9	0.48	800	1.0
89-03	U-10Zr/316SS	T536	X421	9	0.52	850	1.0
89-04	U-10Zr/316SS	T536	X421	9	0.45	750	1.0
89-05	U-10Zr/316SS	T323	X423	5	0.55	800	1.0
89-06	U-10Zr/316SS	T323	X423	5	0.52	750	1.0
89-08	U-10Zr/316SS	T323	X423	5	0.45	850	1.0
89-13	U-10Zr/316SS	T323	X423	5	0.58	800	0.4
89-14	U-10Zr/316SS	T323	X423	5	0.61	800	0.2
89-15	U-10Zr/316SS	T323	X423	5	0.64	800	2.0
89-16	U-10Zr/316SS	T323	X423	5	0.67	800	4.0
89-09	U-26Pu-10Zr/316	T326	X423	5	0.70	800	1.0
89-10	U-26Pu-10Zr/316	T326	X423	5	0.73	800	2.0
89-11	U-26Pu-10Zr/316	T326	X423	5	0.78	800	4.0
89-12	U-26Pu-10Zr/316	T326	X423	5	0.80	800	0.4
90-01	U-19Pu-10Zr/D9	T106	X421	17	0.50	750	1.0
90-02	U-19Pu-10Zr/D9	T106	X421	17	0.87	750	1.0
90-03	U-19Pu-10Zr/D9	T106	X421	17	0.84	800	1.0
90-04	U-10Zr/D9	T227	X421	17	0.51	800	1.0
90-05	U-10Zr/D9	T227	X421	17	0.87	800	1.0
90-06	U-10Zr/D9	T227	X421	17	0.53	800	1.0
90-07	U-10Zr/D9	T227	X421	17	0.82	750	1.0
90-08	U-10Zr/D9	T227	X421	17	0.78	725	1.0
90-09	U-10Zr/D9	T227	X421	17	0.75	800	0.5
90-10	U-10Zr/D9	T227	X421	17	0.73	725	7.0

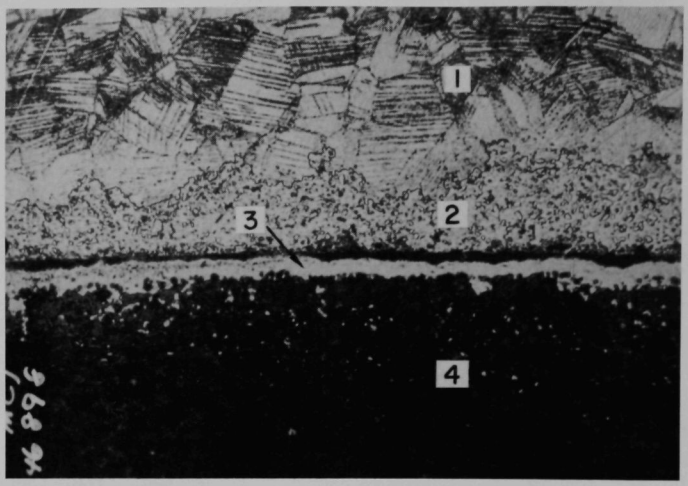

Fig. II.5. Diffusional Interaction in Type-316 Stainless Steel Cladding: (1) Intact Cladding, (2) Affected Cladding, (3) Zr-rich Surface Layer on Fuel from Fabrication, (4) Etched Fuel. (Etched, 525X.)

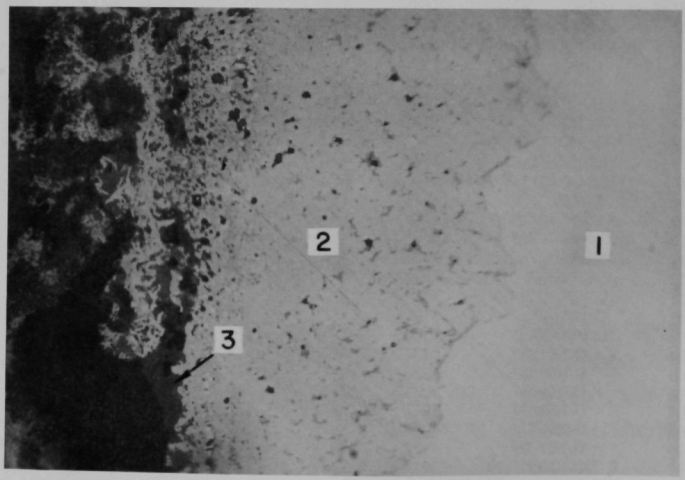

Fig. II.6. Liquid-phase Boundary Penetration in D9 Cladding from Test 90-01: (1) Intact Cladding, (2) Reacted Cladding, (3) Lanthanide Fission Products. (As-polished, 500X.)

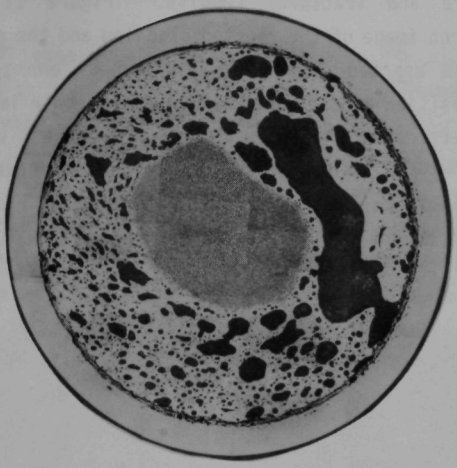

Fig. II.7. Transverse Section of the U-10Zr/HT9 Specimen after the 88-04 Test (800°C, 1.0 h). Note fuel liquefaction except in the center. (As-polished, 26X.)

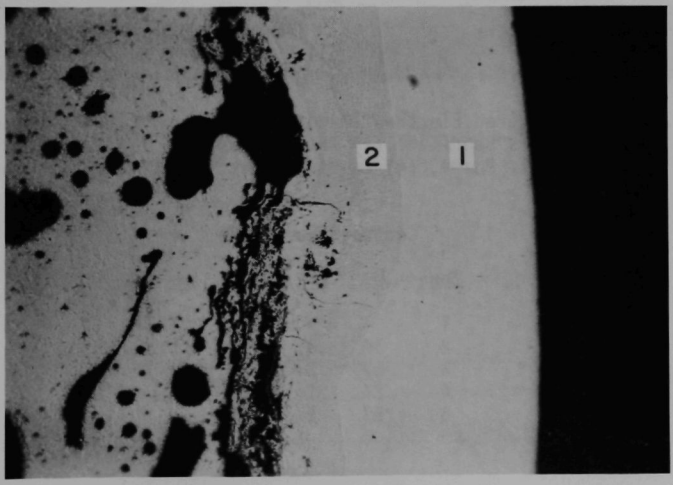

Fig. II.8. Liquid-phase Matrix Penetration in HT9 Cladding: (1) Intact Cladding, (2) Reacted Cladding. (As-polished, 150X, MCT 244014.)

at room temperature and fractures readily. Figure II.9 shows the SEM backscattered electron image of the reacted cladding and the compositions of the major phases in the reacted zone as determined by energy-dispersive X-ray analyses. The composition of the unreacted cladding, both immediately adjacent to the well-defined reaction boundary and further away, was essentially that of the original HT9 material. No diffusional-controlled subphases or intergranular penetration ahead of the visible reaction boundary could be detected on the cladding side of the boundary at magnifications up to ~3000X.

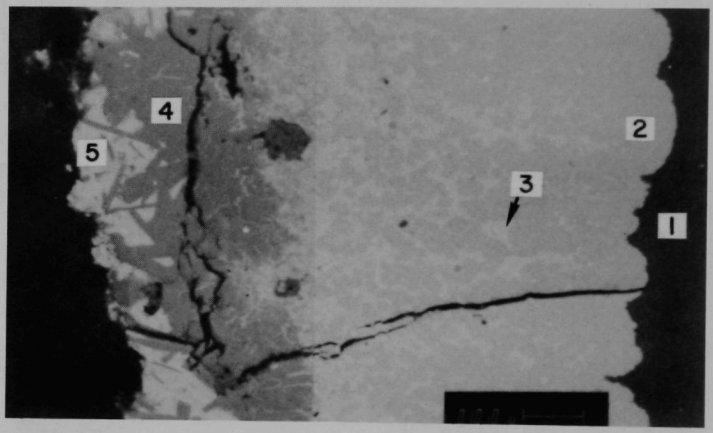

Fig. II.9. Backscattered Electron Image of the Cladding Reaction Zone in a U-10Zr/HT9 Specimen: (1) Intact Cladding, (2) Dendritic Phase, (3) Matrix Phase, (4) Zr-rich Phase, (5) Once-molten Fuel

Composition (at.%)

Zone	U	Zr	Fe	Ce
1	-	-	88	12
2	16	3	70	11
3	67	3	28	2
4	2	32	49	17
5	67	5	28	-

4. Time-dependent Cladding Penetration Rate

Several tests were performed on comparable specimens at the same temperature (800°C) but for different durations. The principal purpose of these tests was to determine whether the penetration rate would vary strongly with time, particularly during the latter part of a heating cycle. The results, summarized in Fig. II.10, show that after the initial rapid reaction, the penetration rate either remains constant or decreases with time. Apparently, no runaway penetration occurred at any time during the tests. The rapid penetration at the onset of the heating is probably related to a fuel/cladding diffusional interaction during the steady-state irradiation. The interdiffusion layers on the fuel and cladding surfaces, upon reaching 800°C, apparently liquefied with little delay. After these layers were consumed, further penetration into the cladding was then controlled by diffusion across the liquid/solid boundaries.

5. Temperature-dependent Cladding Penetration Rate

The duration of most of the FBTA tests was 1.0 h. The rates of liquid-phase cladding penetration determined from these 1.0-h tests are shown in Fig. II.11. (Penetration rate is defined as the measured maximum penetration divided by the 1.0-h test duration; it represents an effective rate and includes the accelerated penetration at the onset of heating.) Data scatter in the liquefaction band shown in the figure is due mainly to the wide variability of

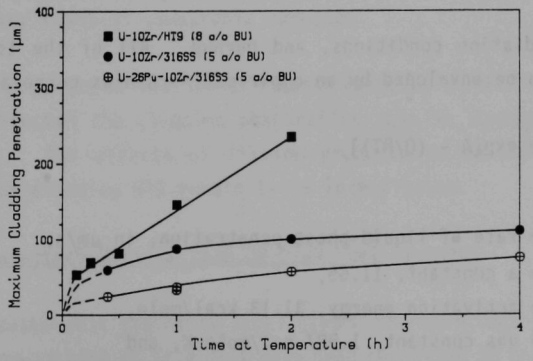

Fig. II.10. Time-dependent Cladding Penetration at 800°C

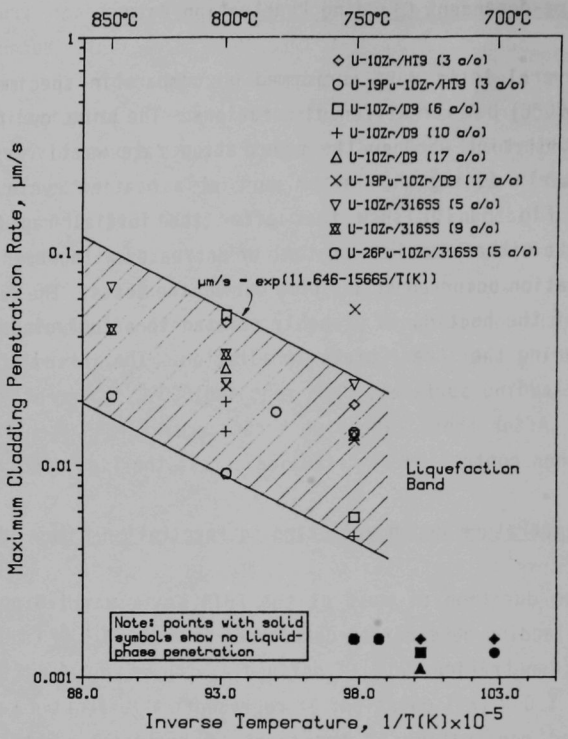

Fig. II.11. Effective Cladding Penetration Rates for Specimens Tested for 1.0 h

material, irradiation conditions, and burnup. All of the test data points, except one, can be enveloped by an empirical Arrhenius correlation

$$S = \exp[A - (Q/RT)],$$

where

S = rate of liquid-phase penetration, in μm/s,
A = a constant, 11.65,
Q = activation energy, 31.13 kcal/mole,
R = gas constant, 1.987 cal/mole K, and
T = temperature, K.

The exception occurred in test 90-01 on a specimen from the midplane section of a high-burnup (17 at.%) U-19Pu-10Zr/D9 element. Because of excessive swelling of the cladding (~7% diametral strain) near the midplane of this element, a gap developed between the fuel and cladding during steady-state irradiation. Additional fuel swelling into the gap apparently resulted in a more open fuel structure of the high-Pu-content fuel and created more paths for the migration of the lanthanide fission products to the fuel surface (see Fig. II.6). These concentrations of lanthanide fission products are apparently responsible for the enhanced cladding penetration. An identical test, 90-02, on a specimen obtained from the upper portion of the same element where swelling of the cladding was more modest (~1% strain), yielded a penetration rate only about one-fourth of that in the 90-01 test.

6. Conclusions

Three types of fuel/cladding interaction have been identified in the metallic fuel compatibility tests conducted in the FBTA. No interaction was noticeable at temperatures below 700-725°C. At higher temperatures, solid-state interdiffusion, liquid-phase grain boundary penetration, and liquid-phase matrix penetration were found.

The temperature-dependent liquid-phase penetration followed an Arrhenius correlation. An enveloping penetration-rate equation, developed from 1.0-h test data, may be used to evaluate fuel-element cladding wastage during an off-normal reactor event of comparable duration.

The presence of lanthanide fission products in the fuel/cladding gap significantly affected the cladding penetration rate in austenitic stainless-steel claddings. The effects of fission products on nonswelling, tempered martensitic steel cladding HT9 remain to be investigated.

C. Breach Characteristics of Lead D9 Clad Fuel Elements

Tests of austenitic stainless steel clad U-xPu-10Zr fuel (x = 0, 8, 10 wt %) to peak burnups as high as 18.4 at.% have been completed in the EBR-II reactor (see Refs. 7 and 8 for a detailed test description). Their steady-state behavior

has been summarized in Sect. II.A of this report. Cladding breach behavior at closure welds, in the gas plenum, and in the fuel column region have been observed. In all cases, the breach behavior has been benign.

1. Breach Histories

The X419 test was reconstituted at 1 and 3 at.% burnup for postirradiation examination before it was terminated at 11.9 at.% with no breaches observed. Two elements from X419 at this burnup level have been used for the RBCB program. Longitudinal defects in the fuel region were induced and subsequently led to failure. Their behavior after breach was consistent with the fuel column breach reported below in the X420 test. Details on the X482 (U-19Pu-10Zr) and X482A (U-10Zr) tests can be found in Ref. 9.

The X420 test was reconstituted at 5.5 at.% burnup prior to its first breach at 13.5 at.% burnup. Further reconstitution led to termination at 17.1 at.% burnup, prior to which 10 additional breaches occurred.

The X421 test was reconstituted at 10 at.% burnup and terminated at 18.4 at.% burnup. Two breaches occurred at >17 at.% burnup.

Of the 13 breaches in X420 and X421, all but four occurred in the fusion zone of the upper closure TIG weld, remote from the fueled core region.

Three of the breaches in the X420 tests, not associated with the closure weld, also occurred above the core region and were not fuel-specific. The failure site was in the plenum region about midway between the upper closure weld and top-of-fuel. The site was at an identical elevation in all three elements.

The only breach observed that may truly be fuel-specific occurred in element T084 from the X420 test at ~16.4 at.% burnup. A good estimate of the breach burnup can be made since tag gas signals and delayed-neutron (DN) signals were coincident. The failure site was a hairline crack in the fuel region of the U-19Pu-10Zr element, ~9 in. (~22.9 cm) from the bottom of the fuel column (X/L_o ~0.67).

2. Weld Failures

Table II.2 summarizes the nine upper weld failures experienced in the X420A, X420B, and X421A tests. The uncertainty in burnup at breach for the X420B elements stems from the fact that reactor Runs-149 and -150 were a particularly "busy" time for breaches in EBR-II and multiple fission gas and tag signals did not lend themselves to straightforward identification. Recent preliminary analyses appear promising in characterizing the fission gas signals of metallic fuel plenum leakers.[10]

In all cases, a characteristic sodium (and liquid fission product) deposit could be seen on the upper weld surface during postirradiation examination. A typical weld failure deposit appears in Fig. II.12. The initial weld failure in the X420A test was examined destructively in some detail. The failure site was located at a sharp notch between the end plug base metal and the fusion zone. The heat-affected zone in the cladding appeared uncracked. A small tight crack grew perpendicular to the element axis through the fusion zone of the weld and allowed fission and tag gas to escape. The intergranular crack was ~0.060 in. (~1.5 mm) long on the weld surface and had a maximum opening of ~0.0002 in. (~5 microns). Figure II.13 shows a section through the end plug at

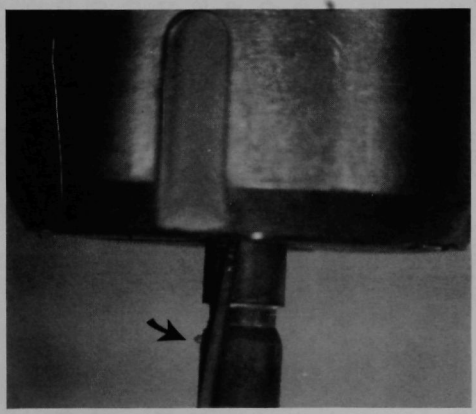

Fig. II.12. Sodium Deposit at the Upper Weld Breach of Element T060

TABLE II.2. Breach Data in the Lead D9 Subassemblies

Fuel Composition	Element ID No.	S/A ID No.	% Burnup (Final)	Type of Breach	Estimated % Burnup at Breach	% Fission Gas Left in Plenum	Observed Weight Loss, g
U-19Pu-10Zr	T084	X420B	17.03	Fuel Region	16.4	10.68	4.11
U-19Pu-10Zr	T109	X420B	16.90	Plenum	~14.5-17	5.86	1.80
U-19Pu-10Zr	T177	X420B	16.96	Plenum	~14.5-17	1.91	3.84
U-10Zr	T150	X420B	17.00	Plenum	~14.5-17	13.84	2.19
U-19Pu-10Zr	T060	X420A	14.66	Upper Weld	13.5	1.13	0.36
U-8Pu-10Zr	T025	X420B	16.80	Upper Weld	~14.5-17	N/A	0.25
U-8Pu-10Zr	T028	X420B	17.03	Upper Weld	~14.5-17	N/A	0.61
U-10Zr	T090	X420B	17.07	Upper Weld	~14.5-17	N/A	0.50
U-19Pu-10Zr	T118	X420B	17.08	Upper Weld	~14.5-17	N/A	0.66
U-8Pu-10Zr	T033	X420B	17.08	Upper Weld	~14.5-17	N/A	0.55
U-19Pu-10Zr	T047	X420B	17.10	Upper Weld	~14.5-17	N/A	1.20
U-10Zr	T233	X421A	17.45	Upper Weld	17.4	18.11	1.14
U-19Pu-10Zr	T072	X421A	17.83	Upper Weld	<17.8	47.89	1.03

N/A = Data not available.

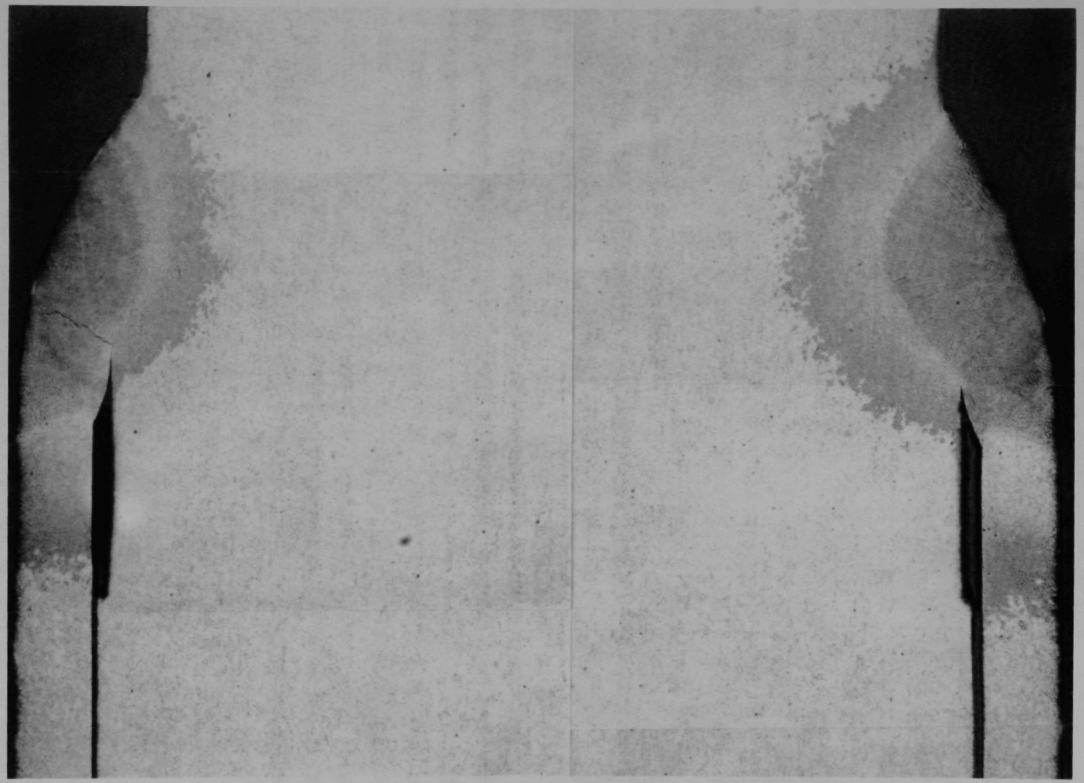

Fig. II.13. Transverse Section Through the Upper End Plug of Element T060. The weld fusion zone at the left contains the crack.

a depth where penetration was incomplete. A wafer was sliced from the failure site and examined on the energy dispersive spectrometer (EDS) in the scanning electron microscope (SEM). Only semi-quantitative results were possible due to the high radiation field. Spectra from the fracture surface and nearby bulk weld zone revealed the as-built D9 compositions. Sodium soluble fission products (strontium and barium) in minor levels were seen on surfaces which had been in contact with the bond sodium after breach. Radiological smear samples of the breach region in most of these types of failures read high in Eu 154-155, Sr 89-90, Ba-La 140, and Cs 137. A few of these breaches showed trace amounts of nonsoluble fission products (like Zr 95 and Rh 106) and microgram levels of fuel, no doubt swept through the breach as small particulate. The weld failures were all of a benign nature, with no fuel loss or DN signals present. Weight loss in these failures (after running in the RBCB mode for times up to five months) was generally small but readily detectable. Mass balances could be used to rationalize the weight loss by fission gas alone; the crack openings were apparently so small that some of the elements still contained appreciable gas inventories after breach.

The breach can be interpreted as a result of the high stress concentrator and high plenum pressure in these short plenum elements. No evidence for fission product assistance is seen. Redesign of this weld fitup has eliminated the stress-riser effect, and plenums have been lengthened in subsequent test elements. It is interesting to note that identical design closure welds were used in subsequent tests with HT9. The X425 test operates equivalent in pressure and temperature to X420 in reactor row-4. It has not experienced any breaches, weld or otherwise, to ~17.5 at.% burnup to date.

3. Plenum Breaches

Table II.2 lists three elements from the X420B test which experienced plenum failures at high burnup. They also failed during the same time interval as the weld failures and so contributed to the myriad of tag and fission gas signals present during reactor Runs-149 and -150. Because the plenum is a region of low cladding temperature and strain with no adjacent fuel, the occurrence of breach was an unexpected one. The three elements lost considerable weight after

failure which can only be rationalized by a substantial venting of tag and fission gas, sodium bond, and sodium soluble fission products. The failure site in all three elements is ~4.5 in. (~11.4 cm) from the upper end. Two of the elements were adjacent to one another in the bundle; the other was four rows of elements away. All were outer row elements adjacent to the duct wall.

Figure II.14 shows a laser profilometry scan of element T177. The overall profile is the average of four scans, 45° apart, while the inset shows a set of individual scans, 10° apart, in the breach region. The breach site in all three elements showed this region of slight ovality. Siblings from this test at similar burnup showed no such features in their plena though all elements became oval due to bundle-duct interaction in the highly strained fuel region (see Fig. II.3 for peak strains at this burnup).

While no cracks were discernible on the cladding exterior after washing (a bright stain was the only obvious feature), optical metallography revealed a substantial crack ~0.100 in. (~2.5 cm) long and ~0.0005 in.

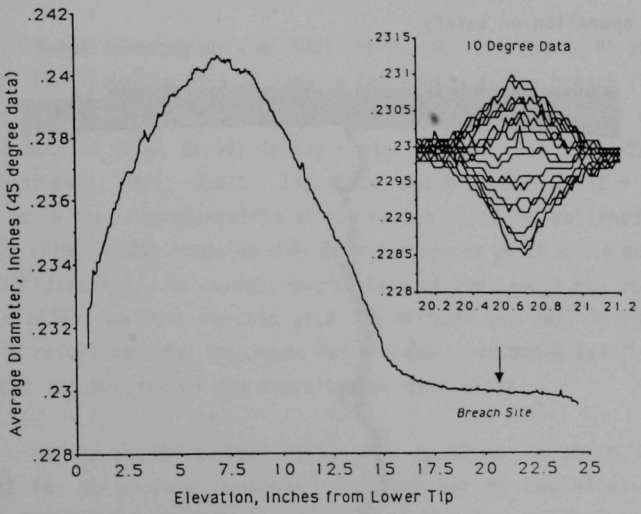

Fig. II.14. Diametral Profile of T177, a Plenum Breach Element. Inset shows ovality at the breach.

(~13 microns) at its widest in transverse section. Figure II.15 is an as-polished section through the breach in element T177. The crack runs along the element axis perpendicular to the major stress and appears to have initiated on the cladding inner surface. It is intergranular throughout with numerous branched secondary cracks. Etching revealed no anomalous microstructures in the D9 nor was any extraneous material in contact with the cladding inner surfaces. Micro-hardness data taken at 90° intervals did not vary with azimuthal angle (293 +/- 13 DPH at the breach, 304 +/- 27 DPH away from the breach). Thus no evidence for overheating or inhomogeneous as-built structure could be found.

The exact cause of these plenum breaches cannot be determined. The best guess is that handling forces (likely a bending moment) during one of the two remote reconstitutions may have caused a defect which eventually resulted in a stress rupture failure of the plenum. The fact that all three elements failed at the same exact site and were all outer row elements is likely more than coincidental. Outer row elements would be more prone to interact with the old duct during disassembly and with the fresh duct during reassembly.

In any case, plenum failures such as these are benign, with no effect on reactor operation or safety.

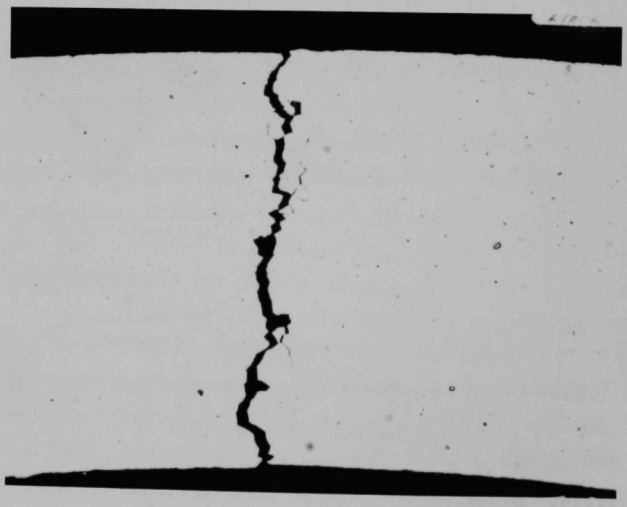

Fig. II.15. As-polished Micrograph of the Plenum Breach in Element T177

4. Fuel Column Breach

With the exception of the two predefected elements from X419 used in the RBCB tests[9] experience with natural fuel column failures in D9-clad metallic fuel is limited to T084, a U-19Pu-10Zr elements from X420 (see Table II.1).

A clear correlation between xenon tag and DN signal was used by the EBR-II Core Surveillance Section to identify this breach.[11] Using the ratio of Xe 131 to Xe 134, they were able to determine that a high Pu element was the DN signal source. They estimated the burnup at 16.3 at.% using the Xe 129 and Xe 130 mole fractions. Postirradiation examination of the X420 test proved both predictions true.

Figure II.16 (from Ref. 11) shows the coincident DN and fission gas signals from this breach. Expulsion of bond sodium and DN precursors (consistent with the loss of 4.11 g at time of examination) led to the DN signal as a burst of ~20 min. duration, approximately four times background. This type of signal is consistent with the results from Ref. 9 for small cracks in D9 cladding in the fuel column area.

Gamma scanning data of T084 for Cs, Nb, Zr, and Ru-Rh showed a loss of Cs (Fig. II.17) but no loss of fuel in the region of the breach (Fig. II.18). The latter observation was supported by optical metallography of an as-etched transverse section (Fig. II.19) in the breach region, ~9.1 in. (~22.9 cm) from the bottom of core, (x/L_o ~0.67). The crack, which appears at 12 o'clock in the photo, is not a true representation of the breach site. As-polished sections of this region (Fig. II.20) revealed only hairline cracks which would not be visible at this magnification. An in-cell degradation of the sample had occurred after etching in which the fuel reacted with the etchant and cell atmosphere. The unfortunate result was that the fuels swelled and in so doing split the cladding even further and propagated the crack to the size shown.

At the cladding outer surface the crack was ~0.20 in. (~5 mm) long by ~0.0002 in. (5 microns) wide and ran parallel to the element long axis (perpendicular to the cladding hoop stress). The main crack is intergranular with a few smaller cracks, 2 to 3 grain diameters long, clustered nearby.

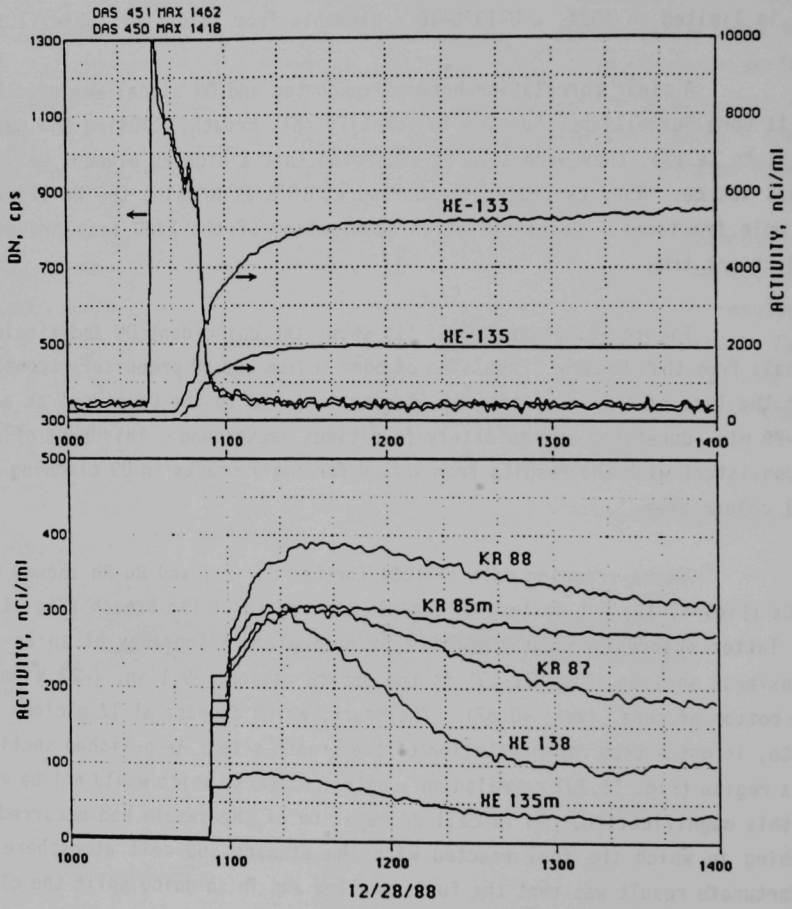

Fig. II.16. Delayed Neutron and Fission Gas Signals Associated with the Fuel Column Breach Element T084

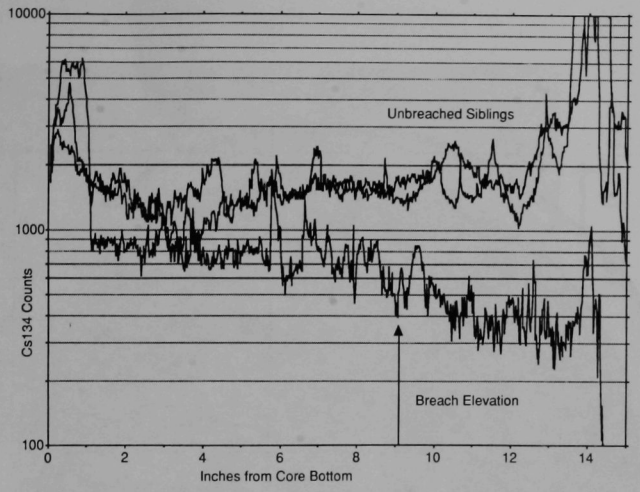

Fig. II.17. Comparison of Cs134 Inventories of the Fuel Column Breach and Unbreached Siblings

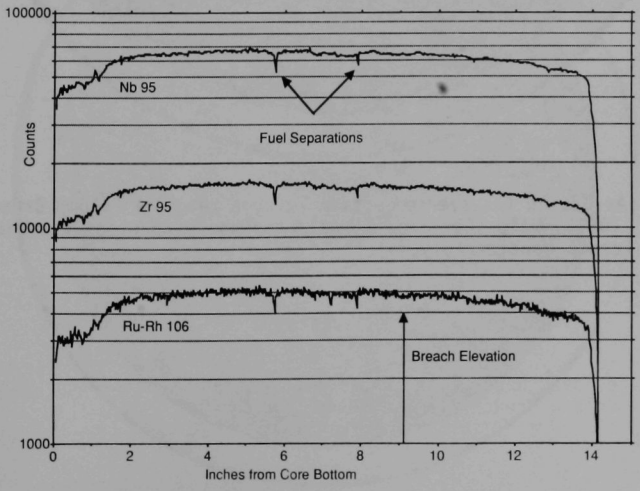

Fig. II.18. Gamma Scans of Fuel Column Breach Element T084 for the Solid Fission Products Nb95, Zr95, and Ru-Rh106

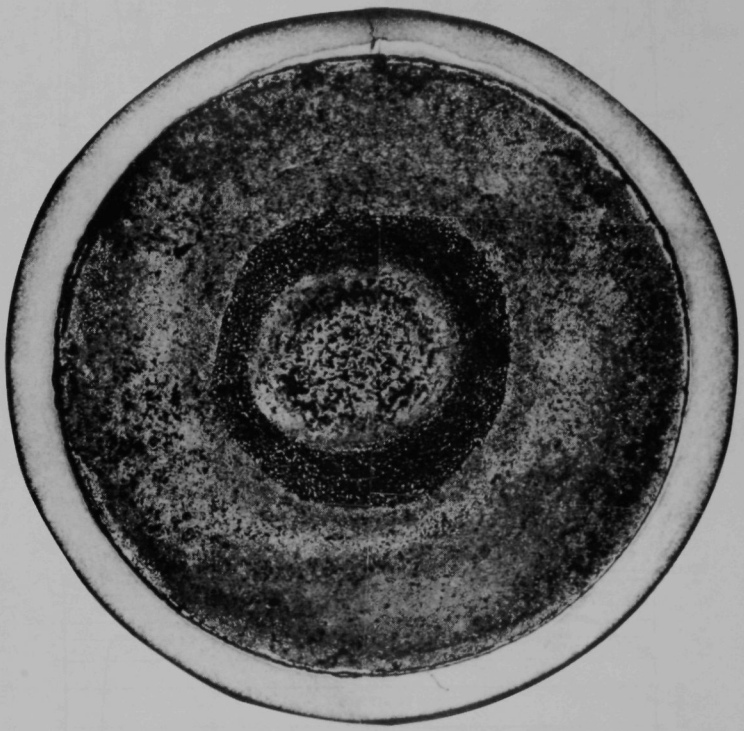

Fig. II.19. As-etched Transverse Section Through the Fuel Column Breach Site in T084. Note: An in-cell fuel/atmosphere reaction has widened the crack considerably.

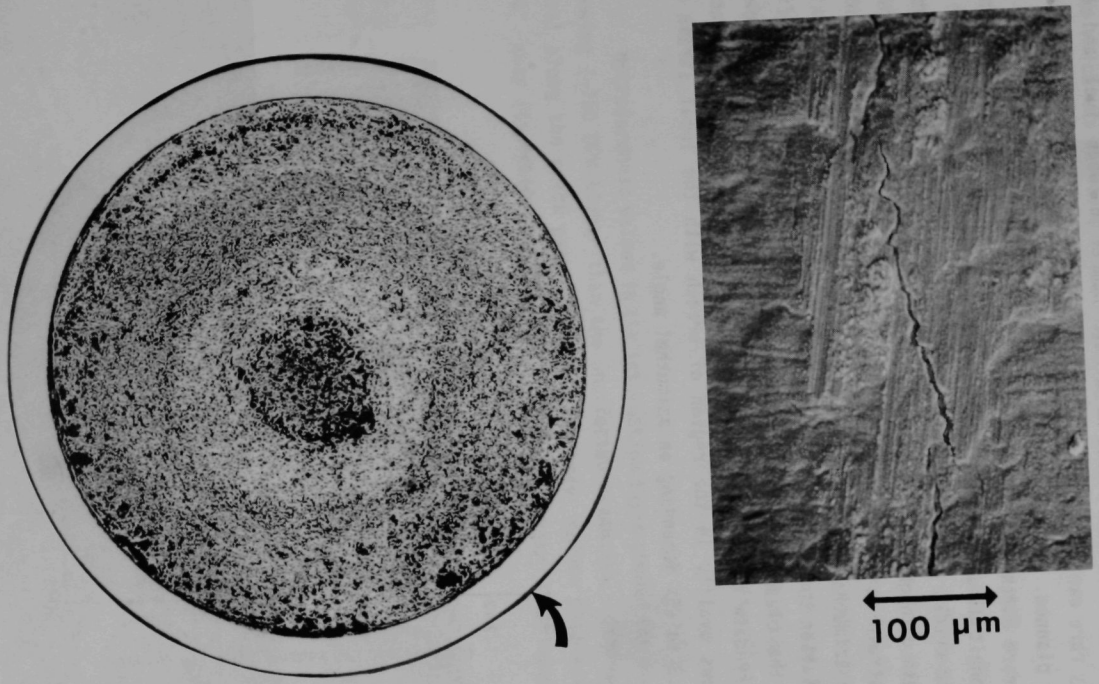

Fig. II.20. Micrographs of the Breach in T084, As-polished Section (Left) and Cladding Surface (Right)

Scanning electron microscopy showed that some of the secondary cracks were filled with a material intermediate in atomic number between fuel and cladding, presumably rare earth fission products. Further examinations of the breach site have been planned. Quantitative chemical analyses of the interaction zone and adjacent rare earth precipitates will be made with the electron microprobe. A shallow longitudinal "groove" (Fig. II.21) could be seen on top of and adjacent to the main crack, possibly caused by abrasion with an adjacent element in this tight bundle of highly strained test elements (2/3 of the elements in the bundle have ~4% strain at this location). The crack was opposite T084's own wrapper wire at an azimuthal position where element/element interaction is maximum and tends to flatten the normal cladding circular cross-section. Laser profilometry confirmed the cladding ovality at this elevation. Figure II.21 shows laser profilometry data on T084 analogous to Fig. II.14 for the plenum breach site. It too shows ovality in the region of breach with the local strain varying between ~3.3 to ~5% depending on azimuthal angle.

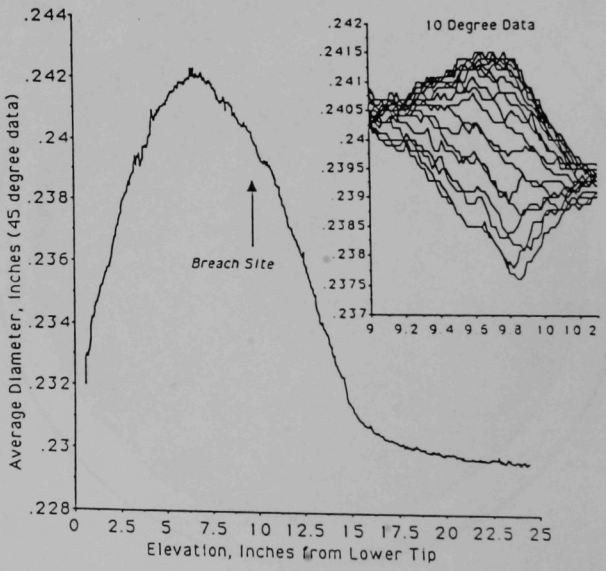

Fig. II.21. Diametral Profile of T084, the Fuel Column Breach Element. Inset shows ovality at the breach.

The crack occurred in an area of intense fuel/cladding solid state interaction which was revealed by an oxalic acid etch. This structure is shown clearly in Fig. II.22.

The maximum depth of interaction was ~0.15 mm (~0.006 in.) and was centered on an azimuthal arc (~30° wide) of increased interaction. This layer is typically very hard and often cracks during microhardness indentures. This type of interaction has been associated with the interchange of Ni and Fe from the cladding with the lanthanide series of fission products (La, Ce, Pr, Nd, Pm, and Sm). The fuel adjacent to the breach appeared to be unaffected by the breach. The annular zones of redistribution were concentric and resembled sibling fuel at like burnup. It is clear that fuel loss in this type of breach is not to be expected since crack openings are small and no sodium/fuel reaction products form.

Microhardness values in the interaction layer showed the usual degree of hardening (~750 DPH higher than the unaffected cladding). However, the D9 base metal along the crack path had lower hardness values than samples 90° and 180° away (typically 50 DPH less). It would appear that based on the

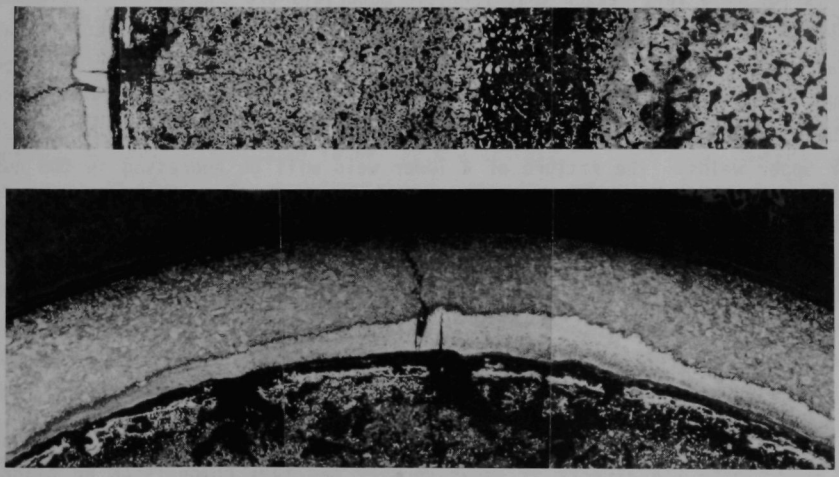

Fig. II.22. As-etched Transverse Micrographs at the Breach Elevation in T084

observations of accelerated fuel/cladding chemical interaction and the cladding softening, nominal cladding temperatures were exceeded for an indeterminate amount of time in-reactor. At this high burnup cladding dilation and thermal bow possibly promoted local regions of distorted geometry and coolant flow. Stress rupture of the cladding would thus be promoted in areas of high cladding wastage and lowered creep strength.

EBR-II operated with consequence of this fuel column breach to the scheduled end of the run for an additional 34 days (~0.6 at.% burnup). Fuel column failures of this type in D9-clad metallic fuel are of limited impact on reactor operations. Because gas release in the fuel region is relatively gradual, and the fuel is compatible with the coolant, no breach propagation nor fuel loss is to be expected. The benign behavior of metallic fuel column breaches is one of the many favorable attributes of metallic fuel.

In one sense, none of the observed breaches are truly prototypic of "end-of-life" metallic fuel failures in the next generation of LMR's. The fuel column breach of T084 is non-prototypic of cladding failures in that the use of high swelling cladding materials (i.e., D9 and 316 SS) for wire-wrapped elements beyond a reasonable level (i.e., burnup) of bundle tightness will be avoided. It is for this very reason that ferritic materials are the preferred cladding choice. There are also some indications that ferritics suffer less solid-state fuel/cladding chemical interaction than the austenitics. Weld designs have been improved in the experimental program and can be made reliably. Weld failures are a non-fuel issue at any rate but are benign events when they do occur at least for upper welds. The failure of a lower weld will be addressed in the next series of RBCB tests now in planning. HT9 welds have proven reliable thus far in all of the HT9 subassemblies irradiated to date. Cladding defects induced during remote reconstitution are always possible but will be an unlikely situation since the subassembly will only be assembled once in its lifetime.

D. HT9-Clad Blanket Fuel Performance at 1.2 at.% Burnup

The objectives of the X431 and X432 HT9 clad blanket tests are 1) investigate the effects of smear density and fuel composition on blanket element behavior to prototypic goal burnup, 2) generate performance data which

will be used to benchmark the LIFE-METAL fuel performance code, especially regarding fuel/cladding mechanical interaction in high smear density applications, and 3) provide irradiated test elements for ex-reactor high temperature tests.

The reference driver fuel for an advanced Liquid Metal Reactor system such as the Integral Fast Reactor would be a U-Pu-Zr alloy clad in a low-swelling steel. The fuel would typically contain >20% plutonium and 10% zirconium by weight. A 75% smear density and low-swelling tempered-martensite steel such as HT9 are chosen to limit cladding deformation at high fluences. The design choices for metallic blanket fuel are not yet as clearly defined because little pertinent data on metallic blanket fuel exists. High fertile-to-fissile conversion rate and performance reliability are required. As was the case for driver fuel, a low-swelling cladding alloy is needed since residence times on the order of four to five years are currently anticipated. The HT9 steel appears to satisfy this requirement. The choice of fuel composition and smear density is not as clear, however. Paper studies to date have only considered HT9-clad U-10Zr fuel of 85% smear density as the reference type. The impetus for the X431 and X432 tests was to expand fuel designers' options to consider still higher smear densities and/or more dilute alloys of U-Zr.

The X431 and X432 tests were initiated to demonstrate the possible tradeoffs between smear density (85% vs 90%) and fuel alloy content (U-2, 6, and 10% Zr). In order to maximize conversion of U-238 to Pu-239, the heavy-metal density of the fuel is an important parameter. For the three alloys tested the uranium density is estimated to be: 17.9 g/cc (U-2Zr), 15.9 g/cc (U-6Zr), and 14.2 g/cc (U-10Zr). The disadvantage of using the reference driver fuel alloy (U-10Zr) is thus clear. However, the reduction of zirconium content lowers the solidus temperature of the fuel, the significance of which depends on the postulated off-normal events for the reactor in question. The estimated solidus temperatures would be: 1160°C (U-2Zr), 1201°C (U-6Zr) and 1233°C (U-10Zr). Geometric smear density of the blanket element is a key parameter in determining the extent to which fuel/cladding mechanical interaction (FCMI) can be accommodated with low strains or cumulative damage fraction. From prior EBR-II tests of HT9 clad U-19Pu-10Zr fuel, we know that insignificant FCMI occurs at or below 75% smear density. Additional strain (but no breach) occurred in 85%

smear-dense driver fuel to ~12.5% at.% burnup (X441). The effect of zirconium on fuel/cladding chemical interaction in binary fuel has not yet been determined, and thus is another aspect that fuel designers must consider during off-normal events.

1. Test Description

Each 19 element subassembly contained two to five elements from each of the six groups described in Table II.3. All six types were wire-wrapped HT9-clad elements ~38.5 in. long x 0.370 in. in diameter. The fuel slugs in all six types were nominally 13.5 in. x 0.313 in. Smear density was thus controlled by cladding wall thickness. The as-built plenum-to-fuel volume ratio was 1.82 (85% smear density) or 1.93 (90% smear density). U-235 enrichment was adjusted to give each fuel type the same power, given by: 8.5% (U-2Zr), 10.7% (U-6Zr), and 13.2% (U-10Zr). Both subassemblies were operated at a peak midplane linear power of ~12 kW/ft. The peak inside cladding temperature was ~600°C for both subassemblies. Burnup rates varied between the three alloys due to the enrichment in U-235 and are given by: ~0.0043%/day (U-2Zr), ~0.0049%/day (U-6Zr), and ~0.0056%/day (U-10Zr).

TABLE II.3. Nominal Fuel Design Parameters

Type	Fuel Alloy	Smear Density	Cladding Wall Thickness, mils
A	U-2Zr	85%	15
B	U-2Zr	90%	20
C	U-6Zr	85%	15
D	U-6Zr	90%	20
E	U-10Zr	85%	15
F	U-10Zr	90%	20

2. Examination Results

The data summarized here was obtained on interim examinations of the X431 and X432 tests at ~30% of their goal burnup of 5%. Axial fuel growth, cladding diametral strain and optical metallography will be presented.

a. Axial Fuel Growth

Neutron radiography was used to measure axial fuel growth in the 38 elements from X431 and X432. The average response is summarized below in Table II.4. It appeared that the fuel/cladding radial gap was closed except near the very top of the fuel column.

Though this data base is small, several observations can be made regarding axial growth of these blanket elements. For both smear densities tested, the U-6Zr fuel tends to show the least axial growth of the three alloys tested. For a given level of burnup and Zr addition, the as-built fuel/clad gap

TABLE II.4. Axial Fuel Growth

Subassembly	Fuel Alloy	Smear Density	% Peak Burnup	% Axial Growth
X431	U-2Zr	85%	1.07	5.09
X431	U-2Zr	90%	1.06	2.77
X431	U-6Zr	85%	1.22	4.04
X431	U-6Zr	90%	1.22	2.29
X431	U-10Zr	85%	1.38	4.95
X431	U-10Zr	90%	1.36	2.73
X432	U-2Zr	85%	1.35	5.77
X432	U-2Zr	90%	1.38	3.26
X432	U-6Zr	85%	1.56	3.91
X432	U-6Zr	90%	1.57	2.38
X432	U-10Zr	85%	1.78	4.82
X432	U-10Zr	90%	1.70	2.75

governs the amount of axial growth. High smear densities promote low axial growth levels. Free swelling in the axial direction is effectively shut off once the gap is closed. Assuming that the gap is fully (but only recently) closed, the ratio of radial to axial (free-swelling) growth is approximately 2:1. This anisotropy was noted in previous tests of fuel in EBR-II examined at low burnup prior to fuel/clad contact.

3. Cladding Strain

The cladding diameter profiles were measured by spiral contact profilometry after irradiation. This technique measures the diameter at 90° to the spacer wire. The average response is summarized below in Table II.5.

Though the data base is small and the strains minor, the general trends in cladding deformation behavior can be summarized as follows:

TABLE II.5. Cladding Strain

Subassembly	Fuel Alloy	Smear Density	% Peak Burnup	% Cladding Strain
X431	U-2Zr	85%	1.07	0.25*
X431	U-2Zr	90%	1.06	0.36
X431	U-6Zr	85%	1.22	0.26
X431	U-6Zr	90%	1.22	0.32
X431	U-10Zr	85%	1.38	0.20
X431	U-10Zr	90%	1.36	0.30
X432	U-2Zr	85%	1.35	0.30*
X432	U-2Zr	90%	1.38	0.32
X432	U-6Zr	85%	1.56	0.21
X432	U-6Zr	90%	1.57	0.32
X432	U-10Zr	85%	1.78	0.22
X432	U-10Zr	90%	1.70	0.26

*In the region of uniform deformation per discussion below.

- For all fuel alloys, the 90% smeared-density elements showed more strain in spite of their thicker walls. This is to be expected if FCMI dominates fission gas loading.

- Zirconium content did not appear to significantly affect the cladding deformation at these burnups.

- All 21 of the thin-walled 85% smeared-density elements showed sinusoidal diametral strain traces, indicative of some wire/jacket interaction. Therefore, the peak strains reported above may be an over-estimate of the true strain since ovality is usually greatest 90° to the wire.

- Position on the subassembly grid regarding inner/outer row location had no discernible effect on the cladding strains.

- Essentially no measurable strain occurred in the plenum region from gas loading alone. The diameters in the plenum region were generally within as-built dimensions.

- Four of the five U-2Zr 85% smeared-density elements showed pronounced ovality and large cladding strains at the bottom ~2.5 in. of the fuel column. Peak diametral strains ranging from 1.9% to 3.3% were observed. The diameters 90° to the peak strains showed corresponding negative strains (i.e., less than as-built diameters).

In order to understand this observed anomaly, the neutron radiographs were closely inspected. Fuel structures in these regions were observed to differ from the rest of the slug. A mottled appearance showing density variations was noted at the exact locations of the anomalous cladding strain. Gamma scans of the U-2Zr fuel for fission product activity were made. No unusual fission product distributions were observed in any of the fuel examined. The only notable effect was that of greater Cs 134 and Cs 137 retention in the 90% smear-dense fuel. Essentially no Cs activity could be observed in the displaced bond sodium above the fuel column. This is consistent with the lesser

amount of interconnected porosity in the 90% smear-density fuel. Pre-irradiation radiographs showed no prior anomalies in the fuel, cladding, or bond sodium levels. Hand-held micrometer measurements of 22 spare X431/X432 siblings showed no local cladding strain in this region in the as-built condition. A review of the manufacturing data showed no nonconformances in these elements regarding sodium-bond quality, as-built densities, etc.

One of the elements from the X431 test was destructively examined by optical metallography. The region of ovality at the bottom of the fuel column was sampled with longitudinal and transverse sections (see Figs. II.23 and II.24). The fuel consisted of basically three types of microstructure. The "normal" fuel consisted of the usual finely divided two-phase structure (alpha + delta), with a homogeneous distribution of small fission gas bubbles and zirconium globules. At the point of maximum ovality, this structure covered approximately 20% of the cross-section. Fuel/cladding contact in this region was

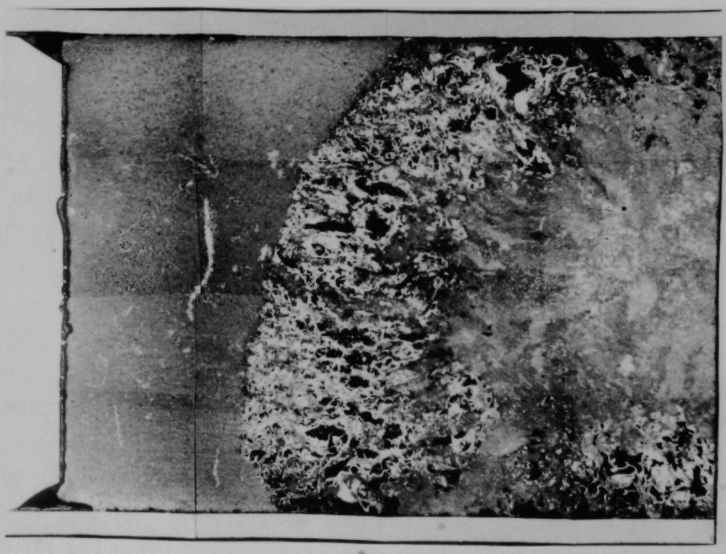

15X

Fig. II.23. Longitudinal Section Through the Region of Ovality in an Irradiated U-2Zr Blanket Element

20X

Fig. II.24. Transverse Section Through the Region of Ovality in an Irradiated U-2Zr Blanket Element

tight. The second type of structure observed, which covered approximately 30% of the cross-section, was a very porous and "torn" structure reminiscent of the morphology of low-temperature ternary fuel after ~2% burnup. This structure has been interpreted in the past as grain boundary cavitational swelling. Fuel cladding contact was intermittent in this region. The remaining 50% of the fuel was generally found in-board of the "torn" structure and appeared the least porous. Air-etching the samples overnight in the containment box revealed extremely coarse grains of a columnar nature. Sections taken at the very top of the slug (see Fig. II.25) and just below midplane also contained regions of this type though no "torn" fuel or cladding ovality was observed. The latter sample contained coarse grains covering ~50% of the cross-section. The grain diameters

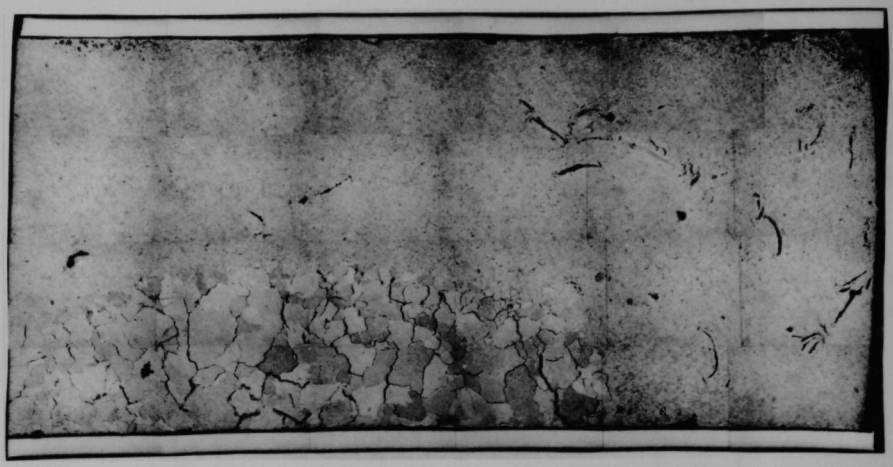

15X

Fig. II.25. Longitudinal Section Through the Upper Portion of a U-2Zr Blanket Element

in these regions ranged up to ~0.030 in. (~750 microns). Fuel microhardness data showed the coarse grains to be ~20% harder than nominal in the region of ovality and ~50% harder than nominal at the top of the slug. Cladding hardness data taken at the five elevations sampled showed no effect of the type of adjacent fuel, nor was any significant fuel/cladding chemical interaction observed, despite the fairly high cladding temperature (600°C) at the top of the fuel column.

An unirradiated sibling element (U-2Zr, 85% smear density) was also examined to determine if the coarse-grained structure observed after irradiation had any as-cast precursors due to the injection-casting process or sodium bond heat treatment (~500°C for 1 h).

The structure revealed by etching this fuel consisted of a homogeneous distribution of fine-grained acicular phase typical of quenched uranium alloys of low-to-moderate zirconium content. This phase is likely the metastable alpha-prime phase, supersaturated in zirconium. No evidence of precursors to the coarse or columnar grain structure as seen in the irradiated fuel was observed.

Microhardness data showed a constant level at all elevations averaging ~360 DPH. According to the literature this level of hardness is reasonable for a martensitic alpha-prime type of structure in quenched uranium alloys. The "normal" irradiated fuel averaged ~170 DPH at the bottom and ~180 DPH at the top of the column. The coarsened irradiated fuel averaged ~200 DPH at the bottom and ~270 DPH at the top of the column. Softening of the structure is not inconsistent with in-reactor tempering. Pores and voids in the fuel would also tend to soften the fuel.

Exaggerated grain growth similar to the unirradiated U-2Zr fuel has been observed in ex-reactor heat treatments of uranium. It was reported that the preferred growth direction for coarsening and irradiation growth is the same, i.e., [010]. Grain refinement is believed to be controlled by inclusion content, and so it can be speculated that an inhomogeneous distribution of impurity content may have catalyzed the localized grain coarsening that was observed. The temperature distribution in-reactor could also promote grain growth, since single crystals of uranium can be prepared by annealing suitably heat-treated polycrystalline uranium in a temperature gradient.

It is now speculated, based on the evidence, that fuel cladding mechanical stresses resulted from coarsening along a preferred growth direction. These growth stresses were sufficiently high at the cooler end of the column to deform the cladding. Since the ovality appeared maximum at 90° to the wire, some constraint by the bundle must have occurred. The fact that the 90% smear dense U-2Zr siblings showed no such ovality may be due to their thicker wall and hence lower stress. The examinations of unirradiated sibling elements suggest that the cladding ovality did not occur during element manufacture.

All of the type "A" fuel has been removed from the X431 and X432 test matrix to prevent interference with the goal of achieving prototypic burnups.

4. Conclusions

Good performance characteristics have been observed in the high smear density U-Zr blanket fuel tested to ~30% of goal burnup. With one

exception, their behavior has been consistent regarding expected cladding and fuel strain. No breaches have been incurred at this burnup level. Anomalous cladding strain behavior has been observed in U-2Zr, 85% smear-density fuel. The X431 and X432 tests will continue irradiation to goal burnup of 5% or first natural breach.

References for Section II

1. G. L. Hofman et al., "Swelling Behavior of U-Pu-Zr Fuel," Metal. Trans. A, **21A**:517 (1990).

2. R. G. Pahl et al., "Experimental Studies of U-Pu-Zr Fast Reactor Fuel Pins in the Experimental Breeder Reactor-II," Metal. Trans. A, **21A**:1863 (1990).

3. S. T. Zegler and C. M. Walter, "Compatibility Between U-Pu-based Fuels and Potential Cladding Materials," AIME Nuclear Metallurgy Symp. on Plutonium Fuels Technology, AIME 13 (October 1967).

4. G. L. Hofman et al., "Chemical Interaction of Metallic Fuel With Austenitic and Ferritic Stainless Steel Cladding," Proc. Intl. Conf. on Reliable Fuels For Liquid Metal Reactors, **121**, Section 4:131, Tucson, AZ (1986).

5. A. E. Dubberley et al., "Designing for Passive Safety in the ALMR," Proc. Intl. Fast Reactor Safety Mtg., **I**:131, Snowbird, UT (August 12-16, 1990).

6. H. Tsai, "A Versatile Apparatus For Studying The Behavior of Irradiated Fuel," Trans. Am. Nucl. Soc., **60**:655, San Francisco, CA (November 26-30, 1989).

7. R. G. Pahl et al., "Steady-state Irradiation Testing of U-Pu-Zr Fuel to >18 at.% Burnup," Proc. Intl. Fast Reactor Safety Mtg.," **IV**:129, Snowbird, UT (August 12-16, 1990).

8. R. G. Pahl, C. E. Lahm, R. Villarreal, W. N. Beck, and G. L. Hofman, "Recent Irradiation Tests of Uranium-Plutonium-Zirconium Metal Fuel Elements," Proc. Intl. Conf. on Reliable Fuels for Liquid Metal Reactors, 3, Tucson, AZ (September 7-11, 1986).

9. G. L. Batte' et al., "Run-beyond-cladding Breach (RBCB) Test Results for the Integral Fast Reactor Metallic Fuels Program," Proc. Intl. Fast Reactor Safety Mtg., **IV**:207, Snowbird, UT (August 12-16, 1990).

10. J. D. B. Lambert, Argonne National Laboratory, personal communication (1991).

11. J. R. Armstrong, Argonne National Laboratory, personal communication (1989).

III. PYROMETALLURGICAL PROCESS DEVELOPMENT

A key element in the Integral Fast Reactor (IFR) Program is the development of an efficient process for recovering plutonium and uranium from the metallic core and blanket materials, removing fission products from them, and re-enriching the core alloy with plutonium bred in the blanket. To accomplish this, major efforts are directed toward flowsheet development and process chemistry, process development studies, engineering-scale demonstration of the electrorefining process, and waste treatment and management.

A. Process Flowsheet and Chemistry

The IFR pyrochemical process flowsheet has been refined so that it has the necessary flexibility for providing the desired products (essentially pure uranium and a U-Pu mixture) from all IFR spent-fuel compositions while generating a minimum volume of waste, which has very low transuranic (TRU) element content. The major focus of flowsheet refinement is examining the operational and safety issues associated with the FCF demonstration.

In the IFR process, spent fuel in its stainless steel cladding is chopped into approximately quarter-inch lengths and placed in a basket that is introduced into molten salt at 500°C in an electrorefining vessel. The basket is connected to a dc power supply and made anodic; nearly pure uranium is removed from the spent fuel by electrotransport to solid cathodes, then the plutonium and any remaining uranium in the feedstock are electrotransported to liquid cadmium cathodes. The actinides are almost completely removed from the cladding hulls, and noble metal fission products either remain in the basket or fall as particulate to the bottom of the electrorefiner. The alkali and alkaline earth metals in the spent fuel are oxidized and remain in the electrorefiner salt, as do most of the rare-earth fission products.

As reported previously,[1] a computer code, PYRO, has been developed that accurately predicts the distribution of the elements in the electrorefiner during the individual operations that make up the pyrochemical process. The newest modifications of the PYRO code, along with various waste and feedstock compositions, were used to study fuel and waste processing strategies. The results indicated that fuel processing can be easily adapted to the various sorts of

feedstocks that are expected, provided only that the results obtained in earlier experiments hold up in the actual equipment with spent fuel as feed.

After some number of batches of fuel have been processed (perhaps a dozen, depending on the age of the fuel and its activity, it will be necessary to remove lanthanide fission products from the salt so that the heating of the electrorefiner by fission-product decay will decrease. This will be done by contacting the electrorefiner salt with an almost-saturated solution of uranium in cadmium. Plutonium, the minor actinides (primarily Np, Am, and Cm), and a fraction of the lanthanides will be reduced into the cadmium; the salt will contain the lanthanides and some additional uranium. The plutonium and minor actinides will be returned to the electrorefiner. The salt will be treated with lithium ("stripped") to remove the uranium and lanthanides, then returned to the electrorefiner.

Where cadmium is used in the electrorefining process (cadmium cathodes, as well as salt extraction and stripping), the critical issue for product and waste composition is the distribution of rare earths and actinides between cadmium and the molten salt. Sufficient basic data and practical experience have been acquired to assure that the product compositions will be satisfactory and that adequate separations can be achieved in the lanthanide removal process. However, supporting chemistry studies are being undertaken to increase the precision with which one can calculate the distribution of the lanthanides and actinides between salt and cadmium and to test or eliminate the simplifications and assumptions used in earlier quantitative flowsheet calculations.

As part of the supporting chemistry studies, the separation factors for pairs of the rare earth elements up to atomic number 64 (gadolinium) and for neodymium vs. plutonium are being measured. These separation factors are being determined by measuring the distribution of these elements between salt (LiCl-KCl eutectic) and metal (cadmium) phases at 500°C. Activities and activity coefficients are also being measured by electrochemical means for the most common rare earth elements. No major process changes have resulted from replacing previous assumptions and approximations with experimental data (agreement with existing estimates was usually quite good). Detailed predictions of product compositions with respect to the behavior of the individual rare earth elements are expected to improve as more experimental data become available.

There were some unexpected findings, however. Yttrium was much more readily oxidized than expected; a provisional value for the separation factor between yttrium and lanthanum is approximately 30. Europium was so easily oxidized that it was closer in behavior to alkaline earths than rare earths. Also, it was expected to see a mixture of $EuCl_3$ and $EuCl_2$, at least under highly oxidizing conditions; only $EuCl_2$ was found, even in the presence of excess $CdCl_2$.

It was also found that interactions occurred among the rare-earth/cadmium intermetallic compounds. Usually, rare earth concentrations in saturated cadmium solution were half or less of the saturation level in binary rare- earth/cadmium systems. It is believed that solid solutions among the intermetallic compounds are forming, and current calculations are based on that assumption. Until a widely applicable description of the precipitating solid composition is available, separation factors based on unsaturated cadmium solutions should not be used where rare-earth-containing solids exist; order-of-magnitude errors are possible.

In support of safety analyses, the affinity of the IFR electrolyte for water is being investigated under hypothetical accident conditions. For these studies, a set of water-salt mixtures having various compositions are equilibrated in conditions of constant temperature and humidity until they reach an unchanging composition. Mixtures having excess water evolve water, while salt-rich samples absorb water until all samples reach this constant composition. The boundary between water-absorbing and water-evolving mixtures of salt and water is then determined as a function of temperature and humidity. This information is being used to evaluate accident scenarios for risk of criticality.

Figure III.1 shows the unchanging composition derived as a function of sample temperature and humidity (humidifier temperature). This figure shows the overall water composition that would be reached (from the salt-rich side) after a long time at various electrorefiner temperatures and absolute atmospheric humidities following a hypothetical accident. The conditions are conservative in that they correspond to low electrorefiner temperatures, unusually high humidities, and long times at those high humidities when compared to the expected electrorefiner conditions and the climate of the FCF site. Nonetheless, they show that accident-induced criticalities due to water absorption are unlikely. This work has been completed except for measurements at a few more conditions of temperature and humidity.

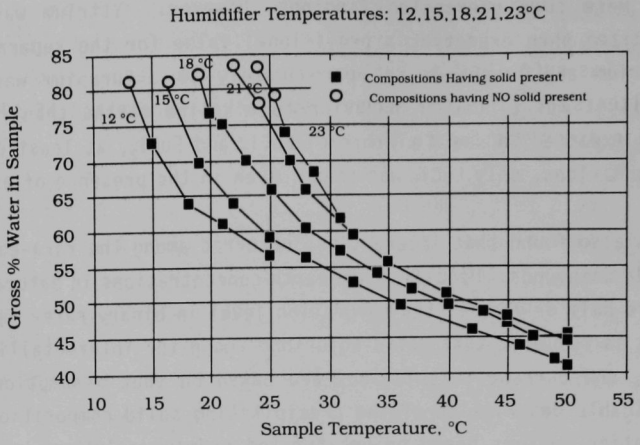

Fig. III.1. Unchanging Salt-Water Compositions as Function of Sample Temperature and Humidifier Temperature (indicated at top of each curve)

B. Process Development Studies

The process development studies include experiments to determine the effect of impurities in the argon atmosphere on the plutonium behavior in the IFR electrorefiner, post-test examination of a laboratory-scale electrorefiner crucible to determine any life-limiting mechanisms, and experiments to study zirconium behavior in the electrorefiner.

1. Salt/Atmospheric Reactions

The IFR pyroprocess operations are normally carried out in a high-purity argon atmosphere (<10 ppm oxygen, <10 ppm water). It is of interest to know the plutonium behavior in the electrorefiner in the event that the argon gas purity were to be compromised in a hypothetical accident. Two tests were completed in which salt, approximating that used in processing IFR fuel, was placed in an MgO crucible and exposed to varying levels of H_2O and O_2 at 500°C. The tests were conducted in a small tube furnace, utilizing once-through air (21°C dew point) that was exhausted through high-efficiency particulate air filters. The plutonium-containing salt for these experiments was obtained from the laboratory-scale electrorefiner.

In the first test, a diaphragm pump was used to introduce glovebox air into the furnace. The air exited the furnace through an outlet tube. The air flow rate was sufficient to replace the air volume every minute in the space over the molten salt. In the second test, a gas consisting of 100 ppm O_2 and 100 ppm H_2O in argon was fed to the furnace.

In both tests, the UCl_3 was rapidly oxidized from the salt. Since the crucible material was MgO, a thermodynamic potential for the reaction $(\text{uranium chloride})_{salt} + (MgO)_{solid} = (\text{magnesium chloride})_{salt} + (UO_2)_{solid}$ exists in this system. Therefore, a third test was run to determine if this reaction, rather than reaction with air in the cover gas, was responsible for the rapid loss of UCl_3 from the salt solution. In this test, the salt was added to two steel crucibles, one of which contained MgO crucible fragments.

Figure III.2 shows the plutonium analytical data for tests I and II, and Fig. III.3 the uranium data for test I (a similar plot was obtained with the uranium data for test II and is not included here). Figure III.4 shows the uranium data for test III in the presence and absence of MgO. The data for rare

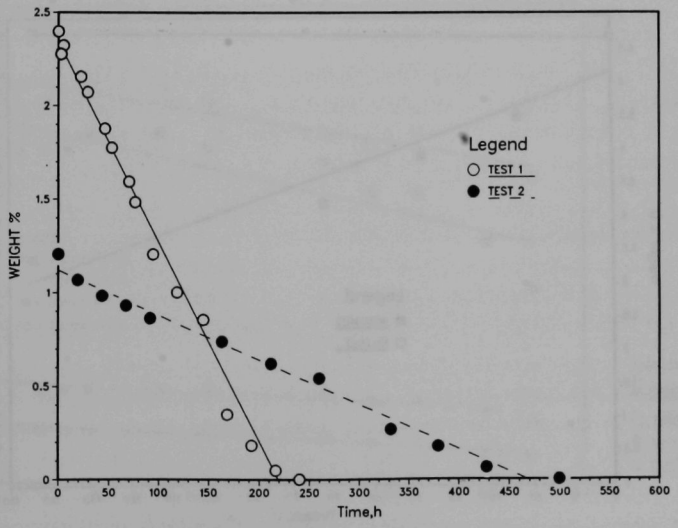

Fig. III.2. Plutonium Analytical Results for Tests I and II

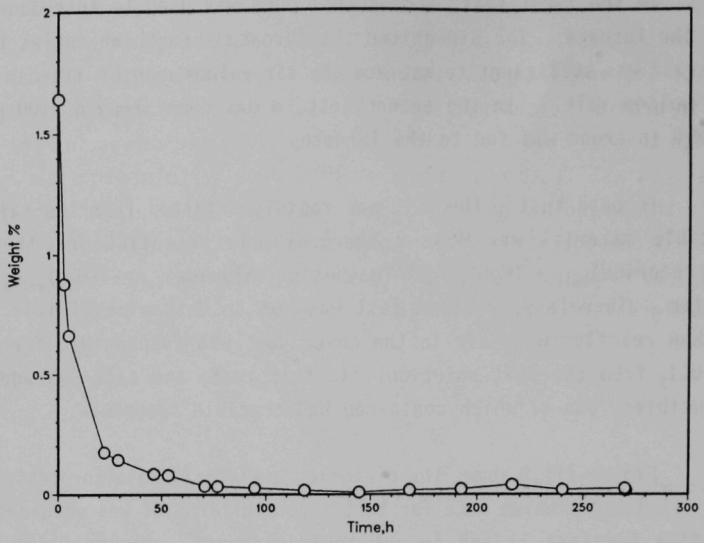

Fig. III.3. Uranium Analytical Results for Test I

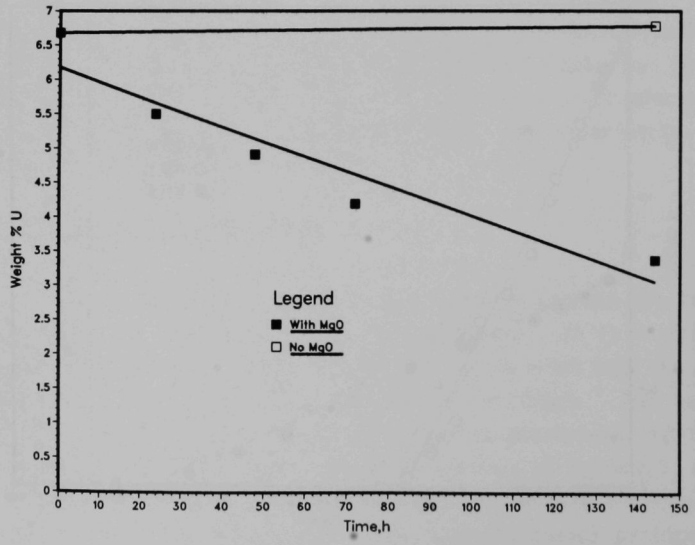

Fig. III.4. Uranium Analytical Data for Oxidation of UCl_3 with and without MgO in Test III

earth concentration in test II are given in Fig. III.5. The data in these figures show that the uranium concentration decreased much more rapidly than the Pu, Ce, Nd, Sm, and Y concentrations. As indicated by Fig. III.4, the rapid decrease in uranium concentration in the first two tests was due to interaction of UCl_3 with the MgO crucible. Since the slopes for the curves in Fig. III.2 are much less for test II than I, the oxidation rate for plutonium was reduced by decreasing the O_2 and H_2O content of the cover gas. The rate of decrease in Nd, Ce, Sm, and Y concentrations also depended on the O_2 and H_2O levels in the argon cover gas. As expected, the rate of plutonium oxidation was lower than that of uranium and greater than that of the rare earths.

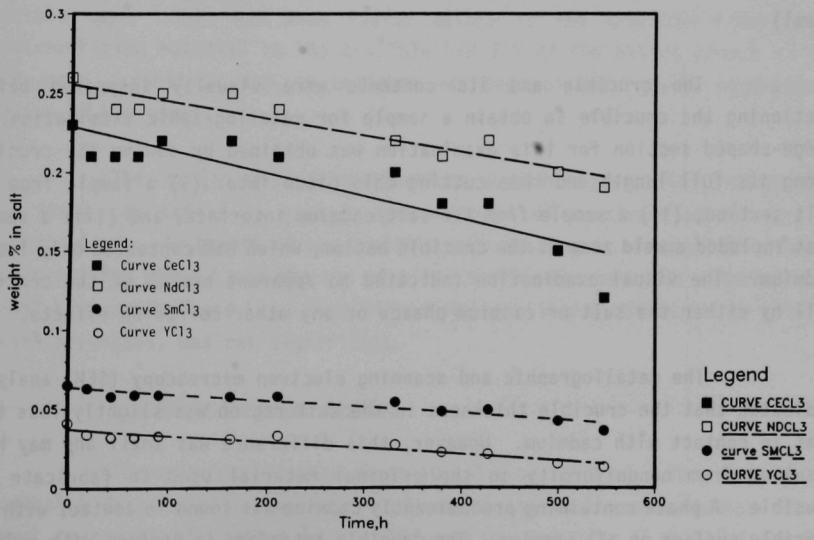

Fig. III.5. Rare Earth (Ce, Nd, Sm, and Y) Concentration vs. Time for Test II

The layer of material at the bottom of the MgO crucible from test I was analyzed by X-ray diffraction and was found to contain mostly salt, with two additional cubic phases. The first phase was UO_2, with a smaller amount of UO_2-PuO_2 solid solution or rare earth oxides. The second phase was PuO_2. This X-ray analysis indicated that the ratio of UO_2 to PuO_2 was 2:1. Thus, there was no preferential buildup of PuO_2.

2. Examination of Laboratory-Scale Electrorefiner Crucible

The laboratory-scale electrorefining cell was shut down for maintenance after approximately four years of operation at ~500°C. This shutdown was caused by a water leak (in a copper cooling coil), which resulted in an air leak in the side arm of the furnace tube. Because the above tests revealed that $PuCl_3$ and UCl_3 in the salt are converted to oxides in the presence of oxygen, it was decided not to reuse the 15-cm dia crucible for the electrorefiner cell and its contents. Further, it was decided that destructive examination of the crucible would provide a good opportunity to obtain valuable information on the corrosion behavior of the crucible material (low-carbon steel) and on possible side reactions involving the electrorefiner contents (salt, Cd, U, Pu, Zr, and steel).

The crucible and its contents were visually inspected before sectioning the crucible to obtain a sample for metallographic examination. A wedge-shaped section for this examination was obtained by sawing the crucible along its full length and then cutting this piece into: (i) a sample from the salt section, (ii) a sample from the salt/cadmium interface, and (iii) a sample that included a weld zone at the crucible bottom, which had contacted only liquid cadmium. The visual examination indicated no apparent breach of the crucible wall by either the salt or cadmium phases or any other corrosion effects.

The metallographic and scanning electron microscopy (SEM) analysis indicated that the crucible thickness in the salt region was slightly less than that in contact with cadmium. However, this difference was small and may have resulted from nonuniformity in the original material used to fabricate the crucible. A phase containing predominantly cadmium was found in contact with the crucible surface on all samples. The crucible interface in contact with cadmium metal, which had features common to all samples, is characterized by a thin layer

(1-3 μm) of U-Fe adhering to the crucible surface. The ratio of U to Fe in the layer was close to the 67 mol % U-33 mol % Fe eutectic composition in the binary U-Fe system. Since the eutectic temperature is 723°C, the thin layer was likely formed by reaction of uranium dissolved in cadmium with the steel crucible. The thinness of the layer suggests that it is passivating, and thus helps protect the steel from further attack.

The crucible corrosion appeared to occur evenly and at a low rate. This observation suggests that the crucible wall was subjected to slow, planar corrosion. No evidence for selective grain boundary attack on the steel was found and very little salt was present in the samples, including that taken from the salt region. Thus, the steel crucible is stable in the chloride salt. A light grey solid phase was observed on the surfaces of the samples taken from the salt region and the salt/cadmium interface region. This phase essentially consisted of Cd and Zr, and elemental analysis of this phase indicated a composition of Cd_2Zr. This phase also contained small amounts of U and Pu (<5 wt %) and even lower amounts of Fe (<1 wt %).

Examination also revealed a weld joint separation (0.013-cm wide) where the crucible upper shell had been fusion welded to the crucible floor plate. Electrorefining material in the crucible had filled the entire length of this weld joint separation, but no evidence was seen of substantial corrosion or erosion of the steel.

The results of these examinations provide experimental evidence that mild steel can safely be used as the material of construction for the IFR electrorefiner. No breach of the crucible wall was found, nor any life-limiting mechanism that would limit the use of mild steel as the crucible material. The amount of U and Pu found in an immobilized state, either by diffusion or precipitation processes, was not significant.

3. Zirconium Behavior Studies

Zirconium constitutes about 30 vol % of IFR fuel. This fuel will be anodically dissolved in the electrorefiner during fuel reprocessing. In the normal transport of uranium to a solid cathode and U-Pu to a liquid cadmium cathode, the bulk of the zirconium is not transported but is left in the

electrorefiner. With repeated cycles, this zirconium accumulates. In the normal course of electrorefining, a small, fairly constant amount of uranium and plutonium metal heel is left in the electrorefiner. In the presence of this U/Pu heel, the zirconium remains in the metallic state and is not oxidized into the salt phase.

Zirconium behavior in the engineering-scale electrorefiner is reported in Sect. III.C.4. One observation is that the zirconium solids do not disperse easily into the liquid phase. Instead, these solids seem to accumulate on solid surfaces in the electrorefiner. To more conveniently study the behavior of zirconium, a series of small-cell tests with a zirconium rod anode and cadmium pool anode are being conducted. In 1990, a cell of the type Zr/LiCl-KCl-$ZrCl_x$/Cd(Zr) was operated at 500°C. No uranium was used and ~21 g zirconium was transferred from the zirconium rod anode to the cadmium pool cathode. Visual examination at the end of the test indicated that the zirconium had deposited on top of the cadmium pool. X-ray diffraction analysis of a deposit sample indicated that Cd_2Zr had formed. Metallographic and SEM examination of the cell are now in progress to determine the location and form of the zirconium. It is planned to conduct additional tests to explore methods for removal of zirconium from the electrorefiner.

C. Engineering-Scale Process Development

The key steps in the pyrochemical processing of spent fuel are dissolution and product recovery by using either solid or liquid cathodes or direct chemical reduction. Progress made in developing each step is discussed below. Also reported are results from tests of zirconium behavior and a device for harvesting the uranium deposit from a steel cathode. All tests were conducted in the engineering-scale electrorefiner (0.9 m dia crucible).

1. Dissolution of Simulated Fuel

In earlier tests,[2] anodic dissolution of chopped, clad U-Zr alloy pins was demonstrated at the plant scale (~10 kg batch size). All of the alloy was removed from the cladding with a coulombic efficiency of about 50%; the anodic dissolution rate was 0.5 kg uranium per hour. After the anodic dissolution baskets were rotated at 250 rpm in the gas space above the salt in

the electrorefiner to reduce the amount of salt on the hulls, only 2 g uranium, not associated with the residual salt, remained on the cladding hulls.

In this report period, anodic dissolution of U-Zr-fissium alloy pins was demonstrated at the plant scale. With a coulombic efficiency of about 50%, nearly all (~99.8%) of the uranium was removed from the cladding. Some of the cladding segments were empty, but some contained a residue. Chemical analysis of the residue in several segments showed that about 65 wt % salt and 20% of the initial zirconium remained in the pins. The zirconium was associated with Ru, Mo, and Rh. If anodic dissolution of irradiated fuel shows that a large portion of the cladding hulls is filled with a salt residue, a technique may be needed to remove this salt.

2. Electrotransport to Solid Cathode

Improved performance has been achieved in the electrotransport of uranium from a cadmium pool anode to a single mandrel cathode. Previous tests[2] with multipin solid cathodes showed that the highest performance was attained with salt and cadmium mixing early in the run and no mixing during the later portion of the run. Under these conditions, 9.5 kg (0.26 kg/h) and 9.3 kg (0.35 kg/h) of uranium were deposited on a single mandrel cathode in 37 h and 26.5 h, respectively. A uranium deposit collected on a single mandrel cathode is shown in Fig. III-6. In the previous tests with single mandrel cathodes, salt mixing was continued during the entire run. Under this condition, the highest weight of uranium collected on the single mandrel cathode was 6.4 kg.

3. Electrotransport to Liquid Cadmium Cathode

Tests were conducted with the objective of electrodepositing 3 kg uranium in a liquid cadmium cathode (LCC) in 24 to 48 h. Voltage-current measurements on several runs showed that the cell resistance decreased as the elevation of the LCC crucible above the cadmium anode was decreased. The apparent resistance was 49 mΩ at a crucible elevation of 13 cm (5-1/8 in.) and 22 mΩ at 10 cm (4 in.). Most of the resistance was due to the small cathode area of the crucible. Based on the weight of the product from one run, about 3 kg uranium was collected in 32.5 h with a collection efficiency of 49%. Figure III.7 shows an autoradiograph of the sectioned product ingot. The dark areas

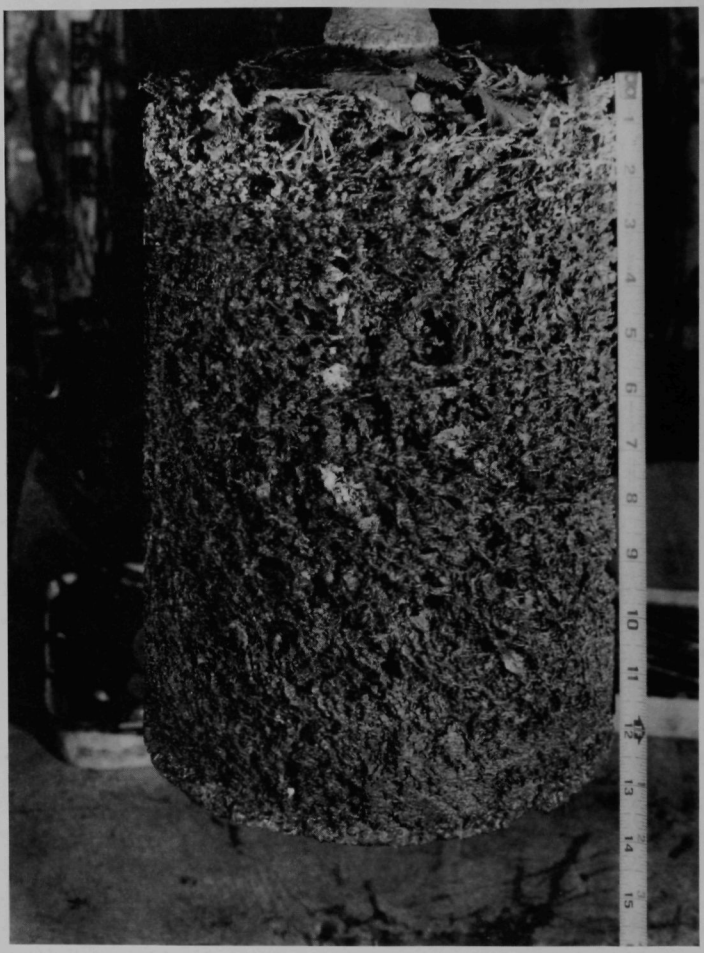

Fig. III.6. Photograph of Uranium Deposit (9.3 kg) on Single Mandrel Cathode (ANL Neg. No. 9132)

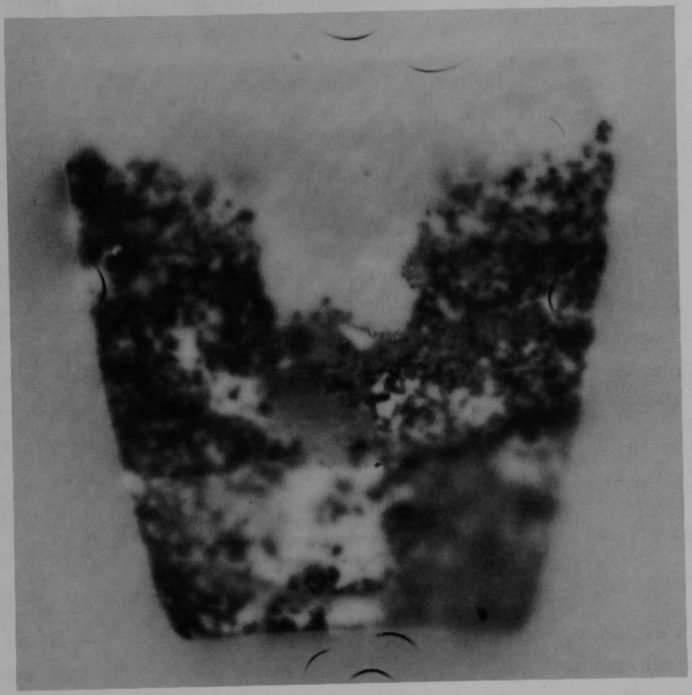

Fig. III.7. Autoradiograph of Sectioned Product Ingot from Test with Liquid Cadmium Cathode

(film exposed by β-radiation) show the location of uranium in the crucible. The radiograph indicates that the uranium distribution is good, i.e., under the cadmium surface and fairly uniformly distributed.

4. Zirconium Behavior

The zirconium behavior in the engineering-scale electrorefiner is being studied in conjunction with the other electrorefiner development work. In this study, unfiltered core samples (dip-tube sample through both liquids) and filtered samples of cadmium and electrolyte phases are being taken from the electrorefiner under various process conditions.

After numerous runs with the engineering-scale electrorefiner over the past 2-1/2 years, the total zirconium charged to the electrorefiner is 11.0 kg. The amount of zirconium removed as part of the cathodes is 3.43 kg. Thus, 7.57 kg Zr has accumulated in the electrorefiner. This quantity of zirconium is not reflected in analyses of the core or filtered samples taken of the electrolyte and the cadmium anode, which indicate a zirconium content of only 0.50 to 0.67 kg. Hence, approximately 7.0 kg Zr is unaccounted for and is believed to be residing somewhere in the electrorefiner. The amount of unaccounted zirconium has increased as the runs have progressed.

The zirconium content of the cadmium anode, based on the core samples, is within a relatively narrow range of 0.43-0.78 kg. The values for the filtered anode samples are in a range of 0.35-0.67 kg for the same runs. The solubility limit of zirconium in cadmium is 0.22 wt %,[3] which corresponds to an overall zirconium content in the anode of about 0.55 kg if the material is completely mixed. The reasonable agreement between the averaged zirconium content in the core and filtered anode samples, as well as the fact that the values are close to the solubility limit of zirconium in cadmium, suggests that the cadmium anode is saturated and not full of suspended zirconium solids.

All of the core samples have shown a higher zirconium concentration at the bottom of the electrorefiner. The samples at the bottom exceed the saturation value, whereas the samples taken higher up in the cadmium are less than the saturation value. Core samples were also obtained at positions about 90° around the electrorefiner circumference. Some core samples were taken while

mixing was being done, and others after mixing was stopped. The results indicated reasonable agreement in the zirconium values from each circumferential position and little effect of mixing.

It was suggested that zirconium loss from the electrorefiner may have occurred due to the formation of volatile $ZrCl_4$ (sublimation point 334°C). Samples were taken of material that had deposited on the upper positions of the heat shields (above crucible) and also material condensed and deposited on one of the small ports on the electrorefiner cover during a period when the port was only partially covered. Since cadmium has a fairly high vapor pressure, most of the condensed material was expected to be cadmium. Analyses indeed indicated cadmium contents of 95% or greater, and the zirconium contents were only 0.02 wt % for the heat shield deposit and <0.001 wt % for the cover deposit.

Thus far, no evidence has been found of zirconium accumulation at the salt-cadmium interface, which might be expected if Zr-Cd intermetallics had formed. Another possibility is accumulation of zirconium on the vessel wall. The engineering-scale electrorefiner has a perforated metal crucible that fits inside the main vessel, leaving a 1/8-in. (0.3-cm) gap between the crucible and the main vessel wall and bottom. Since zirconium might have deposited in this annular space, the inside wall was scraped and sampled for zirconium material. A ladle was used to scrape up one side wall, from the cadmium at the bottom through the salt layer. The analysis results for the main ladle sample are shown in Table III.1. Also shown in Table III.1 are analytical results for WS-1, a

TABLE III.1. Content of Sample from Wall Scraping

	Content, Wt %	
	WS-1	Ladle
U	3.16	3.88
Zr	0.35	0.59
Cd	74.9	91.4
Li	1.61	0.16
K	6.10	0.60

portion of the scraping that fell out of the top of the main ladle sample. The scraping presumably was collected higher on the electrorefiner wall, as reflected by its higher Li and K content. Interestingly, the zirconium content of this scraping is significantly higher than that of the average core sample, which is close to the saturation value of 0.22 wt %. This suggests that some zirconium-rich material may be adhering to the walls.

These studies will be continued to determine the options available for removing zirconium from the electrorefiner and further processing this material either as a waste to be discarded or as a material to be returned to the fuel cycle.

5. Equipment Testing

A device to harvest the uranium deposit collected on a steel mandrel cathode has been fabricated and tested in the engineering-scale electrorefiner. The main elements of this device are a machined die mounted on backing plates, which are attached to a unistrut framework. This device is secured by bolting it to two sections of unistrut channel, which are welded to the floor of the electrorefiner glovebox. A bolted collar is attached to the cathode assembly and the die positioned around a clean portion of the cathode mandrel above the deposit. A glovebox crane is then attached to the cathode assembly. To harvest the uranium deposit, the mandrel is pulled slowly through the die by lifting the cathode assembly with the crane.

The device was tested with the 12 kg (9.3 kg uranium) deposit on the single steel mandrel cathode shown in Fig. III.6. The purpose of the test was to determine the effectiveness of the device in removing the uranium deposit from the steel mandrel.

The uranium deposit was completely removed from the solid cathode mandrel, except for a thin layer of uranium. After uranium harvesting, this thin layer (less than 0.16 cm) can be removed by electrotransport of the uranium to the cadmium pool, and the mandrel can be reused in uranium electrodeposition runs. Information obtained during this test will be used to design the electrorefiner harvester equipment that will be used in the FCF. Further tests

are planned in which devices, other than the glovebox crane, will be used to pull the mandrel out of the uranium deposit.

D. Waste Treatment Processes

Processes are being developed to recover TRU elements from the metal and salt wastes in the electrorefiner and to convert the treated materials into disposable high-level waste forms. The metal wastes consist of cladding hulls, zirconium, and cadmium, which contains the noble metal fission products. Except for the cladding hulls, these wastes are expected to contain only small amounts of actinides. The salt contains the alkali metal, alkaline earth, rare earth, and halide fission products. It will also contain from 0.5 to 1.0% of the actinides fed to the electrorefiner. Efforts have been concentrated on developing processes for treating and immobilizing the waste salt.

1. Waste Treatment Flowsheet

The flowsheet for treating the salt and metal wastes discharged from the electrorefiner has been updated and new steps proposed which may have advantages for the overall fuel cycle. Among the more important changes is the removal of the bond sodium and alkali metal fission products from the chopped fuel by distillation. These metals are converted to chlorides in the salt stripper as described in Sect. III.D.3. Separating the alkali metals from the fuel (1) minimizes the sodium content of the salt in the electrorefiner and thereby avoids raising its melting point; (2) reduces the use of $CdCl_2$ to oxidize electropositive elements in the fuel and thereby decreases the amount of cadmium in the waste; and (3) removes cesium from the electrorefiner and thereby reduces the heat load by about 30%.

To remove waste salt and metal from the electrorefiner after several electrorefining cycles, the following operations are used:

1. After the last cathode product has been removed, the traces of actinides and a fraction (~10%) of the zirconium in the cadmium pool are transferred to the salt by adding $CdCl_2$ to the salt.

2. Most of the zirconium remaining in the pool is electrotransported to solid cathodes. A small fraction of the collected zirconium becomes waste, and the rest is used in the recycled fuel alloy.

3. A pump-filter assembly is inserted in the electrorefiner to circulate first salt and then metal through a sintered metal filter to remove particles of insoluble impurities, such as UO_2, and undissolved noble metal fission products (Nb, Mo, Tc, Ru, and Rh). Some cadmium is retained in the filter to remove the cadmium-soluble fission products (Pd, Ag, In, Sn, Sb, and Te). The filters are sent to waste processing.

4. An amount of lithium sufficient to reduce most (~90%) of the actinide chlorides is added to the electrorefiner. This leaves about 75% of the rare earths in the salt phase. Then, all of the salt is removed from the electrorefiner and sent to the treatment steps described below.

The process steps used to treat the salt and metal discharged from the electrorefiner are shown in Fig. III.8. To recover the TRU elements in the

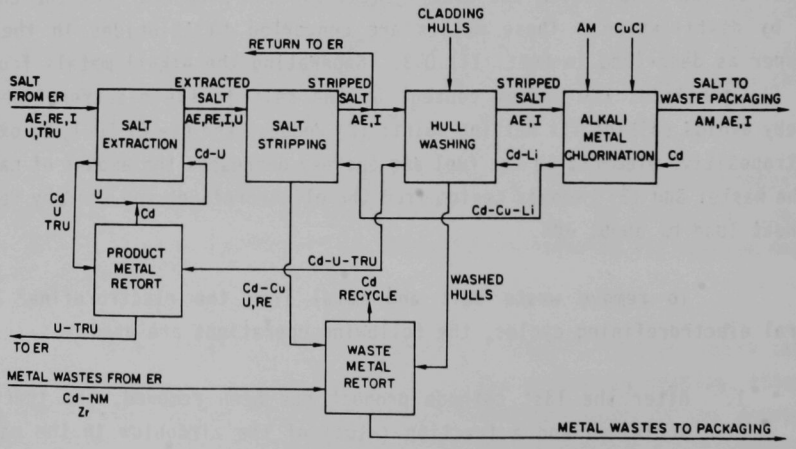

Fig. III.8. Waste Treatment Flowsheet
(ER = electrorefiner, RE = rare earths, NM = noble metals, TRU = transuranic elements)

salt and separate them from rare earths, the salt is first contacted with a Cd-U solution at 500°C in a multistage, countercurrent extraction train. The uranium in the metal phase exchanges to a greater extent with TRU elements in the salt phase than with rare earths. Figure III.9 illustrates the recovery of TRU elements and their separation from rare earths in extraction trains with four to seven equilibrium stages and metal/salt mass flow ratios from three to seven. These curves suggest that four to six actual stages in a counter-current extraction train will suffice to obtain the desired separation of actinides from lanthanides and reduce the actinide content of the salt to the 10^{-3} to 10^{-4} range.

After TRU elements are separated from rare earths in the extraction train, the entire batch of electrorefiner salt is fed to the stripper vessel where three steps are performed: stripping, cladding hull washing, and alkali metal chlorination (see Fig. III.8).

The treated salt is then absorbed into a zeolite, which strongly adsorbs the fission products Cs and Sr by ion exchange and contains the remaining salts in its "molecular cage." The initial investigations of this promising method for immobilizing waste salts are described in Sect. III.D.4.

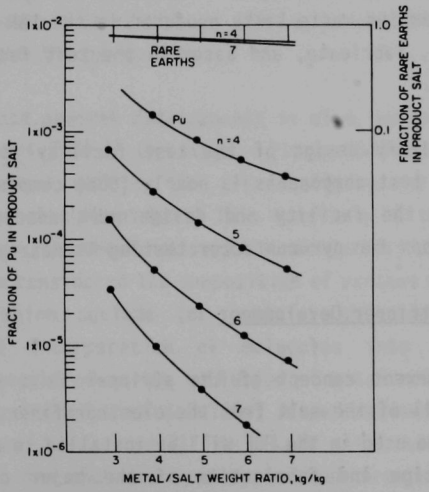

Fig. III.9. Extraction of Plutonium and Rare Earths from Salt by Multistage Contactors (n = number of stages)

The filters from the electrorefiner are combined with zirconium, cladding hulls, and the stripping alloy, which contains the rare earth fission products and uranium. This mixture is fed to the waste metal retort, where it is mixed with copper, then most of the cadmium is distilled off and recycled. A small fraction is left with the metallic residue, the remainder is equivalent to the fission product cadmium and the $CdCl_2$ added to the electrorefiner to oxidize rare earth, alkali metal, and alkaline earth fission products in the fuel. It is expected that the cadmium, uranium, and most of the fission products will be dissolved in the copper. The metal waste mixture will be densified by pressing or melting, then encapsulated in a thick, corrosion-resistant container for disposal.

2. Pyrocontactor Development

High-temperature centrifugal contactors (pyrocontactors) are being developed for separating TRU elements from rare earths in the IFR fuel cycle. A facility is being assembled for conducting experiments to determine the performance and extraction efficiency of the pyrocontactor with molten cadmium and chloride salts at 500°C. The ultimate goal is to develop a liquid metal-salt extraction process that uses multistage, countercurrent pyrocontactors to recover the TRU elements from the waste salts produced in the EBR-II FCF. The current effort is to design, fabricate, and assemble the test facility with a single-stage pyrocontactor.

Preliminary design of the test facility is complete and final design of the major test components is nearly (80%) completed. A glovebox was installed to house the facility and design work needed for modifying and extending the glovebox for pyrocontactor testing is nearly (85%) complete.

3. Salt Stripper Development

The current concept of the stripper is a stirred vessel large enough to contain all of the salt from the electrorefiner. A prototype of the stripper vessel to be used in the FCF will be installed in a 0.46-m (18-in.) dia furnace well. Design and fabrication of the major components is nearly completed. A pump-transfer line assembly will be used to transport about 60 L of salt containing rare earths and uranium from the electrorefiner into the

stripper, which will contain about 20 L of cadmium. The stripper will be equipped with an agitator capable of imparting mixing power densities up to 1.4 kW/m^3 (7 hp/1000 gal) in the salt and 5.9 kW/m^3 (30 hp/1000 gal) in the metal phase. Ports for sampling and charging materials, as well as fittings for instrumentation such as liquid level probes and reference electrodes, will be provided. Experiments will be conducted to determine stripping rates as functions of mixing intensity, effectiveness of filters, characteristics of insolubles, and performance of equipment and instruments.

4. Salt Waste Form Development

Although the treated salt will contain only trace amounts of actinides and very small amounts of rare earth fission products, it will contain Cs and Sr and is therefore likely to be a high level waste (HLW) according to the definition in the Code of Federal Regulations (Title 10, Part 60). As such, it must be disposed of in a geologic repository for HLW. Therefore, a waste form that will meet the acceptance criteria for the repository must be developed for the treated IFR waste salt. Definition of the exact acceptance criteria is still evolving, but in general terms, the waste form must be a solid monolith that is strong, leach resistant, and radiation resistant. It is also desirable that the salt immobilization process be relatively simple, amenable to remote operation, and compatible with the IFR pyroprocess.

With these general requirements in mind, we are developing a salt waste form that is fabricated in two steps: (1) immobilizing the waste salt in an inert, leach-resistant matrix, and (2) densifying the matrix to yield a mechanically strong, solid monolith. This matrix will then be sealed in a durable metal container. As the first step toward identifying a potential matrix for chloride salts, we considered the composition of various minerals. Naturally occurring minerals which occlude (or contain) chloride salts are known. ("Occlusion" is the incorporation of molecules into a zeolite cavity. "Hydration" can be thought of as the occlusion of water molecules.) Examples of chloride occluding minerals are sodalite, scapolite, and cancrinite. These minerals are zeolites, i.e., crystalline alkali metal and/or alkaline earth aluminosilicates that are characterized by an open framework with relatively large cavities and channels. The salt molecules are typically held in these cavities and are not readily released.

Efforts to identify zeolites that would occlude IFR waste salt and a process that would yield analogs of these naturally occurring minerals appear to have been successful. Promising results were obtained by contacting dehydrated A50, a synthetic zeolite having sodium as an exchangeable cation, with a molten salt (92.5 wt % LiCl-KCl eutectic salt, 5.0 wt % NaCl, 1.0 wt % CsCl, 1.0 wt % $BaCl_2$, and 0.5 wt % $SrCl_2$). The experiment consisted of pouring the molten salt at 450°C into a column of A50 supported on a quartz frit and allowing the salt to percolate through the column. The salt that flowed through the column and frit was collected and analyzed. The zeolite was washed with water to remove adhering salt, dried to constant weight, and analyzed.

Two types of reactions, ion exchange and salt occlusion, occurred between the molten salt and the zeolite. Most of the sodium ions on the zeolite were exchanged for ions in the salt, and the zeolite occluded about 40% of its weight in salt. Evidence for these statements is provided by the results given in Table III.2. The moles of contained cations are shown in Table III.2 for the same amount of zeolite: about 70.7 g of the initial zeolite (sodium form) and 100 g of the final zeolite-occluded salt compound. The original zeolite contained about 0.5 mol of exchangeable sodium ions. The cations in the final zeolite-salt in excess of this value were those in the occluded salt. From a charge balance, it was calculated that the chloride content of the zeolite-salt compound should be 17 wt %; the results of two chloride analyses were 17.1 and 17.3%.

TABLE III.2. Concentrations of Univalent and Divalent Metals in Zeolites

	Concentration[a]						
Sample	Ba	Cs	K	Li	Na	Sr	Total
FR-8[b]	0.010	0.015	0.190	0.703	0.032	0.007	0.957
Anhydrous A50[c]	0	0	0	0	0.498	0	0.498

[a]Concentration units are moles per 100 g of salt equilibrated zeolite for FR-8, and moles per equivalent amount of anhydrous A50 zeolite (about 70.7 g A50). See text for further explanation.
[b]Final salt-equilibrated zeolite.
[c]Starting zeolite.

From the chemical analyses, it could not be determined which cation is in the zeolite structure and which is in the occluded salt. However, it is clear that sodium in the original zeolite has exchanged almost completely with other cations. In addition, the cations in the zeolite-salt were enriched in Li, Ba, Sr, and Cs compared to their concentrations in the original salt. This was also shown by the analyses of the salt that passed through the zeolite column. The amounts of Ba, Cs, and Sr in this salt were at or below their detection limits; the estimated decontamination factors were 640, >700, and >250, respectively.

The above results are encouraging. They demonstrate that zeolites can sorb the cations of interest. However, the matrix must also contain these cations when the waste form is eventually exposed to groundwater in the repository. Some short-term leach tests have been completed, and these results are also promising. The leach resistance of the washed and dried zeolites was measured for a 24-h leach period in terms of the percent released. The amounts of Ba, Cs, Li, K, and Sr released were <0.01, 0.06, 0.1, 0.01, and 0.01%, respectively. Thus, the zeolite matrix acts as a leach-resistant matrix under the conditions of the test.

The zeolite materials discussed above are in the form of powders, which would not be suitable for a high-level waste form. Laboratory work to identify a method for solidifying the zeolite-salt compounds is at a very preliminary stage. We have conducted experiments to test the feasibility of densifying a matrix consisting of zeolite and copper powders. Hot isostatic pressing of various mixtures at 375°C and 69 MPa (10,000 psi) yielded solid monoliths that were relatively strong. Further experiments are planned in which zeolites with sorbed salt will be hot isostatically pressed with copper powder.

Studies to determine the radiation resistance of zeolites with sorbed IFR waste salt are still in the planning stage. However, the radiation resistance of sodalite was studied by Thompson.[4] The results showed that exposure of sodalite to 1×10^{10} rad did not affect the sample volume or its leachability.

5. Regulatory Requirements for High-level Waste Disposal

Two wastes streams from the reprocessing of IFR fuels, salt and metal, might be classified as high-level wastes. In accordance with current waste-disposal philosophy, these wastes would be disposed of in a deep geologic repository. Thus, the producer of IFR reprocessing wastes must plan to comply with the requirements for HLW acceptance at a repository. To support such planning, information on the current status of HLW acceptance requirements was reviewed and analyzed to evaluate their applicability to IFR wastes. The results of reviewing and analyzing this information will be expressed in a document summarizing (1) the general background of standards, regulations, and current activities of waste producers and federal agencies, relative to preparations for disposal of HLW, and (2) conclusions about the regulatory requirements that might be demanded of the IFR waste producer and the IFR waste package.

References for Section III

1. J. R. Liaw and J. P. Ackerman, "PYRO-New Capability for Isotopic Mass Tracking in Pyroprocess Simulation," Intl. Conf. on the Physics of Reactors: Operation, Design, and Computation, Marseille, France, 2:XI-33 (April 23-27, 1990).

2. Y. I. Chang et al., "Integral Fast Reactor Program Summary Report, FY 1985-FY 1989," Argonne National Laboratory Report, ANL-IFR-125, p. 69 (January 1990).

3. I. Johnson, K. E. Anderson, and R. Claypol, "Chemical Engineering Division Summary Report--July, August, and September 1960," Argonne National Laboratory Report, ANL-6231, p. 67 (1960).

4. G. H. Thompson, "Evaluation of Mineralization Processes for SRP Wastes," Savannah River Laboratory Report, DP-1389 (1975).

IV. SAFETY EXPERIMENTS AND ANALYSES

A. Status of the EBR-II PRA

Argonne National Laboratory is currently performing a Probabilistic Risk Assessment of the Experimental Breeder Reactor-II (EBR-II). The main objective of the PRA is to develop a quantitative safety statement for EBR-II. This takes the form of a Level 1 PRA focusing on core damage frequency. Specifically, this involves identifying the dominant accident sequences in terms of core damage. This objective can be divided into two important separate sub-objectives, to quantify the detailed accident sequence frequencies and to quantify the associated conditional probability of core damage. The PRA process leads to identification of the important systems, components and human actions with respect to both sequence initiation and to mitigation. A containment study will be considered after completion of the Level 1 assessment. An important feature of the EBR-II PRA is that a seismic PRA effort was instituted in parallel with the internal events PRA. This was done because of the expected low frequency of internally initiated events.

Application of standard PRA methods to EBR-II introduces some special problems because of the unique features of the reactor and its mission. Because of the design of the reactor and the inherent transient reactivity feedbacks and heat removal capabilities, it has the capability to sustain many accident sequences without core damage. This capability has been demonstrated experimentally for the unprotected loss-of-flow and for the loss-of-heat-sink accidents[1] as well as many protected transients.[2] The mission of EBR-II as an irradiation facility introduces another unique problem in the PRA. In the general case, the EBR-II core may contain many experimental subassemblies along with the driver fuel. It has been found that the details of core composition do not have a major impact on the reactivity feedbacks; as a result the effect of core composition can be included in the uncertainties. However, the characteristics of different experimental subassemblies may require separate damage assessments for different irradiation experiments.

The primary motivation for this enterprise has been to provide a quantitative estimate of risk for the operation of EBR-II. However there are

significant insights to be gained for application to IFR design. Inasmuch as EBR-II is viewed as a prototype for an IFR, the identified sources of risk, and the demonstration of lack of sensitivity in various areas, can be used to guide the design and prove the performance of an IFR by application of risk-based methodology to studies of traditionally important areas such as electrical power dependence and sensitivity to human error.

1. Systems Analyses

Systems analyses have been completed on the following front line systems, the Reactor Shutdown System (RSS), primary pumps and motor-generator sets, shutdown cooling, and shield and thimble cooling. In addition, the three main support systems, electrical, instrument air, and water supplies have been analyzed. In EBR-II all systems, with the exception of the RSS, are continuously operating and thus are not demand systems. In general, therefore, the systems analyses are primarily used to identify and evaluate potential new initiating events.

2. Database

The data used to evaluate the system reliabilities and to establish initiating event frequencies come from a number of sources. For some initiating events the plant operating history directly provides the required frequency. For others the use of generic or LMR data is required. The LMR database CREDO[3] is being used to provide most of the pertinent data for system reliability.

3. Accident Sequence Analysis

Any LMR, in fact any reactor, utilizes a fundamentally simple safety design approach which can be described as follows; first, scram the reactor to ensure neutronic shutdown and second, provide means of removing decay heat. The complexity that arises in the study of accident sequences in LWRs springs from the hierarchy of redundant and diverse decay heat removal systems--ECCS, HPSI, etc.--required to prevent core damage in accident sequences. PRAs have identified dependencies on support systems, e.g., electrical power, which have translated to vulnerabilities to faults in those support systems. The

dependencies arise because the front-line systems are active, on demand, systems and therefore have a probability that they will not respond when required.

EBR-II is designed with the same simple safety design approach but a very different architecture. Just as in LWRs, a scram system is provided to shut off the nuclear chain reaction; but thereafter the decay heat removal is carried out by passive means, utilizing natural circulation. In the primary tank, if the primary pumps are not operating, natural circulation transfers heat from the core to the bulk sodium. Heat is extracted from the tank sodium by three separate routes. The main heat transport path is through the secondary sodium loop. In fact, if the secondary sodium is flowing under natural circulation conditions, the rate of extraction of heat is large enough to take the system into a cooldown. This is prevented by retarding the natural circulation flow by running the secondary electromagnetic pump backwards. Under certain conditions the secondary sodium flow is stopped in order to maintain the water level in the steam drum and the decay heat is removed by the two shutdown coolers. The shutdown coolers are independent, continuously operating, natural circulation driven NaK loops. The total heat removal by the shutdown coolers is 60 kW during normal operation, but when the bulk temperature rises from 700°F to 710°F, sets of louvers open automatically and the heat rejection rate increases. Thus, the shutdown coolers passively remove 60 kW but have an active element to activate the larger heat removal (360 kW). Finally there is a shield cooling system that removes 150 kW from the tank, but is dependent on electrical power being available.

Figure IV.1 is a very simple event tree which expresses the design approach above. Consider each of the three sequence types in this primitive tree. Under normal scram and normal decay heat removal there is no core damage. Given that scram occurs, then in the event of failure to remove decay heat there is a slowly developing long term core vulnerability. (Sequences of this type have traditionally proved to be the dominant sources of risk in LWR PRAs.) Failure to scram can lead to an immediate core vulnerable sequence. (This latter class of events is a historical area of emphasis in LMR safety analysis; it includes the study of HCDAs (Hypothetical Core Disruptive Accidents) such as Unprotected Loss-of-Flow and Transient Overpower.) The normal shutdown route of successful scram and successful decay heat removal could still lead to core

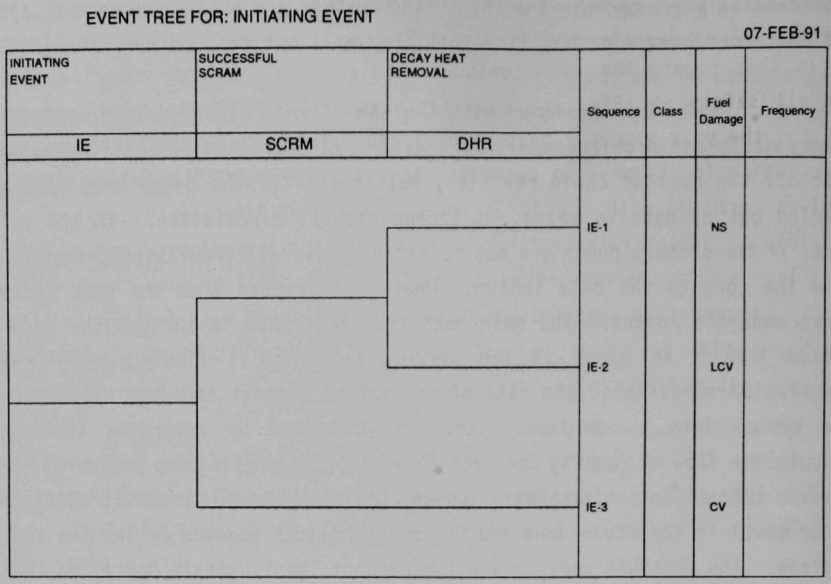

Fig. IV.1. Simple Event Tree

damage in the rare cases where the initiating event is extraordinarily severe and rapid such that the normal protective functions do not act to prevent overheating. Examples of such initiating events might be a large rapid reactivity insertion, instantaneous seizure of both primary pumps or a rapid and large loss of sodium from the primary tank.

Consider each type of sequence enumerated above and its contribution to the likelihood of core damage in EBR-II. Firstly, only a few of the latter very rare events have been identified that could conceivably lead to fuel damage, even given a scram. These events are inherently difficult to quantify but the PRA has shown that the annual frequency of this class of event is of the order of 10^{-8} or less for internal events. These initiating events are almost exclusively associated with some structural failures. Alternately earthquakes offer a credible means of causing structural failures at a frequency higher than 10^{-8} per year making the seismic portion of the PRA important in defining the overall risk.

In the sequences where the scram is successful but the ability to remove heat is degraded there is a potential long term core vulnerability. It is in this regard that some unique features of the design contribute to the overall safety of EBR-II. These features demonstrate one aspect of passive safety, the passive decay heat removal capability which is achieved by natural circulation in primary and secondary sodium and naturally circulating shutdown coolers combined with the large heat capacity of the primary system. It is possible to demonstrate that, with no heat rejection other than the parasitic heat losses from the tank, fuel damage will not occur for many days. Therefore it is to be expected that loss-of-heat-sink transients will contribute little to the final risk statement because there are no identified ways to defeat the passive heat removal and natural circulation.

The third class of sequences are the Anticipated Transient Without Scram (ATWS) events, for example Loss-of-Flow without scram. In the response to ATWS events EBR-II displays another aspect of passive safety in that, for many initiating events, even without scram the system can maintain power to flow balance using only the negative reactivity feedbacks inherent in the core. This property has been demonstrated directly in the Inherent Safety Demonstration Tests of April 1986.[1] It is of obvious interest to assess the reliability of the property of passive response to accidents in some way and express that in the language of a Probabilistic Risk Assessment.

The systems analysis of the scram system has provided a probability of failure to scram of typically 5×10^{-6} per demand. When combined with the initiating event frequency this results in sequences in this class of $\sim 7 \times 10^{-6}$ per year. However results of transient analysis using SASSYS indicate that only 1×10^{-6} per year of these transients will lead to any fuel damage. This result stems from the ability of EBR-II to survive most of these transients without fuel or structural damage.

4. Human Reliability

EBR-II has long maintained the position that safety of the plant is insensitive to human error. Analysis of potential initiating events has identified no new human error related events. Furthermore all the front line

systems which act to prevent core damage, with the exception of the RSS, are continuously operating. Repair and maintenance are carried out when shutdown, little or no on-line maintenance takes place, and therefore human error can essentially only contribute through the only demand system, i.e., via the scram reliability. Detailed human reliability analysis has shown that there is little dependency on human error.

5. External Events

The seismic portion of the PRA is being executed in parallel with the internal events study. A site specific hazard curve was commissioned based upon existing seismic surveys. The expected damage frequency for different generic plant level fragilities has been computed using representative randomness and uncertainty values. The resulting mean and median annual failure frequencies are shown in Table IV.I.

TABLE IV.1. Annual Failure Frequencies for Generic Fragilities vs. Peak Ground Acceleration (â) Using the EBR-II Seismic Hazard Curve

â (g)	Median	Mean
0.2	5.8×10^{-5}	1.5×10^{-4}
0.4	1.1×10^{-5}	3.9×10^{-5}
0.6	3.6×10^{-6}	1.7×10^{-5}
0.8	1.4×10^{-6}	8.1×10^{-6}
1.0	5.2×10^{-7}	4.0×10^{-6}

The mean failure frequencies clearly show that the damage frequency predicted due to earthquakes can be expected to dominate there from internal events. This result arises from the uncertainty in the seismic hazard evaluation, in particular, lack of knowledge of the return frequency of large, rare earthquakes.

Studies are in progress to establish the fragilities of important systems using combinations of expert judgment and deterministic calculation of

the response of specific systems. The reactor tank, containment building, and the shutdown coolers have been completed. Studies of the control rods, primary pumps, and reactor core are underway.

6. Summary

The EBR-II PRA is now entering a phase of intensive review by both EBR-II staff and independent reviewers. The results thus far have indicated a low frequency of all forms of damage from internal initiating events, 4×10^{-6}, with no single accident sequence or initiating event dominating the outcome. The hazard curve for the seismic analysis contains sufficient uncertainty that it will inevitably lead to a mean seismic induced annual failure frequency in the 10^{-5}-10^{-6} range. Core damage due to seismic induced failures can be anticipated to dominate the core damage frequency.

B. US/European Safety Study

Within the framework of a cooperative effort among European and U.S. LMR R&D organizations, a comparative study of the safety performance of metal and oxide-fueled core designs has been performed to analyze the response of the two fuel types during a range of accidents in a large (3500 MWt), pool-type, liquid-metal cooled reactor design. The emphasis in the analysis was to quantify the safety margins available with oxide and metal fuels when used in conjunction with design features that supply self-limiting reactivity responses to transient power-to-flow mismatches in accidents with failure to scram. The analyses considered three accident sequences: the unprotected loss-of-flow (ULOF) sequence, in which power to all pumps is lost; the unprotected transient overpower (UTOP) sequence, in which one or more inserted control rods are inadvertently withdrawn; and the unprotected loss-of-heat-sink (ULOHS) sequence, in which all normal heat removal capability is lost. The initial conditions for all transients were taken to be the normal operating conditions (full power and flow) at the end of equilibrium burnup cycle (EOEC), and all analyses were conducted on the basis of best-estimate phenomenological modeling assumptions.

1. Unprotected Accident Calculations

The principal goal of this study was to determine the generic differences between the safety performance of oxide and metal-fueled 3500 MWt reactors. To that end, the core designs described in Sect. V.A in a pool-type primary circuit plant design were analyzed to determine their responses to three unprotected accident initiators: the unprotected loss-of-flow (ULOF), the unprotected transient overpower (UTOP), and the unprotected loss-of-heat-sink (ULOHS).

The unprotected loss-of-flow accident is assumed to be initiated by a total loss of offsite power. This causes the electrical power to be lost to all primary pumps, intermediate loop pumps, and feedwater pumps. In addition, it is also assumed that there is a failure to scram the reactor, so that the reactor power changes only in response to the reactivity feedbacks introduced as a result of the electrical power loss. The primary and intermediate loop pumps coast down according to their inertial characteristics only, which are assumed to provide an initial flow-halving time in both cores of 8 sec in the primary loop and 6 sec in the intermediate loop. The reactivity transient that results in the oxide core design is depicted in Fig. IV.2.

In the pump coastdown transient with the oxide-fueled core, as the core flow drops, the coolant outlet temperature rises. With this temperature

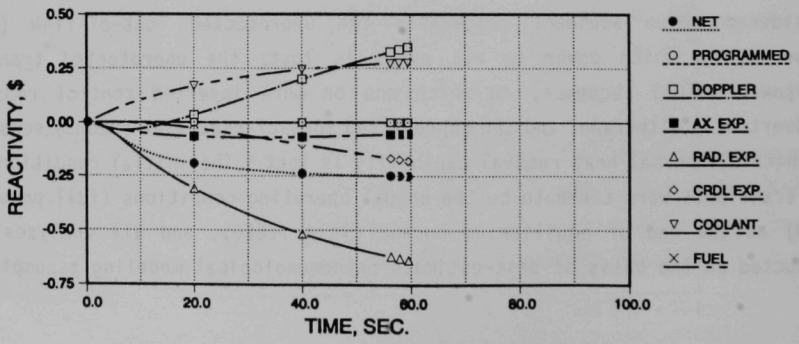

Fig. IV.2. Oxide Core ULOF Reactivity History

increase, the coolant density decrease introduces a positive reactivity effect, and thermal expansion of the above-core structure spreads the core, introducing a negative reactivity effect. The net negative reactivity reduces the reactor power, chilling the fuel and causing a positive Doppler reactivity feedback. Thermal expansion of the fuel and cladding reduces the effective core fuel density as the swollen, irradiated fuel, wedged within the cladding, is elongated axially, giving a slightly negative reactivity feedback. As the heated coolant washes the control rod drivelines above the core, they expand and marginally increase the absorber insertion, giving a negative reactivity feedback. Although the net effect of these feedbacks is negative, the power reduction is insufficiently fast to counter the flow rundown, power/flow increases and coolant boiling in the core begins at 56 sec after accident initiation. From this point on the accident would proceed into loss of cooling and core meltdown.

Results from analysis of the unprotected loss-of-flow accident in the metallic fueled core design are shown in Figs. IV.3 and IV.4. Compared to the oxide reactivity feedbacks, the metal core yields a much reduced positive Doppler feedback, due to the fact that the high fuel thermal conductivity gives a normal fuel operating temperature only around 200°C above the coolant temperature. As the power reduction decreases the fuel temperature to near the coolant temperature, comparatively little Doppler feedback is available to retard the power decrease. The power reduction is sufficiently fast to avoid coolant boiling in the hottest fuel assembly (see Fig. IV.4) with a margin of around 150°C.

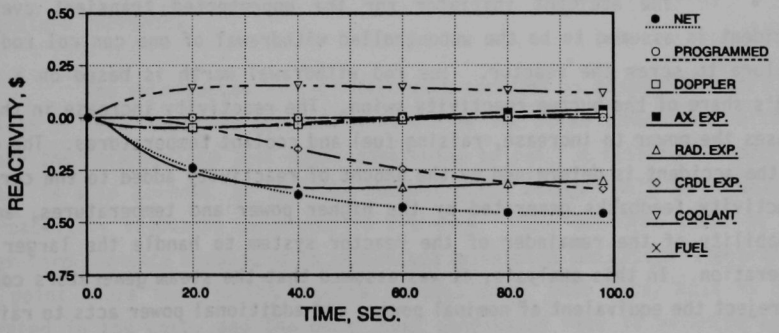

Fig. IV.3. Metal Core ULOF Reactivity History

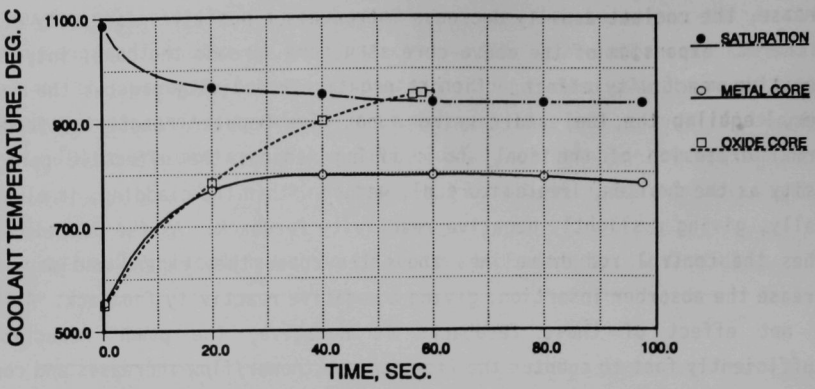

Fig. IV.4. Metal and Oxide ULOF Peak Temperature Histories

A number of parametric sensitivity calculations were carried out to determine the variability of the ULOF results with changes in input assumptions (pump coastdown rate, material thermo-physical properties, reactivity feedback coefficients) to reflect uncertainties. It was found that for the oxide core, a non-boiling ULOF response was obtainable by assuming a three-fold increase in the control rod driveline expansion coefficient. On the other hand, the metal core results proved to be relatively insensitive to large changes in most of the input assumptions away from the optimized design, with the potential for significant increases in safety margins by modest extension of the pump coastdown time.

The accident initiator for the unprotected transient overpower accident is assumed to be the uncontrolled withdrawal of one control rod, with failure to scram the reactor. The rod withdrawal worth is based on a single rod's share of the burnup reactivity swing. The reactivity increase in the core causes the power to increase, raising fuel and coolant temperatures. The course of the accident is determined by the amount of reactivity added to the core, the reactivity feedbacks generated by the higher power and temperatures, and the capability of the remainder of the reactor system to handle the larger power generation. In this analysis, it was assumed that the steam generators continue to reject the equivalent of nominal power, and additional power acts to raise the secondary coolant return temperature, and thence the primary coolant temperature.

The coolant temperature increase introduces negative reactivity feedback that counters the rod withdrawal reactivity, and acts to return the core power to balance the available heat rejection rate once the rod withdrawal is completed. At final equilibrium, the entire system is at an elevated tempeature compared to the normal operating condition. Table IV.2 contains a summary of UTOP results for the oxide and metal fueled core designs.

Table IV.2. Unprotected Transient Overpower Accident Results

	Oxide	Metal
Reactor State	BOEC	EOEC
Rod Withdrawal		
Rate, $/sec	+0.005	+0.005
Worth, $	+0.10	+0.11
Peak Power, P/P_o	1.08	1.17
Peak Coolant Temperature Rise, °C	18	40

As these results show, the temperature increases associated with this accident are inconsequential for both fuel types. The key to avoiding core disruption is the small size of the rod withdrawal worth, which comes about due to the good breeding capabilities of these designs and the resulting low burnup reactivity swings. Consideration of control margin increments to accommodate uncertainties would increase the rod withdrawal worths and the size of the temperature increases.

The unprotected loss-of-heat-sink accident is assumed to start with the loss of heat rejection capability at all of the steam generators, with the primary and intermediate loop pumps continuing to run. A failure to scram the reactor is also assumed, so that the reactor power changes only in response to the reactivity feedbacks generated in the core. This accident tends to be a longer-term sequence because it is terminated by raising the system temperatures to a point where the fission process is shut down, only decay heat is being generated in the core, and the decay heat generation rate is balanced by the capacity of the decay heat removal systems. Figure IV.5 contains time histories

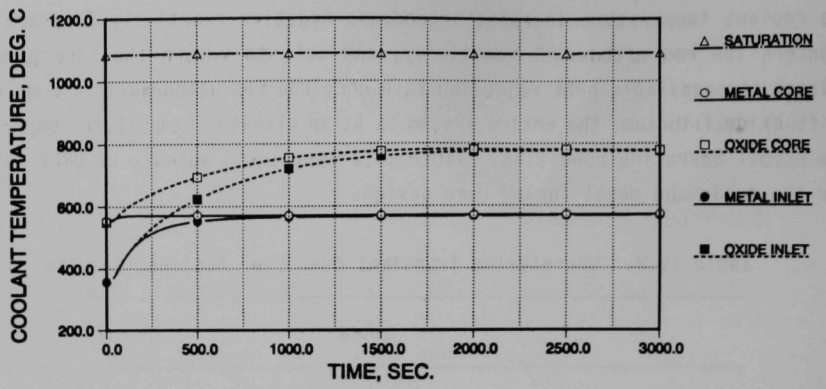

Fig. IV.5. Metal and Oxide ULOHS Core Inlet and Outlet Temperature Histories

of the core inlet and peak coolant outlet temperatures for this accident sequence for both oxide and metallic fuel designs. As in the unprotected loss-of-flow sequence, the more favorable Doppler feedback due to the high thermal conductivity metallic fuel results in a faster power reduction, and a lower temperature quasi-equilibrium state.

2. Conclusions

The results of this comparison study reflect the basic thermal, mechanical, and neutronic performance differences of oxide and metal fuels. Metal fuel has an effective thermal conductivity that is nearly an order of magnitude larger than that of oxide fuel. This results in much lower operating temperatures in metal fuel and a lower stored energy during operation. In addition, the lower metal fuel temperature results in a lower Doppler reactivity to overcome on startup, yielding a reduced control reactivity requirement, and a reduced positive feedback to be overcome on power reduction, either upon scram or in an unprotected accident. Because metal fuel gives a harder (higher energy) neutron spectrum due to the absence of light-weight moderating isotopes, the fertile-to-fissile conversion is increased compared to oxide fuel. This further reduces the control reactivity worth requirement. The harder spectrum also leads to an increased positive coolant density reactivity and a decreased reactor Doppler feedback coefficient.

Analyses show that in unprotected loss-of-flow and loss-of-heat-sink sequences, metal-fueled liquid-metal-cooled reactors with pool-type primary systems provide larger temperature margins to coolant boiling than are available with oxide fuel.

C. Predicting Margins and Uncertainties for Unprotected Accidents Using Measurement Based Methods

It has been proposed that the technical specifications upon which an IFR reactor be licensed should include a requirement for demonstrability of safe inherent shutdown. This stems from the present thinking that the concept of inherent safety is an integral part of the plant safety posture and that credit for the associated risk reduction should be taken in the plant safety analysis upon which the reactor is licensed. The situation is analogous to that which exists for current commercial reactors. These plants are licensed under the provision that the Engineered Safety Features be periodically tested and shown to work. In the case of the IFR, since the mechanisms for passive shutdown are an inherent part of the reactor, it should be possible to test these mechanisms at normal operation without having to reconfigure the alignment of the plant as is the case for existing commercial plants. The work reported here in fact indicates that such non-intrusive methods will be sufficient to determine whether the feedback mechanisms giving rise to a safe shutdown capability are indeed in place in the operating plant.

The demonstrability of a passive shutdown capability when done a priori by means of calculating is potentially complicated by a plethora of uncertainties associated with predicting life cycle effects and the values of engineering design parameters. Some of the more difficult tasks include: predicting number densities as a function of burnup, predicting mechanical interaction between fuel and cladding as a function of burnup, predicting reactivity effects associated with radiation induced geometry changes, and characterizing how manufacturing tolerances affect the hot clean k_{eff} of the core. When the only means for estimating these uncertainties are a priori calculations performed without reference to current operating data, then significant derating of the reactor could be required so as to guarantee successful inherent shutdown. The apparent solution is, in addition to estimating these uncertainties a priori, to actually measure their net effect on the reactor state once the reactor is operating.

It is from this background that a method has been developed to demonstrate from plant measurements the extent of the passive shutdown capability that is in place.

The scope and complexity of the task is simplified by the following two observations. First, the region of space over which measurements need to be collected and processed is limited to the envelope surrounding the core. The reason is as follows. The behavior within this envelope is affected by only three boundary conditions--reactor flowrate, reactor inlet temperature and external reactivity. In turn the behavior of these boundary conditions is encompassed by five transient classes--loss of flow, loss of heat sink, rod run out, primary pump overspeed and chilled inlet temperature. For each class, simple methods exist for determining a priori the limiting behavior of the boundary conditions. Therefore, if a model for the processes within this envelope can be obtained from current measurements, then the current response of the core for these five transient classes can be calculated on-line yielding the status of the inherent shutdown capability. The present task then reduces to one of obtaining a model for the processes inside the envelope using measurements obtained by non-intrusive means.

The second observation is that the important safety related features of the reactor response--temperature rise and power--correlate, at least to the first order, with just a few parameters. The values of these parameters can be determined from measurements in an empirical manner without having to decompose the parameters into their underlying constitutive components. The nature and origin of these parameters is made more clear by separating the behavior of the core into quasi-static and dynamic components as follows. On the time scale that primary flow, rod position and inlet temperature change during ATWS events, all reactivity feedbacks with the exception of the one group neutron precursor population behave quasi-statically. The coolant temperature, the cladding temperature, the fuel temperature, the temperature of core structures (hex can and load pads) and the grid plate temperature all remain essentially in instantaneous equilibrium with the power, the flow rate and the inlet temperature. (Actually, the control rod time constant can range between 10 and 30 sec, which is decidedly not quasi-static. However, treating it as quasi-static only increases the width of the confidence bands on the core response

prediction, but does not invalidate the method.) When all reactivity feedbacks but the precursor population are in equilibrium with the instantaneous power, flow and inlet temperature, the net reactivity can be written as

$$\rho = A(1 - \bar{P}) + B\left[1 - \frac{\bar{P}}{\bar{W}}\right] + C\delta T_i + \rho_{ext}$$

where

$\bar{P}$ = normalized power,

$\bar{W}$ = normalized flow rate,

δT_i = reactor inlet temperature change for normal,

ρ_{ext} = external reactivity,

and where A, B and C are integral parameters that are functions of the reactivity feedback coefficients for fuel temperature, cladding temperature coolant density and structure temperatures. The dynamic behavior of the plant is then well approximated by

$$[\rho - 1]\frac{d\bar{P}}{dt} + \left[\frac{d\rho}{dt} + \lambda\rho\right]\bar{P} = 0$$

where

λ = one group neutron precursor decay constant.

Thus, the current state of the reactor, including those phenomena we have a difficult time calculating accurately--fuel-cladding mechanical interaction, number density dependence on burnup and reactivity effects associated with radiation induced swelling--are embedded in the measured values of the four parameters A, B, C and λ.

At the heart of the method is a technique for estimating these integral parameters from measurements taken from the operating reactor. The values for these parameters and the variance of their uncertainty are chosen to maximize the likelihood that the above equations produced the measurements. In locating this maximum, a search over the parameter space is performed. To make the search more tractable and to guarantee a unique set of parameter values, the optimization is decomposed into several optimization subproblems. First, a quasi-static transient is used to identify values for the subset of parameters A, B and C. Once these values are known, a dynamic transient provides the value for λ. Second, for each transient, these values are gotten using a least squares criterion that does not depend on the variances. These estimated values are then held fixed and their associated variances are estimated by maximizing the likelihood that the above equations generated the data.

To provide a starting point for the testing and demonstration of the method at the EBR-II plant, the method was evaluated by processing simulated measurements of the EBR-II reactor. The simulations were limited to the study of the effect of primary flowrate on reactor behavior; the effect of external reactivity and inlet temperature are to be studied in future work. Even though the simulation was relatively simple--it consisted of the point kinetics equation with one precursor and the prompt jump approximation and a lumped parameter equation for the control rod--it describes the core response to a loss of flow observed in EBR-II quite well.

The method was applied to these simulated measurements with the problem partitioned as described earlier. The quasi-static transient involved ramping flowrate from 100 to 85% and back again over a period of 1 h. The dynamic transient was driven by this same flow with a 10% peak-to-peak pseudo-random binary signal superimposed on this.

The success with which the methodology correctly identified the core dynamics is evident in Fig. IV.6. The figure compares for a loss of flow event the prediction generated by the core model containing the A, B, C and λ identified from measurements, termed the "identified" model, with the "actual" plant response. The dotted lines show the three-sigma confidence level predicted by the identified model; the solid line is the actual plant response, that is,

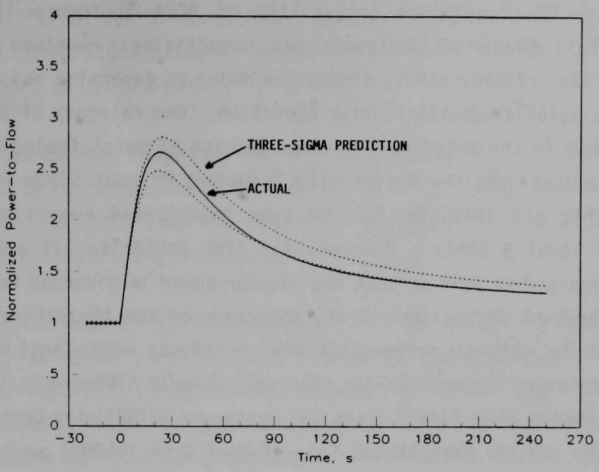

Fig. IV.6. Three-sigma Power-to-flow Uncertainty Prediction for Flow Coastdown

the response from the model used to generate the simulated measurements. The solid line is seen to generally fall within the dotted lines as it should.

The results for the simple case described above are encouraging. Work is under way to test the method using simulated measurements generated by the more detailed models in the SASSYS code. The method is to be eventually tested in EBR-II.

D. Fuel Damage During Off-Normal Transients

In order to assure that fast reactor fuel and blanket pins operate safely over their lifetime, certain design limits have been developed to assure cladding integrity is maintained through normal operation (level A), anticipated faults (level B), and unlikely faults (level C). In addition, the less stringent criterion that the core geometry remain coolable has been established for extremely unlikely faults (level D) that represent limiting cases of failure that are within the design basis of the plant. Severe accidents where double faults are postulated are considered to be of extremely low probability and are therefore Beyond Design Basis Accidents (BDBAs).

Although the cumulative probability of BDBA accidents is very small ($<10^{-6}$/yr), this class of accidents has nevertheless received considerable attention in fast reactor safety studies in order to determine any residual risk to the public associated with reactor operation. One category of BDBAs that has been emphasized in the assessment of the response of metal-fueled fast reactors to severe accidents are the Anticipated Transient Without Scram (ATWS) events. These accidents are initiated by the same anticipated events as those that comprise the level B DBA's. However, for ATWS accidents all automatic scram systems are assumed to fail so that the reactor power is governed only by passive reactivity feedback mechanisms. A key objective of the innovative fast reactor designs is to be able to accommodate ATWS accidents with limited core damage through the inherent response of the reactor. Generic ATWS events that have been studied include the Unprotected Transient Overpower (UTOP), the Unprotected Loss-of-Flow (ULOF) and the Unprotected Loss-of-Heat Sink (ULOHS) accidents.

Another category of BDBA plant transients that has received considerable attention in the IFR program are accidents involving Shutdown Heat Removal System (SHRS) failures. Here again multiple faults are assumed so that the Normal Decay Heat Removal System (NDHRS) and Direct Reactor Auxiliary Cooling System (DRACS), if included in the design, are lost and the Reactor Vessel Auxiliary Cooling System (RVACS) is partially blocked. At issue here is fuel damage over long times (hours) at decay heat levels so that it makes little difference whether the reactor was shut down by the scram system or by the passive reactor response to an ATWS event.

1. Thermal Response of Metallic Fuel Pins

The thermal response of metallic fuel pins to whole-plant transients depends on the reactor design. The approach to assessing fuel damage outlined here is sufficiently broad to cover the full range of transient response for the different design variations. This approach also covers regimes beyond the expected thermal response in order to address uncertainties and to quantify margins to fuel failure. However, because the reactor designs are continuing to evolve, it is not possible to focus on any one set of calculations as representing the thermal response of the fuel under all DBA and BDBA transient conditions. Instead, groups of results are collected on a common basis and viewed from the standpoint of fuel damage regimes. Although the details of such

results are different for different reactor designs, the overall trends and time scales of the temperature history regimes are similar and representative of the general response of an IFR metal-fueled reactor.

The thermal responses for the protected transients can generally be characterized by a temperature ramp of 1-100 K/sec which reaches a peak in several seconds. At that time the reactor is scrammed and cladding temperatures drop below normal operating conditions within 10 sec.

The cladding temperatures for ATWS events generally increase up until about 50 sec, at which point passive reactivity feedbacks turn the transient around. After several hundred seconds thermal expansion of the core and control rod drive provide sufficient negative reactivity to bring the reactor to a quasi-equilibrium state at elevated temperatures. For longer times the temperatures depend on the availability of the shutdown heat removal systems.

Long-term (10's of hours) cladding temperatures are governed by the decay heat removal capacity. Under normal conditions the decay heat is rejected through the steam generator system. However, loss of the NDHRS and loss of the NDHRS plus the DRACS are design basis accidents (levels B and C, respectively). If both the NDHRS and DRACS are unavailable the decay heat is removed by the RVACS.

The long-term cladding temperatures following shutdown heat removal system failures again depend on the reactor design. During this time the reactor is subcritical, either due to scram or due to passive negative reactivity feedbacks. If scram is achieved, this phase will end when the decay heat drops below the heat rejection capacity. Even for the case where no backup heat removal is available the heating rate is such that operator intervention to establish emergency cooling within 10 to 12 h may prevent excessive core damage.

2. Cladding Damage Mechanisms

Cladding damage during the transients discussed in the previous section can occur by metallurgical changes and by mechanical loading. Both mechanisms tend to be very strong functions of the temperatures. Metallurgical damage includes microstructural changes (e.g., recovery and recrystallization),

alloy depletion, fission product attack and fuel-cladding metallurgical interaction. Mechanical damage occurs primarily by creep deformation resulting in grain boundary cavitation and/or local instabilities in the plastic deformation.

Alloy depletion and fission product attack are usually modeled as cladding wastage. The affected zones are assumed to be strengthless so that the entire cladding load is carried by the unaffected cladding tendon. The rates are such that most of the wastage occurs during steady-state operation.

Metallic fuels also interact metallurgically with the cladding. A diffusion zone between the fuel and the cladding may form during steady-state operation. The affected zone in the cladding is again assumed to be strengthless. Additional attack during accident transients is usually too slow to be of interest unless eutectic melting occurs. However, if liquids do form at the interface the eutectic penetration rates can be many orders of magnitude more rapid and significant transient thinning of the cladding wall may occur.

The tendon that has not suffered severe metallurgical damage must carry most of the mechanical loading on the cladding. Depending on the duration and intensity of the loading and the temperature transient, damage to the load-bearing tendon may lead to cladding breaches or may significantly reduce the ability of the cladding to withstand further damage. At the high temperatures of interest to safety analysis most of the mechanical damage is related to creep. Creep deformation can cause grain boundary cavitation which results in pinhole leaks that eventually coalesce into longitudinal fissures in the cladding. Creep deformation also thins the cladding wall which may result in local plastic instabilities (bulges) and rupture.

At about 1-2 at.% burnup structural traps (e.g., grain boundaries) for fission gas become saturated and the excess gas is collected in larger pores, which are the dominant cause of fuel swelling. These pores grow by collection of gas until the swelling is sufficient both to close the fuel-cladding gap, and also to cause interconnection of the porosity.[4] After the gap closes, and during most of the fuel lifetime, each axial elevation of the fuel contains porosity that is connected to the plenum, so that the pressure in this open porosity is nearly equal to the plenum pressure. So long as the fuel contains large pores

that are at the plenum pressure, fuel creep into these pores during steady-state irradiation is sufficiently rapid to maintain the entire fuel cross section in a state of hydrostatic stress equal to the plenum pressure. The cladding loading prior to transient heating, therefore, tends to be nearly uniform along the entire pin.

Transient heating of high burnup fuel also produces cladding loading that is dominated by the plenum pressure. The similarity of the fuel and the cladding thermal expansion and the compliance of the porous fuel lead to negligible Fuel-Cladding Mechanical Interaction (FCMI) cladding damage. Although the FCMI stresses in the cladding may be sufficient to yield the cladding early in the transient, little plastic strain accumulates before the fuel is sufficiently hot that fuel creep relaxes the cladding loading to a hydrostatic state that follows the transient increase in plenum pressure.

3. Models for Fuel Damage

The LIFE-METAL[5] and FPIN2[4,5] computer codes have been developed to model the thermal mechanical behavior of IFR metallic fuel pins. These codes are intended to provide the "state-of-the-art" understanding of metal-fuel damage and provide reference analyses against which simpler, but less general, models may be tested.

The LIFE-METAL code is used for the analysis of metallic fuel pins under operational conditions, while FPIN2 is used to analyze accident conditions. Although there is some overlap in capabilities for handling off-normal conditions, the emphasis in the development and validation of the codes is very different. LIFE-METAL has focused on steady-state fuel behavior, while for FPIN2 the focus has been on transient fuel behavior. The codes use different numerical analysis methods, but LIFE-METAL and FPIN2 use a common set of material properties. LIFE-METAL incorporates detailed models for predicting steady-state fuel behavior, but does not include detailed high-temperature fuel behavior models for accident analysis (e.g., fuel melting). FPIN2 incorporates models related to accident analysis but requires the user to provide input data describing the pretransient/steady-state conditions. This input can be obtained from LIFE-METAL calculations or data (e.g., fuel geometry, fuel microstructure, fission gas remaining in the fuel) from sibling pins. For design calculations,

LIFE-METAL output is the preferred method of determining FPIN2 initial conditions, as LIFE-METAL has been validated to groups of fuel pins, each group having a common fuel composition and operating history. For detailed single-pin analysis of transient tests (e.g., TREAT), the preferred option is to use data from sibling pin(s) to provide the initial conditions.

4. Model Validation

The current IFR experiment program for validating models for metallic fuel damage during off-normal transients includes the out-of-reactor Fuel Behavior Test Apparatus (FBTA) and Whole Pin Furnace (WPF) tests and the in-reactor TREAT and EBR-II transient tests.

The FBTA tests provide[6] the primary source of data on the metallurgical interaction between metallic fuels and cladding. In these tests (formerly designated as DEH tests) ~8 mm-long segments of irradiated fuel are heated by a computer-controlled infrared radiant furnace at a specified temperature and test duration. Included in the measurements are the temperature for the onset of melting at the fuel-cladding interface and the rate at which the melt penetrates the cladding. With some exceptions, the penetration rate results tend to follow the correlation given previously.[7] Separate experiments have also been run which validate the assumption in the modeling that the rate is almost constant at constant temperature.

A new WPF[8] fuel pin test system has recently been put into operation in the Alpha-Gamma Hot Cell Facility at Argonne National Laboratory (see Sect. IV.E). The furnace in this system is similar to the FBTA furnace but is much longer allowing the testing of intact irradiated IFR fuel pins. The first three tests, FM-1, FM-2, and FM-3 have subjected low burnup EBR-II pins to transients consisting of a temperature ramp from 773 K to 1073 K at 6 K/sec followed by a temperature hold at 1073 K until cladding failure is detected. Although external heating is used in these tests the calculated temperature profiles are almost flat because of the excellent thermal conductivity of metallic fuels. Such flat profiles are nearly prototypic of accident scenarios at decay heat levels. Furthermore, unlike oxide fuels, the temperature drop across metallic fuels is not large (a few hundred degrees Kelvin) even at full power so that WPF results are applicable to a wide range of transients.

The only way to achieve fully-prototypical transient testing of IFR fuel pins is to use in-reactor nuclear heating with flowing sodium coolant. The TREAT reactor is being used by the IFR program to provide such data for short-term transients. The aim of the experiments[9] run thus far, designated tests M2-M7, was the study of cladding failure threshold and other safety-related phenomena during simulated transient overpower (TOP) accidents. Specifically, the data needs addressed by the TREAT tests were: 1) determination of margin to failure and identification of underlying mechanisms, 2) assessment of pre-failure axial expansion as a potentially significant pre-failure reactivity removal mechanism, and 3) preliminary assessment of post-failure events; behavior of disrupted fuel and coolant. In general, the TREAT tests have confirmed the fuel damage models outlined previously. The tests also confirm that IFR fuels have a large margin to failure under transient overpower conditions; the failure threshold power with the 8 sec period overpower conditions tested was about four times nominal power over a wide range of burnups and fuel types tested.

EBR-II has been used in the past to perform operational transient testing of oxide fast reactor pins under slow ramp-rate conditions. Similar tests could also be run for metallic fuels. The EBR-II overpower transients are run with fuel that has been irradiated in a low-power EBR-II core position and then shifted to a high power position. Following an additional period of steady-state irradiation at the same pin power but at a reduced EBR-II power, the transient is then run by ramping EBR-II to full power. In this mode of operation power transients of up to 100-150% overpower can be achieved at rates up to 10% per second. Elevated temperature EBR-II tests at constant power are also of interest to the assessment of transient fuel damage because ATWS events shown tend to reach a quasi-equilibrium state where the temperatures are changing slowly over long periods of time. An example of this type of test is the EBR-II XY-22 eutectic penetration experiment.[10] In this test fuel pins with burnups between 0.0 and 7.7 at.% were irradiated for 42 min at elevated cladding temperatures of around 1070 K. The measured penetration rates were in general agreement with the models and the out-of-reactor data.[7]

E. The Whole Pin Furnace System

The new Whole Pin Furnace (WPF) system installed in the Alpha-Gamma Hot Cell Facility (AGHCF) at ANL-E is being used to perform out-of-reactor tests on

intact, EBR-II-irradiated IFR fuel pins. Objectives of the test program are to (1) study the behavior of irradiated fuel pins under simulated reactor accident conditions with emphasis on long-term (minutes to days) loss-of-flow and/or loss-of-heat sink types of events; and (2) provide data for the validation of fuel-pin models in the FPIN-2 and the LIFE-METAL codes. The ability to conduct long-term overheating tests on irradiated metal fuel pins in the WPF system essentially bridges the gap between the short-term (seconds) transient overpower experiments in TREAT and relatively low temperature, inherent safety demonstration experiments in EBR-II.

Out-of-reactor heating tests provide an effective and economical means to study the behavior of irradiated materials, particularly under potential reactor accident conditions during which transient high temperatures tend to overwhelm neutron-irradiation effects. Heating tests performed on cladding from oxide fuel pins in the Fuel Cladding Transient Tester (FCTT)[11] and on segments from metal fuel pins in the Fuel Behavior Test Apparatus (FBTA)[12] are examples of separate-effects studies performed on preirradiated fuel. The FCTT tests investigated stress-rupture behavior of irradiated cladding tubes, and the FBTA tests evaluated penetration of cladding due to fuel/cladding eutectic interactions. The WPF system permits testing of intact, irradiated fuel pins to assess the synergistic roles of fission-gas pressure and fuel/cladding eutectic interaction on fuel-pin failure.

The WPF tests generally fall into one of the two following categories: (1) run-to-cladding breach tests, and (2) safety demonstration, i.e., proof tests. The run-to-cladding breach tests typically employ a temperature-time condition in which the fuel pin is heated, at a controlled heating rate, to a target temperature and held until the cladding breaches. The tests provide information on the combined effects of the two cladding failure mechanisms in metallic fuel pins: cladding thinning by fuel-cladding eutectic formation, and cladding overstress by fission gas pressure loading. Information on axial fuel redistribution is also obtained.

The proof tests typically employ a temperature-time profile that envelopes the cladding temperature-time history anticipated in an accident event. The tests are designed to demonstrate that the fuel pin can survive the enveloping event with no breach, and that the cladding strain and wastage are tolerable.

Data from both test categories are needed for (1) validating the cladding failure models and correlations, and (2) supporting the safety evaluation of fuel designs, e.g., EBR-II Mk-V and ALMR fuels.

System Description

The major components of the WPF system (as shown in Fig. IV.7 before installation in the Alpha-Gamma Hot Cell Facility AGHCF at Argonne) are an in-cell furnace rig, a furnace control and data collection system, and a fission-gas measurement system (not shown). Ancillary components of the WPF system include a glycol/water heat exchanger for cooling the furnace body and nitrogen and helium gas supplies for lamp cooling and environment control.

The in-cell furnace rig consists of a test section and a furnace mounted on a self-propelled, remotely operated cart. The test section, (see Fig. IV.8) containing an irradiated fuel pin, is a 122-cm-long stainless steel tube assembly that is normally evacuated and sealed during a test. Two pressure transducers at the top of the test section provide the means for pin breach detection by measuring the pressure rise due to fission-gas release into the sealed system. Temperature along the length of the pin is measured by six Type-K thermocouples located at different elevations in the annulus between the irradiated fuel pin and stainless steel tube. A Type-S thermocouple, welded on the outside of the stainless steel tube, serves as the control thermocouple for maintaining the desired test temperatures. Outside the stainless steel tube is a quartz tube that provides a channel for helium cover gas flow, which provides an inert atmosphere for the test section during the test.

The furnace is a 65-cm-long radiant heating chamber powered by four longitudinal infrared-filament lamps. Highly reflective curved surfaces behind the filaments focus the radiant energy onto the centerline of the furnace where the test fuel pin is placed. The furnace is capable of continuous high-temperature (1100°C) operation for extended periods, with a short-term capability up to 1650°C. Low-mass lamp filaments and efficient energy focusing permit a rapid specimen temperature rise, up to 30°C/sec, depending on the specimen size. Motorized lift and manual slide mechanisms on the cart are used to support, align, and adjust the position of the test section and fuel pin within the furnace.

Fig. IV.7. Major Components of Whole Pin Furnace Test Apparatus

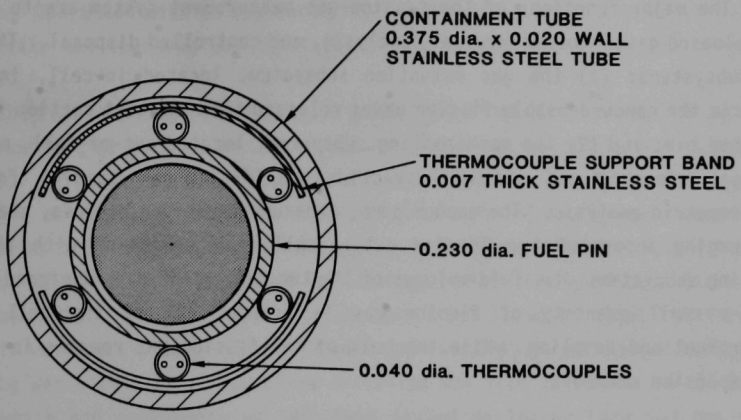

Fig. IV.8. Test Section of the Whole Pin Furnace Test Apparatus

Control of the furnace, based on feedback of a control-thermocouple, is administered by a microcomputer using commercially available software. In the closed-loop feedback algorithm, the control-thermocouple temperature is compared, at a regular time interval, with the desired temperature profile, which could be a flattop, a ramp, or a specific profile that simulates a given reactor transient event. The microcomputer also performs the functions of data acquisition and storage. Key test parameters are graphically displayed on a monitor to exhibit real-time test progression.

To permit unattended WPF operation for up to several days, furnace trips governed by hardware and software mechanisms, some of which are redundant, are provided. Trip initiators under normal conditions include high test-section pressure (i.e., cladding breach detection) and expiration of the desired test duration. Trip initiators under abnormal conditions include high/low control-thermocouple temperatures, high furnace power, high coolant temperature, and low coolant flow rates. Protection of the hot cell and the system are the primary functions of the latter trip initiators. A manual scram ability is provided for operator intervention.

The major functions of the fission-gas measurement system are to collect the released gases for measurement, analysis, and controlled disposal. There are two subsystems: (1) the gas retention subsystem, located in-cell, initially collects the noncondensable fission gases released into the test section from the breached pin; and (2) the gas-sampling subsystem, located out-of-cell, measures the gas pressure and allows extraction of fission-gas samples for mass spectrometric analysis. The vacuum pump, pressure measuring devices, and system gas-purging apparatus are located out-of-cell in conjunction with the gas-sampling subsystem. Manifold volumes of the two subsystems were designed so that only a small quantity of fission gas is brought out of the cell during measurement and sampling, while the bulk of the fission gas remains in-cell in two expansion chambers.

Performance Characteristics

Every phase of the WPF operation was thoroughly checked during out-of-cell acceptance testing before the furnace rig was installed in-cell. The fission-gas measurement system underwent leak and pressure tests, manifold volume calibration, and gas collection and measurement trials, all using helium and argon as substitutes for fission gas. After the furnace rig was installed in the cell, a series of in-cell acceptance tests was conducted to verify system leak tightness, remote operation, and sensor functions. As a result of the thorough out-of-cell checkout, only minor procedural modifications were needed to improve in-cell operation.

Thermal performance of the furnace and the pin breach detection system were two crucial areas that were checked in depth. Results obtained from the characterization of these areas are summarized below.

The thermal performance of the WPF system was characterized in more than 60 out-of-cell checkout runs, most of which used an evacuated test section containing a dummy fuel pin identical in nominal dimensions to an irradiated IFR fuel pin. Early tests established that heat transfer to the pin would not be significantly degraded if the test section was evacuated rather than containing a heat-conducting gas. The normal mode of operation is with an evacuated test

section. Operation with an evacuated test section increases pressure-transducer sensitivity and improves the quantitative analysis of released fission gases.

The major purpose of the thermal performance checkout runs was to determine the parameters to be used in the closed-loop feedback algorithm for temperature control. Criteria for desirable thermal performance were a controlled ramp rate between 5 to 10°C/sec, a stable tracking within 5°C of the target temperatures (as indicated by the control thermocouple) in the range of 600 to 925°C (similar to those of the FBTA tests), and an overshoot of the target temperature of no more than 15°C. The results of the checkout runs indicated that the first two criteria were easily met; ramp rates were 4.5 to 7.3°C/sec and target temperature tracking was within 2°C. The third criterion was also satisfied in all but two runs, which had overshoots of 18°C that lasted no longer than 150 sec before returning to a stable target temperature.

The steady-state furnace temperature profile for an 800°C target temperature indicated an approximate 120°C difference between the temperature at the mid-height of the furnace and at 3 cm above the bottom of the furnace heating zone. In an actual test, the relative position of the fuel pin within the furnace can be adjusted (by raising or lowering the test-section support platform on the furnace cart) to match the anticipated axial temperature profile for a given portion of the fuel pin in a given reactor transient event.

The sensitivity and response time of the WPF system in detecting pin breaching in an evacuated test section was demonstrated by heating an argon-pressurized capsule having a fusible seal and a simulated defect. The capsule had an 0.8-mm-diameter, drilled hole that was soldered closed with Ag-Cu-Sn-Zn soldering material that melts at 618°C and flows at 652°C. The length of the capsule was such that the contained argon gas pressure would approximate that of fission gas in an irradiated IFR fuel pin when the capsule was at temperature. The distance between the defect in the capsule and the pressure transducers at the top of the test section was 100 cm, roughly the same as that anticipated for the breach of a real fuel pin during a test.

The pressure responses of the two transducers in the pressurized capsule test was qualitatively similar. The pressure inside the evacuated test section

remained low (<1 kPa) during slow heatup (1°C/sec) from 300°C, indicating that the test section was sealed tightly during the temperature rise. The pressure increased abruptly at 345 sec when the control-thermocouple temperature reached 619°C, one degree above the solidus of the Ag soldering material. This pressure rise caused a furnace scram at a trip pressure of 8.2 kPa less than 2 sec after melting of the solder. Considering the distance (100 cm) between the defect and the pressure transducers, the sensitivity and response time of the system were excellent in detecting pin breach in an evacuated test section. Lowering the trip setpoint of the pressure transducers further reduces the time between pin breach and detection.

The argon gas released in the sensitivity test was collected to establish the accuracy of the gas-measurement system. The volume of gas collected was within 0.4% of the calculated, contained volume before the test thus demonstrating the capability of the system to quantitatively measure released fission gases.

Irradiated Fuel Test Performance

During FY-1990, three run-to-cladding breach tests (FM-1, -2, and -3) were conducted in the WPF system on irradiated fuel pins at the same test temperature (820°C). The performance of the WPF system in these tests was excellent in terms of temperature control, pin breach detection, and fission gas collection and measurement. Test FM-1 was performed on a 2.9 at.% burnup, U-10Zr/HT9-clad fuel pin that breached at 67 min into the constant temperature hold period at 820°C. The time to failure of this fuel pin fell within the range of the FPIN-2/LIFE-METAL pretest predictions (30 to 90 min). Test FM-2 was performed on a 2.9 at.% burnup, U-19Pu-10Zr/HT9 fuel pin. The time to failure of this pin was longer (112 min) than that of the FM-1 pin, but still within the expected deviation of the HT9 cladding creep rupture correlation. Both pins breached in the fuel column region and the breaches were attributed to fission-gas pressure loading coupled with cladding wall thinning due to fuel-cladding eutectic penetration. Test FM-3 was performed on a U-26Pu-10Zr/HT9 fuel pin with a larger plenum and lower burnup (2.2 at.%) than those of the FM-1 and FM-2 test pins. The lower fission gas pressure in the plenum probably accounted for the delayed failure (146 min) of this fuel pin.

Posttest examination of the FM-1, -2 and -3 fuel pins is underway, and includes isotopic gamma scanning of the test section containing the fuel pin and neutron radiography, sectioning of the test section to recover the fuel pin, and optical and quantitative metallographic examination of the cladding breach and adjacent fuel microstructures.

References for Section IV

1. "The Experimental Breeder Reactor-II Inherent Safety Demonstration," Nucl. Eng. Des., 101:1 (1987).

2. R. M. Singer, D. Mohr, and J. Gillette, "Transition from Forced to Natural Convection Flow in an LMFBR under Adverse Thermal Conditions," Proc. Seventh Intl. Heat Transfer Conf., 5:537, Munchen, FRG (1982).

3. M. S. Smith and W. A. Ragland, "Interaction of CREDO with the EBR-II PRA Development," Trans. Am. Nucl. Soc., 60:411, San Francisco, CA (November 26-30, 1989).

4. J. M. Kramer, T. H. Hughes and E. E. Gruber, "Validation of Models for the Analysis of the Transient Behavior of Metallic Fast Reactor Fuel," Trans. of the 10th Intl. Conf. on Structural Mechanics of Reactor Technology, C:65, Anaheim, CA (August 1989).

5. M. C. Billone, Y. Y. Liu, E. E. Gruber, T. H. Hughes and J. M. Kramer, "Status of Fuel Element Modeling Codes for Metallic Fuels," Proc. Intl. Conf. on Reliable Fuels for Liquid Metal Reactors, 5, Tucson, AZ (September 7-11, 1986).

6. H. Tsai, "Fuel/Cladding Compatibility in Irradiated Metallic Fuel Pins at Elevated Temperatures," Proc. of the Intl. Fast Reactor Safety Mtg., 2:257, Snowbird, UT (August 12-16, 1990).

7. T. H. Bauer, G. R. Fenske and J. M. Kramer, "Cladding Failure Margins for Metallic Fuel in the Integral Fast Reactor," Trans. of the 9th Intl. Conf. on Structural Mechanics in Reactor Technology, C:3, Lausanne, Switzerland (August 17-21, 1987).

8. Y. Y. Liu et al., "Whole-pin Furnace System: An Experimental Facility for Studying Irradiated Fuel Pin Behavior Under Potential Reactor Accident Conditions," Proc. of the Intl. Fast Reactor Safety Mtg., 1:491, Snowbird, UT (August 12-16, 1990).

9. T. H. Bauer, A. E. Wright, W. R. Robinson, J. W. Holland and E. A. Rhodes, "Behavior of Modern Metallic Fuel in TREAT Transient Overpower Tests," Nucl. Technol. (in press).

10. C. E. Lahm et al., "EBR-II Driver Fuel Qualification for Loss of Flow and Loss of Heat Sink Transients Without Scram," Nucl. Eng. Des., 101:25 (1987).

11. M. L. Hamilton et al., "Mechanical Behavior of Irradiated Fuel Pin Cladding Evaluated under Transient Heating and Pressure Conditions," Dimensional Stability and Mechanical Behavior of Irradiated Metals and Alloys, BNES, London, 1:211 (1983).

12. H. Tsai, "A Versatile Apparatus for Studying the Behavior of Irradiated Fuel," 37th RSTD Proc., 1989 ANS Winter Mtg., 88, San Francisco, CA (November 26-30, 1989).

V. CORE DESIGN DEVELOPMENT

A. Core Design Characteristics Used for US/European Safety Study

Technical specialists from Germany, France, the United Kingdom and the U.S. joined together for comparative analyses of safety performance of metal and oxide fueled cores for a range of accidents in a large (3500 MWth), pool-type liquid-metal-cooled reactor. The results of these studies are reported in Sect. IV and in Refs. 1 and 2. The designs presented here form the basis on which detailed neutronic performance and passive safety characteristics are calculated and analyzed. Differences in the computed static performance parameters of metal and oxide cores which arise from basic differences in their neutronic characteristics are identified and discussed.

1. Core Design Description

The metal and oxide reactor core designs were developed based on the general reactor specifications summarized in Table V.1 and the constraints of Table V.2. In addition, it was taken as a requirement to develop metal and oxide cores which are interchangeable in the following sense:

- same assembly pitch,
- same control rod locations and number of rods,
- same overall assembly length, and
- same (except for minor adjustments) radially heterogeneous core layout.

The active zone of the reactor is comprised of a radially heterogeneous arrangement of driver and internal blanket assemblies with one row of radial blanket and three rows of removable shield as shown in Figs. V.1 and V.2 for the metal and oxide cores, respectively. The main motivations for using a radially heterogeneous arrangement rather than the homogeneous layout are:

TABLE V.1. General Reactor Specifications

Reactor Power (MWt)	3500
Reactor Outlet Temperature, °F(°C)	950 (510)
Reactor ΔT, °F(°C)	275 (153)
Cycle Length (days)	365
Capacity Factor (%)	80
Fuel Residence Time (cycles)	
Core	3
Internal Blanket	3
Radial Blanket	6

TABLE V.2. General Design Constraints

	Metal	Oxide
Structural Material	HT-9	HT-9
Driver Fluence Limit (10^{22} fast n/cm^2)	35	35
Fuel Material	U-Pu-10Zr	UO_2-PuO_2
Driver Smear Density Limit	75 vol.%	82.5% TD
Pellet Density	15.7 gm/cc	86.8% TD
Burnup Limit (MWd/kg HM)	150	150
Blanket Material (depleted)	U-10Zr	UO_2
Pellet Density	15.7 gm/cc	95.7% TD
Blanket Smear Density Limit	85 vol.%	93.3% TD
Peak Linear Heat Rating, kW/ft(w/m)	15 (317.5)	13.5 (285.8)

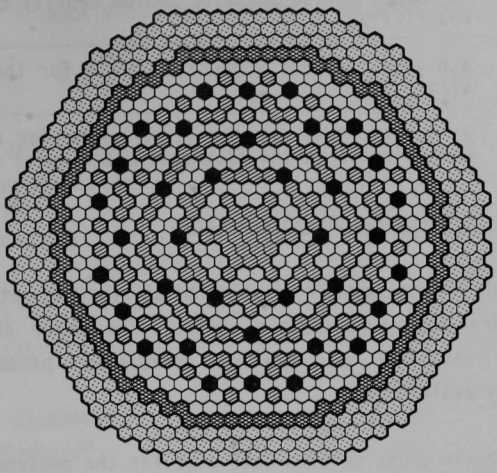

Fig. V.1. Metal Core Planar Layout

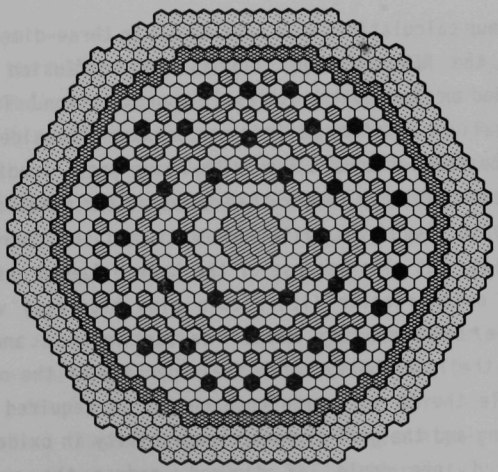

Fig. V.2. Oxide Core Planar Layout

- to obtain a less positive sodium density coefficient of reactivity,
- a higher internal conversion ratio for the given driver pin size, and
- a higher driver enrichment--allowing for a lower fluence to burnup ratio in the fluence-limited metal driver assemblies.

2. Core Performance Characteristics

A neutronics analysis was carried out for the metal and mixed oxide heterogeneous core designs described above. The major objective of these analyses was to establish the relevant performance parameters needed for performing safety evaluations.

The basic cross section data used for the neutronics analyses were from ENDF/B-V.2. These data were processed through the MC^2-2/SDX code system[3,4] to generate separate oxide and metal fuel broad-group libraries which explicitly take account of resonance and spatial self-shielding effects. Nine group cross section sets were generated for general use (in the depletion and rod worth calculations) and 21-group sets were generated for the reactivity coefficient calculations.

Burnup calculations were carried out in three-dimensional hexagonal-z geometry using the REBUS-3 code[5] and a nodal diffusion theory neutronics methodology[6] based on the equilibrium cycle approximation. Table V.3 summarizes several of the salient massflow differences between the oxide and metal cores as calculated by the REBUS-3 code. The oxide heavy metal loading and heavy metal mass flows are substantially larger than those of the metal core mostly because of the presence of the 14 in. axial blankets and the correspondingly taller blanket assemblies, but also because of the taller fueled zone in the core. In particular, the oxide reactor (i.e., core plus blankets) volume is some 70% larger than the corresponding metal reactor volume, and this more than compensates for the lower heavy metal smear density of the oxide vs. the metal fuel form. While the 40 in. oxide core height is required based on pin peak linear heat rating and the goal of interchangeability in oxide/metal layout, and cannot be reduced, one could, if desired, reduce the oxide axial blanket thickness, with corresponding reductions in internal and radial blanket lengths,

TABLE V.3. Reactor Mass Flow Summary

	Metal	Oxide
Enrichment[a] (5)	14.4	19.0
Initial Fissile[a] Loading (kg fissile)	4403.3	4982.7
Initial HM Loading (tonne)	59.50	86.25
Heavy Metal Mass Flow Rate (tonne/y)	18.12	26.32
Breeding Ratio		
Drivers	0.595	0.510
Internal Blankets[b]	0.424	0.446
Radial Blankets[b]	0.106	0.109
Axial Blankets	-	0.157
Total	1.126	1.221
Net Fissile[a] Production (kg/y)	138.6	258.3

[a] Pu^{239} + Pu^{241}.

[b] Over full height; notice difference in heights of metal and driver IB's and RB's.

as a way to reduce the heavy metal reprocessing/refabrication mass throughputs--since the oxide breeding ratio is 10 points higher than that of the metal core. This would have only small effects on safety coefficients, linear heat rate and burnup control swing. Thus, we elect instead to retain the traditional oxide goal of a ~1.2 breeding ratio and separately maintain the traditional IFR goal of a net fissile production which is only just sufficient to overcome estimated reprocessing/refabrication losses.

The oxide enrichment, initial fissile inventory, and fissile loading/year all exceed those of the metal core basically because of the softer neutron spectrum. The harder spectrum of the metal core both increases η and leads to more U^{238} fast fission effect thereby giving a higher worth per gram of fuel and requiring a lower enrichment for BOEC criticality. The higher η and

fast effect plus the increased amount of U^{238} in the core increase the internal conversion ratio of the metal core relative to oxide so that a lower BOEC enrichment is required to assure EOEC criticality.

The sodium void, sodium density, Doppler coefficient, fuel and structure worths and axial and radial expansion coefficients of reactivity were determined in three-dimensional hex-Z geometry for end-of-equilibrium cycle (EOEC) conditions. Flux and adjoint distributions were calculated in 21 energy groups using the DIF3D code,[7] and these data were input to VARI3D to generate the appropriate reactivity worth coefficients. Table V.4 shows the global reactivity coefficients evaluated at EOEC for both the metal and oxide cores.

Examination of Table V.4 shows that the harder spectrum of the metal core leads to a sodium void worth and sodium density coefficient which are about 33% more positive than those of the oxide. The fuel and the Doppler coefficients are somewhat less than half as negative for the same reason. Alternately, the radial and axial expansion coefficients, which are determined mostly by core size and H/D ratio, have similar values for the cores. The impacts of these differences on passive safety response characteristics are discussed in Sect. IV.

3. Conclusions

In this study, we have identified and quantified those physics parameters which differentiate metal and oxide fuel types when the cores are designed to meet the constraints of interchangeability and small burnup reactivity swing. The study shows that although oxide and metal cores designed to the same ground rules may exhibit many similar performance characteristics, they differ substantially in reactivity coefficients, control strategies, and fuel cycle operations. For example, the metal fueled core was shown to require smaller fissile and heavy metal loading and reduced control system requirements. A comprehensive discussion of the neutronics performance of the metal and oxide cores can be found in Ref. 8. However, the more important differences relate to differences in transient and safety performance which derive from differences in reactivity coefficients and thermal conductivity of the fuel forms.

TABLE V.4. Reactivity Feedback Coefficients at EOEC

	Metal		Oxide	
Beta Effective	$3.515 \cdot 10^{-3}$		$3.301 \cdot 10^{-3}$	
Prompt Neutron Lifetime, (s)	$3.195 \cdot 10^{-7}$		$4.054 \cdot 10^{-7}$	
Sodium Void Worth, ($)				
Driver	4.98		3.79	
IB	2.31		1.68	
RB	-0.03		-0.08	
AB	-		-0.19	
Sodium Density Worth, ($)				
Driver	4.51		3.37	
IB	1.99		1.42	
RB	-0.06		-0.11	
AB	-		-0.23	
Doppler Coefficient, $\left(-10^{-3}\, T \frac{dk}{dT}\right)$	Fuel	Structure[a]	Fuel	Structure[a]
Flooded Doppler				
Driver	1.929	0.508	3.984	0.968
IB	1.726	0.174	4.337	0.380
RB	0.181	0.015	0.406	0.030
AB	-	-	0.592	0.065
Voided Doppler				
Driver	1.155	0.378	2.933	0.710
IB	1.180	0.136	3.518	0.293
RB	0.138	0.012	0.340	0.023
AB	-	-	0.506	0.052
Axial Expansion Coefficient, ($/cm)				
Fuel				
Driver	-0.718		-0.693	
IB	0.081		0.137	
RB	-0.004		-0.007	
Fuel and Clad				
Driver	-0.641		-0.617	
IB	0.118		0.170	
RB	-0.007		-0.009	
Fuel and Total Structure				
Driver	-0.586		-0.562	
IB	0.145		0.195	
RB	-0.008		-0.010	
Radial Expansion Coefficient, ($/cm)	-0.765		-0.640	
Control Rod Driverline Expansion Coefficient,[b] ($/cm)	-0.116		-0.0712	

[a]Structure Doppler includes clad plus duct wall.

[b]Value at BOEC = -0.0785 $/cm metal; -0.1183 $/cm oxide.

B. Pin Power and Burnup Modeling in Hex-Z Nodal Diffusion Theory and Validation Against EBR-II Burnup Measurements

Motivated by the analysis needs resulting from the Integral Fast Reactor (IFR) fuel cycle demonstration and other advanced Fast Breeder Reactor (FBR) designs, a method for recovering detailed (pin-wise) information from coarse reactor representations has been developed for hexagonal-z geometry and implemented in a computer code RCT. This code, in conjunction with the REBUS-3 reactor burnup code, has been used to calculate in detail the depletion in EBR-II over a long series of runs. These calculations are being used to validate the REBUS/RCT fuel management methodology as adequate for the EBR-II/FCF fuel cycle for both operational and material control and accountancy purposes. The development of these reconstruction methods was essential to the practical application of the REBUS methodology to the EBR-II fuel cycle.

1. Reconstruction of Pin Burnup Characteristics

Reconstruction methods have reached a high level of development for Light Water Reactors, and are becoming standard analysis tools because they extend the usefulness of computationally efficient nodal schemes and eliminate the need to perform fine-mesh computations. However, the existing reconstruction methods are not directly applicable to full-core FBR's because they have been designed for Cartesian geometry and macroscopic depletion calculations. Therefore, RCT has been developed to reconstruct the intra-nodal distributions of power density, burnup, nuclide densities, group fluxes, and fast and total fluences from nodal-diffusion/depletion calculations performed in hexagonal-z geometry using the REBUS-3/DIF3D Argonne code system.

The spatial reconstruction techniques in RCT are based on higher order polynomial expansions of the nuclide densities as well as the group fluxes. The intra-nodal pointwise group flux is approximated for each node assuming the flux within a node is separable in the hex-plane and axial directions. With this separability assumption, the axial flux distribution of a node is interpolated for each group by a cubic polynomial constrained to preserve the node-average flux, the top and bottom surface-average fluxes, and z-directional flux moment. The hex-plane distribution is interpolated for each group by a non-separable

sixth order polynomial required to preserve the 13 nodal quantities (one node-average flux, six surface-average fluxes, and six surface-average currents) and six local corner fluxes. A unique sixth order polynomial for the hex-plane distribution is obtained with additional constraints requiring the polynomial to be invariant under the symmetry operations of the hexagon and to reproduce lower order polynomial shapes exactly. The corner fluxes used in the hex-plane flux interpolation is approximated by assuming a biquadratic polynomial shape (less the $x^2 y^2$ term) in each of the three adjacent nodes. A simple expression for a corner flux is obtained by preserving node-average and surface-average fluxes, requiring flux and current continuity at mid-points, and imposing a source free condition at a corner point.

The intra-nodal nuclide densities are calculated in one of two ways. In the first way, which is applicable to conventional assemblies with nominally uniform beginning of life (BOL) densities and smooth density variation after depletion, the surface and corner densities are first calculated by solving the nuclide transmutation equations using the surface-average and corner fluxes. Using these surface-average and corner densities as well as the node-average density from the nodal solution and making the assumption of hex-planar and axial separability, the hex-plane densities are interpolated at the center of each fuel pin by a fourth order polynomial. Similar to the case of flux interpolation, the interpolation polynomial is required to preserve the above 13 base values and to be invariant under the symmetry operation of the hexagon. The axial density distribution is interpolated by a quadratic polynomial using the node-average density and the top and bottom surface-average densities. The second method of computing local nuclide densities is applied to specified "special" pins in assemblies with different types of fuel pins (e.g., experimental assemblies in EBR-II); in this case, the densities are not smooth functions of position within the assembly and cannot be determined by interpolation. The special pin nuclide densities are, therefore, calculated by point depletion, i.e., solving the depletion equations with the interpolated fluxes. For each axial pin segment contained in a given node, the top, axial-average, and bottom densities are calculated along the center line of the segment. Using these three values, the axial density distribution is interpolated by a quadratic polynomial.

The intra-nodal distribution of the power density is calculated using the interpolated flux and nuclide density distributions. On the other hand, the intra-nodal burnup and fluence distributions are calculated in a similar manner as the nuclide densities. For conventional assemblies, the hex-plane distributions of burnup and fluences are interpolated by fourth order polynomials, and the respective axial distributions are interpolated by quadratic polynomials, using the node-average, surface-average, and corner values. For the special pins, the burnup and fluences are explicitly calculated using the interpolated fluxes at the center of each fuel pin.

Several important capabilities have been implemented in RCT to permit its application to a wide range of core designs and fuel management strategies. As mentioned above, the burnup characteristics are explicitly calculated for user-defined "special pins" by point depletion using the interpolated fluxes at the center of each fuel pin. The radioactive decay during the out-of-core storage is also considered in the nuclide density calculation. Since non-uniform intra-nodal distributions are considered in reconstruction calculations, the rotational shuffling of assemblies is allowed and is specified by integer multiples of 60°. To permit assembly reconstitution from different types of fuel pins, pin-by-pin shuffling is allowed for the special pins. The axial displacement of fuel (e.g., arising from the movement of the fueled portion of the control rods in EBR-II) is also treated, consistent with the data provided in the REBUS-3 input dataset. Multi-cycle reconstruction calculations are performed as a sequence of single cycle RCT calculations.

2. Validation Using EBR-II Burnup Measurements

One of the first steps undertaken to demonstrate the technical feasibility of the IFR concept was to irradiate three lead subassemblies of U-Pu-Zr fuel in EBR-II. In February 1985 three 61-element subassemblies (X419, X420 and X421) began operation in EBR-II with D9-clad U-10Zr, U-8Pu-10Zr, and U-19Pu-10Zr fuel. Interim examination and reconstitution and subsequent chemical analysis of elements from these three subassemblies has provided measured burnup data for testing the REBUS/RCT methodology. Experimental burnup data was also obtained from test assembly X425, which contained lead HT9-clad IFR binary and ternary fuel elements.

In order to analyze the burnup history for these subassemblies with REBUS, detailed modeling of the reactor loading and the reactor power level history began with Run 130A (August 3, 1984). This process was then extended through a series of all subsequent EBR-II runs (up to the present), where input to the REBUS burnup calculations utilized the known heavy metal loadings for freshly-loaded subassemblies and the REBUS-calculated number densities for the remainder of the assemblies. Therefore, after a series of EBR-II runs had been analyzed, the effect of the initial conditions (i.e., coarse initial reactor loading data) should have diminished.

Because each of the lead test subassemblies were mixed fuel types, analysis with RCT was required for each EBR-II run in which these subassemblies were irradiated in order to determine local values (i.e., values for a specific element at a specific axial position) of the burnup and nuclide densities. These values were then compared with burnup measurements (based on ^{139}La and ^{148}Nd indicators) and Pu and U isotopic ratio measurements.

Results of the burnup comparisons are given in Table V.5. There are data for 14 samples--each measured with La and Nd burnup monitors. Agreement between the REBUS/RCT calculations and results of chemical analysis for the IFR fuel is generally quite good (i.e., within the combined experimental uncertainties of ~6%). The mean value ± 1σ spread of all 28 C/E values is 1.029 ± 0.032. The ± 1σ value is not the 1σ uncertainty in the C/E values (though related to it). It is simply a measure of the spread or dispersion in the values. The range of the 28 C/E values is from 0.960 to 1.087, these extreme values being La burnup measurements of two samples of the same U-8Pu-10Zr ternary element in X419 at ~1.9% burnup. The mean and 1σ spread in the C/E values according to fuel type are shown below.

	Burnup C/E's Mean Value ± 1σ
U-10Zr	1.024 ± 0.012
U-8Pu-10Zr	1.027 ± 0.038
U-19Pu-10Zr	1.036 ± 0.033

TABLE V.5. Comparison of REBUS/RCT Calculated Burnup (atom %) with ^{139}La and ^{148}Nd Burnup Measurements

Distance from End of Fuel (inches)	Measured Burnup (atom-percent) ^{139}La	^{148}Nd	REBUS/RCT Calculation (atom-percent)	Calc/Exper Rel. to ^{139}La	^{148}Nd
S/A: **X419**					
Element: **T167 (U-19Pu-Zr)**					
1.25 - 1.50	1.571	1.624	1.69722	1.080	1.045
6.00 - 6.25	1.828	1.834	1.96534	1.075	1.072
12.25 -12.50	1.426	1.486	1.49521	1.049	1.006
Element: **T013 (U-8Pu-Zr)**					
1.25 - 1.50	1.628	1.665	1.69471	1.041	1.018
6.00 - 6.25	1.791	1.831	1.94689	1.087	1.063
12.25 -12.50	1.550	1.544	1.48817	0.960	0.964
Element: **T119 (U-10Zr)**					
1.25 - 1.50	1.645	1.615	1.67817	1.020	1.039
6.00 - 6.25	1.848	1.872	1.92038	1.039	1.026
12.25 -12.50	1.454	1.467	1.47511	1.015	1.006
S/A: **X419B**					
Element: **T112 (U-19Pu-Zr)**					
5.50 - 5.75	12.53	12.17	12.3459	0.985	1.014
Element: **T141 (U-10Zr)**					
5.50 - 5.75	11.65	12.14	12.0857	1.037	0.996
S/A: **X420**					
Element: **T096 (U-8Pu-Zr)**					
6.00 - 6.25	5.339	5.679	5.60506	1.050	0.987
S/A: **X425**					
Element: **T456 (U-8Pu-Zr)**					
6.25 - 6.50	10.69	10.71	10.9600	1.025	1.023
6.50 - 6.75	10.47	10.34	10.9419	1.045	1.058

The slight differences in the mean C/E values according to fuel type are not significant. In fact, there are no significant trends in the C/E biases. The set of six C/E values for the binary element in X419 at ~1.8% burnup are the best and most consistent set (i.e., closest to unity and to each other). However, the best C/E's for a single sample were for the U-19Pu-10Zr ternary element in X419B at ~12% burnup, which was the highest burnup measured.

U and Pu isotopic analyses have also been performed by the Analytical Laboratory on the same four IFR test assemblies discussed above. The determinations are again obtained from mass spectrometer measurements. Again, the comparison of the measured and calculated U and Pu isotopic fractions agree quite well.

In summary, the goal has been to validate the REBUS fuel management methodology as adequate to determine isotopic mass and neutronic data inputs to HFEF-S for both operational and material control and accountancy purposes. This required first developing and benchmarking the reconstruction capabilities of RCT and then validating REBUS/RCT as a system which can compute the burnup and isotopic distribution in binary and ternary fuel assemblies. The following conclusions may be made from this study. The principal conclusions from the present study are:

1. REBUS-3 analysis using nodal diffusion theory with a three-dimensional hexagonal-Z full core model and ENDF/B-V.2 nuclear data can adequately follow EBR-II fuel management and depletion.

2. Details of nuclide density, burnup, power density, and fluence within the node or hexagonal subassembly can adequately be reconstructed using the RCT code.

3. Comparisons have been made of REBUS-3/RCT analyses with experimental values, including the analysis of mixed fuel type test assemblies that have had complex irradiation histories (such as multiple reconstitutions, multiple core insertions/removals, and multiple core locations and subassembly orientation).

4. Results of these comparisons for burnup and U and Pu isotopic fractions are quite good (i.e., generally within experimental uncertainties).

The principal recommendations from this study are:

1. At present, the experimental database is rather limited and should be expanded. (In fact, considerably more experimental determinations have been requested and should soon be available.) For the near term, emphasis should be placed on: (i) measurements in ternary elements, (ii) measurements of axial distributions and (iii) measurements in fuel assemblies with Mk-V isotopics and test assemblies with significant "minor actinide" constituents.

2. As the experimental database matures and more data becomes available (and as the new mass spectrometer begins operation), accuracy of the experimental values should be quantified through the study of measurement reproducibility.

3. Refinements in the calculational methods (e.g., use of equivalence theory, improvements in cell-homogenization, or revised nuclear data) should be incorporated as they become available.

4. Input preparation for both the REBUS-3 and RCT calculations should incorporate more automation and verification. All the fundamental input to these codes, in particular, the masses and positions of elements within subassemblies and the location and orientation of all subassemblies both in and out of the reactor, should be stored in electronic form.

5. REBUS-3/RCT analysis, combined with the experimental data from recommendation 1 above, should be used to study/refine the extrapolation of "sample" quantities (i.e., isotopic masses for an axial segment of an irradiated element) to "integrated" quantities (i.e., isotopic masses for a collection of elements).

C. Modeling the Isotopic Mass Flows in the Electrorefiner

A new computational code package called PYRO has been developed to support the IFR fuel recycle demonstration project at the Fuel Cycle Facility in ANL-W. The basic pyrochemical code PYRO1-1 developed by Ackerman[9] models the atomic mass flows and phase compositions of 48 essential chemical elements involved in the pyroprocess. It has been extended to PYRO1-2 by linking with the modified ORIGEN code[10] to track more than 1000 isotopic species, their radioactive decays, and related phenomena.[11,12] The algorithm and basic code structure for isotopic mass tracking in the pyroprocess will be presented first. Results from simple scoping studies to more realistic simulation runs will then be discussed to illustrate the significance of modeling in-process radioactive decays, i.e., the "aging" related phenomena.

The dissolution of the spent fuel into the electrorefiner solutions and the extraction of U or U-Pu mixtures by electrotransport to a solid or liquid Cd cathode are basically partition of elements between a molten salt and solid or liquid metal phases. It involves the redox exchange reactions between one element in metal phase and another element in salt phase. At the process temperature of 500°C, these exchange reactions proceed very rapidly so that their chemical equilibrium is established quickly. Therefore, concentrations of the metals and their chlorides can be determined from their equilibrium constants and the relations between chemical activities and concentrations of those species involved. Based upon the chemical equilibria of the redox exchange reactions for elements in various phases in the electrorefiner, models for various chemical processes, such as dissolution, oxidization, electrotransport, reduction, etc. have been developed and implemented as PYRO1-1 modules by Ackerman. Since PYRO must remain flexible to keep up with the pace of pyroprocess technology development, relatively simple procedures are also included in the code package to simulate non-chemical phenomena, such as distillation, melting, or mechanical split and combine operations.

In order to track mass flows by isotopes in the pyroprocess, the code must not only follow the chemical partition in space, but must also allow decay of radioactive nuclides in time. Theoretically, these two events can occur simultaneously; in reality, with spent fuel cooled for 100 days or more, most of

the short-lived nuclides would have decayed away by the time the fuel is introduced into the electrorefiner. In general, chemical partition in pyroprocess takes place in a relatively short time (hours or days) compared to the half-lives (months or years) of those radioactive species that have survived thus far. Under such a circumstance, chemical partition and radioactive decay can be modeled independently. Furthermore, it is assumed that all isotopes of a given chemical element will participate with equal opportunity in all chemical reactions involving that element. For example, U-235 and U-238 are treated equally with all other uranium isotopes for all chemical reactions involved in the whole pyroprocess. But their distinct nuclear properties will be maintained outside the chemical calculations.

These two fundamental assumptions are the guiding force in developing the new capability and the structure of this code is divided into two major blocks: one block performs the chemical partition based on chemical elements only, and the other block performs the radioactive decays using a modified version of the ORIGEN code package and related calculations based on nuclear isotopics. Each code block is a conglomerate of various computational modules that will do specific chemical or physical calculations when requested. This code is developed under the VAX/VMS environment and its computational modules are either Pascal procedures or FORTRAN subroutines. A driver program is constructed according to the flowsheet of the pyroprocess that the user intends to investigate. Proper order of calling various modules and synchronization of input/output must be maintained in order to produce meaningful results. Communications between these two major code blocks are established through internal interface files. Nuclear data libraries and various I/O files are defined by the user. Process control parameters and several code options can be selected by the user.

Resource requirements and job costs for typical test runs using various code options are modest. Generally speaking, one needs to have ~2 megabytes of core memory and ~12,000 blocks of disk space for output for a full simulation of processing 24 batches of feeds and uses all options for isotopics, aging, photon spectra, and summary tables. The CPU time in such case would be ~20 min. This is ~20 times more compared to the requirement for the basic PYRO1-1 run without the isotopic mass tracking capability.

To demonstrate this new capability, especially that related to nuclear isotopics, several scoping studies based on a simplified process flowsheet were performed and analyzed. The flowsheet for these scoping studies assumed that only U-10Zr binary driver spent fuel from EBR-II will be processed using anodic dissolution and solid electrodes for deposition. In the scoping studies, a total of 24 batches of binary fuel with ~20 kg of heavy metal per batch is processed at a rate of one batch per 30 days. Such a long turnaround time allows all steps in the pyroprocess to be completed. The actual time needed for the electrorefining step alone is only a day or so. Neither cadmium pool nor electrolyte salt will be cleaned up between batches in these scoping studies.

Due to the chemical partition and "aging" of the elements in the electrorefiner, materials in the pool and the salt will have different characteristics. The effect of radioactive decays can be seen from the total heat loads in the electrorefiner as shown in Fig. V.3. Without considering the decay, the heat load would simply accumulate linearly as each batch added a fixed amount

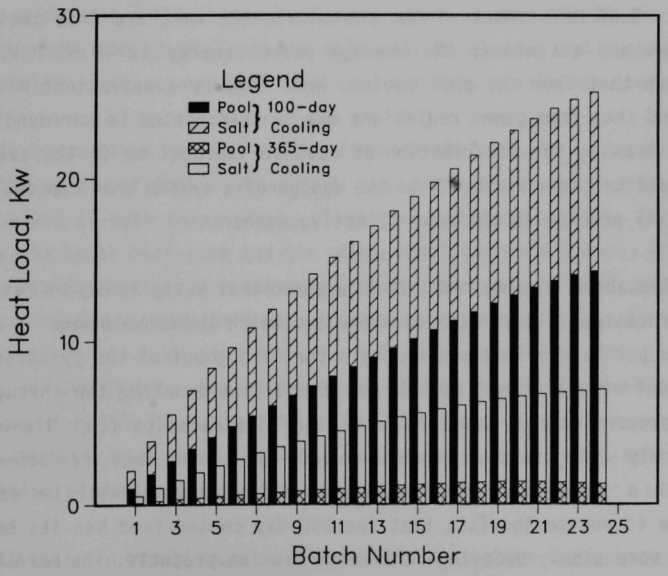

Fig. V.3. Calculated Heat Loads to the Electrorefiner Using EBR-II Binary Driver Spent Fuel after 100-day Cooling and 365-day Cooling as Feed

of heat to the electrorefiner. When aging is considered, the cumulative heat load to the system increases at a retarded rate due to the decay of the material added in previous batches. As shown in Fig. V.3, the total heat load to the electrorefiner approaches an asymptotic value of ~27 kW after processing ~40 batches of 100-day cooled binary feed. Similarly for binary feed at 365-day cooling, the electrorefiner heat load reaches an asymptotic value of ~7 kW after processing ~24 batches.

As also shown in Fig. V.3 for the 100-day cooled feed, heat from the pool and that from the salt is roughly equal in early batches, and approaches 55% in pool and 45% in salt at the end of 24 batches. But for 365-day cooled feed, almost 90% of the heat is in the salt and only ~10% is in the pool after 24 batches are processed. It was also found that the heat in the pool for 100-day cooled feed consisted of ~90% gamma and ~10% beta. On the contrary, the heat in the salt consisted of ~90% beta and ~10% gamma. Similar trends were also observed when the 365-day cooled feeds were processed. Most of the photons in the pool are from the gamma decays of the noble metal fission products; the average photon energy is ~0.63 MeV. Most of the photons in the salt are from the decays of lanthanides and actinides; the average photon energy is ~0.53 MeV, somewhat softer than that from the pool region. Heat from beta radiations will deposit locally and that from gamma radiations may be transported to surrounding media. Therefore knowing the distribution of heat in the pool or in the salt and its form as beta or gamma is useful to the design of a system that can deal with the heat removal problem in the most effective manner.

In the above scoping runs, it is assumed that every 30 days a batch of feed will be processed. A case was run where the batch turnaround time is cut by 50% to 15 days per batch. This would double the throughput of the pyroprocess for a given amount of operating time. It was found that doubling the throughput will not add proportionately more heat to the electrorefiner; at the end of 24 batches, only ~25% more heat is added for 100-day cooled feed. For 365-day cooled fuel, such a simulation indicated that ~33% more heat will be added. This difference is due to the fact that the 365-day cooled feed has its heat mainly come from more slowly decaying rare earth fission products. The more "aged" the feed is, the more "stubborn" it becomes in terms of radioactive decays; thus less beneficial rate of return on reducing the relative heat load will be gained by

waiting longer. But of course the cooler the feed is, the smaller the net heat load to the electrorefiner will be.

The new isotopic mass tracking capability is also used to simulate a pyroprocess campaign strategy proposed by Ackerman and Rohde for the FCF demonstration project.[13] In that strategy, there are two campaigns to be conducted; and the batch turnaround time is assumed to be 30 days. The first 12 batches are binary campaign where only binary fuels will be processed using anodic dissolution and solid electrodes for uranium depositions. After the sixth batch, insoluble noble metal fission products will be removed. At the end of the binary campaign, both Cd pool and salt will be cleaned and restored for the second campaign where mixed binary and ternary fuel will be processed. In the mixed fuel campaign, the electrorefiner will first be charged with binary feeds, then a batch of 20 kg plutonium feed will be loaded to alter the Pu/U ratio in the salt to ~2 to 1 so that the system is prepared to deposit plutonium using liquid Cd cathode. Once the salt reaches such a condition, an alternate of binary and ternary feed will be processed. In the middle of the second campaign, insoluble noble metal fission products will again be removed. At the end of the 24th batch, both the Cd pool and the salt will be cleaned and restored by some waste campaign processes not yet finalized for this simulation study.

Heat accumulates in the electrorefiner as the campaign proceeds and is cut back at the middle of both campaigns by removing noble metal fission products, and at the end of both campaigns by cleaning up the pool and the salt. Figure V.4 shows the total heat load and its gamma component when 100-day cooled feeds are used. Maximum heat load reaches ~13 kW near the ends of both campaigns. For 365-day cooled feeds, similar trends were observed except that: 1) the maximum heat load is only ~5 kW near the ends of both campaigns; and 2) the gamma component is ~10% of total heat load versus ~40% in the 100-day cooled case. Most of the heat for 365-day cooled feeds is beta energy from rare earth fission products in salt; whereas for 100-day cooled feeds both noble metal and rare earth fission products contribute comparable amounts.

With this new capability, we are now able to perform isotopic mass tracking through the pyroprocesses to be demonstrated at the FCF. Heating rates, radiation levels, photon spectra, isotopic distributions, fissile enrichments, and many

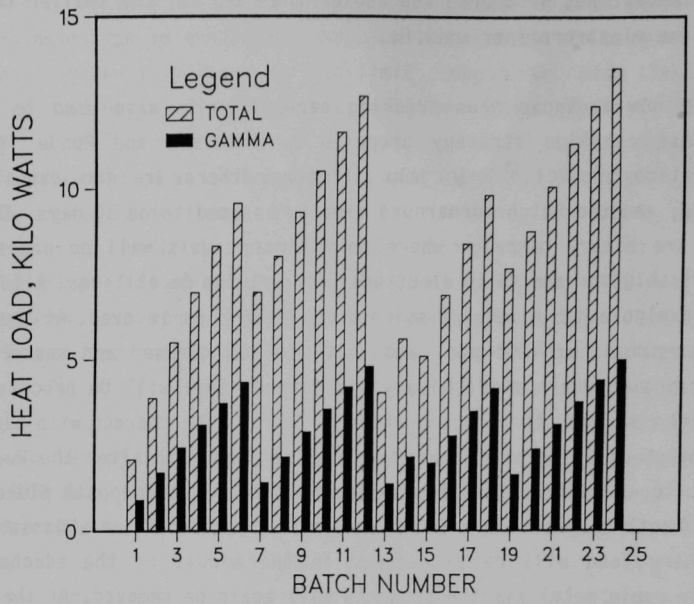

Fig. V.4. HFEF/S Heat Load Study

other important parameters can be calculated consistently to support the design and development needs of the FCF demonstration project. Updates and revisions will be made as new processes are being developed, and as operating data become available. Based on the experience gained in developing this new capability and the results obtained from these scoping and simulation studies, the following summary notes can be made:

1. The fundamental assumption of separability of chemical partition and radioactive decays is generally valid for sufficiently cooled fuels in the pyroprocess. The new capability is structured such that computational modules for chemical processes are independent of "aging" due to nuclear decays.

2. The major effect of "aging" is mostly manifested in the heat load resident in the electrorefiner. With the "aging" effect properly accounted for in the scoping study, heat load estimate is cut down

by as much as 50% (from 50 kW to 25 kW) for the EBR-II Mk-III binary feed of 100-day cooling after 24 batches of operation at a rate of 1 batch per month. Similarly a reduction of ~40% (from 13 kW to 7 kW) is achieved if the same feeds were cooled for 365 days.

3. Doubling the duty cycle of the pyroprocess by increasing the rate to 2 batches per month will not add a substantial amount of heat load to the electrorefiner. The scoping study showed that an increase of ~25% (from 25 kW to 30 kW) in heat load to the electrorefiner after 24 batches of 100-day cooled binary feeds are processed; and an increase of ~33% (from 7 kW to 10 kW) in heat load resulted if 365-day cooled feeds were used instead.

4. About 90% of the heat in the Cd pool is gamma radiation from the noble metal fission products; on the contrary, about 90% of the heat in the salt is beta radiation from the rare earth fission products. It is also found that the noble metal fission products generally have shorter half-lives than that for the rare earth fission products; thus gamma heat in the pool decays more rapidly than the beta heat in the salt which tends to be more "stubborn" and lasts longer.

5. The pyrochemical process intrinsically provides an adequate but not complete separation of Pu from rare earth elements, and no separation from higher actinides. Such a separation is desirable because the retained material discourages diversion, and the higher actinides recycled back to the reactor can be burned as fuel rather than constituting a long-term health hazard in the waste.

This new capability is currently being integrated into a comprehensive mass tracking software package to aid the operation, control, and accountancy of the FCF project. It has the potential to be developed into an out-of-reactor fuel cycle model that can be coupled with the in-core burnup model to simulate consistently and dynamically a completely closed IFR fuel cycle.

References for Section V

1. J. E. Cahalan et al., "Performance of Metal and Oxide Fuels during Accidents in a Large Liquid Metal Cooled Reactor," Proc. Intl. Fast Reactor Safety Mtg., **IV**:73, Snowbird, UT (August 12-16, 1990).

2. P. Royl et al., "Influence of Metal and Oxide Fuel Behavior in the ULOF Accident in the LSPB Benchmark Core and Comparison with Other Cores," Proc. Intl. Fast Reactor Safety Mtg., **IV**:88, Snowbird, UT (August 12-16, 1990).

3. H. Henryson II, B. J. Toppel, and C. G. Stenberg, "MC^2-2: A Code to Calculate Fast Neutron Spectra and Multigroup Cross Sections," Argonne National Laboratory Report, ANL-81-44 (1976).

4. W. M. Stacey, Jr. et al., "A New Space-Dependent Fast-Neutron Multigroup Cross-Section Preparation Capability," Trans. Am. Nucl. Soc., **15**:292 (1972).

5. B. J. Toppel, "A User's Guide to the REBUS-3 Fuel Cycle Analysis Capability," Argonne National Laboratory Report, ANL-83-2 (1983).

6. R. D. Lawrence, "The DIF3D Nodal Neutronics Option for Two- and Three-Dimensional Diffusion Theory Calculations in Hexagonal Geometry," Argonne National Laboratory Report, ANL-83-1 (1983).

7. K. L. Derstine, "DIF3D: A Code to Solve One-, Two-, and Three-Dimensional Finite-Difference Diffusion Theory Problems," Argonne National Laboratory Report, ANL-82-64 (1984).

8. E. K. Fujita and D. C. Wade, "The Neutronic and Fuel Cycle Performance of Interchangeable 3500 MWth Metal and Oxide Fueled LMRs," Proc. Intl. Conf. on the Physics of Reactors: Operation, Design and Computation, **I**:II-55, Marseille, France (April 23-27, 1990).

9. J. P. Ackerman, "PYRO, A System for Modeling Fuel Reprocessing," Trans. Am. Nucl. Soc., 60:168, San Francisco, CA (November 26-30, 1989).

10. M. J. Bell, "ORIGEN - The ORNL Isotope Generation and Depletion Code," Oak Ridge National Laboratory Report, ORNL-4628 (May 1973).

11. J. R. Liaw and J. P. Ackerman, "New Capability for Isotopic Mass Tracking in Pyroprocess Simulation," Trans. Am. Nucl. Soc., 60:169, San Francisco, CA (November 26-30, 1989).

12. J. R. Liaw and J. P. Ackerman, "PYRO- New Capability for Isotopic Mass Tracking in Pyroprocess Simulation," Proc. Intl. Conf. on the Physics of Reactors: Operation, Design and Computation, 2:XI-33, Marseille, France, (April 23-27, 1990).

13. J. P. Ackerman, Argonne National Laboratory, personal communication, (1989).

VI. FUEL CYCLE DEMONSTRATION

A. Introduction

From the outset of the IFR Program, an important goal has been to provide the Facility and equipment for a low-cost demonstration of the pyroprocess fuel cycle at a scale which could easily be related to a future commercial operation. Currently, meeting this goal and beginning the fuel cycle demonstration is the highest priority IFR task. The scope of the effort necessary was described in the "Integral Fast Reactor Program Summary Progress Report FY 1985-FY 1989," ANL-IFR-125, January 1990. Progress toward that end is reported herein.

In the previous report, it was indicated that modifications and equipment installation would be complete by October 1990 and that operation would begin in early 1991. Although progress has been good, resource limitations have resulted in a recognized delay of at least one year in the start of operations with irradiated fuel.

An additional part of the overall Fuel Cycle Demonstration Program is development of a conceptual design for a commercial fuel cycle facility that would utilize the pyroprocess technology developed and demonstrated in the IFR Fuel Cycle Demonstration. This task remains an important issue. However, because of limited personnel and the fact that significant refinement of the concept described in the 1989 report requires information that is to be gained through the demonstration work, no significant resources were allocated directly to this task in 1990 and no progress is reported.

B. Status of Facility Modifications

In May, the National Environmental Protection Act (NEPA) requirements were completed with the approval of the Environmental Assessment and issuance (by DOE) of Finding Of No Significant Impact. DOE-CH then authorized the project to proceed on all previously restricted construction activities. The State of Idaho was notified that full construction began on May 21, 1990 as required in the Idaho Air Quality Construction Permit.

In January, rebar was placed for the Safety Exhaust System (SES) pit ceiling, forms were installed, and the concrete was placed. This includes concrete for the new support beams. Grouting of the pit walls continued into February, and voids in SES pit concrete placing were repaired. The majority of the work on the SES pit was completed in April when the ceilings and walls of pit were grouted with polymer grout, ground smooth, and painted. The final design review of the mechanical systems for the SES was held in December. Procurement was also started for long lead time items for the SES.

The final design review for the foundation of the Safety Equipment Building was held in January. In April, construction of the foundation started. Figure VI.1 shows work on the interconnecting tunnel between FCF and the new Safety Equipment Building. Work on the foundation is shown in Fig. VI.2. In July, the final design review for the building was held. In November, the contract for the building envelope was awarded, and work was to be completed within 120 days. Construction efforts in December are shown in Fig. VI.3. The Emergency Diesel Generators, one of the items to be placed in the Safety Equipment Building, were ordered from National Technical Systems in April, and are scheduled for delivery in March 1991. The day tanks (fuel storage) for the diesel generators are scheduled for delivery in August 1991. The Emergency Diesel Generator System will meet Class IE Safety Grade standards.

In January, a final design review was held for the basement decontamination spray chamber. The basement of the FCF during excavation for construction of the hot repair facility (which includes the Decon Spray Chamber and the Suited Entry Repair Area) is shown in Fig. VI.4. The left hand side of this photo is the approximate location of the spray chamber. Progress in the construction is shown in Fig. VI.5, showing much of the concrete for the lower pit regions. The spray chamber liner was ordered from Process Equipment Co. in February. The installation of the structural steel for the liner started in June and was completed in July. The installation of the liner started and was approximately 50% complete by the end of December. The spray chamber is shown in Fig. VI.6. In addition, the pneumatic transfer system has been installed from the spray chamber to the radiation lab for counting smears.

Fig. VI.1. HFEF/S Modification Program Tunnel Excavation

Fig. VI.2. Work on Foundation for Safety Equipment Building

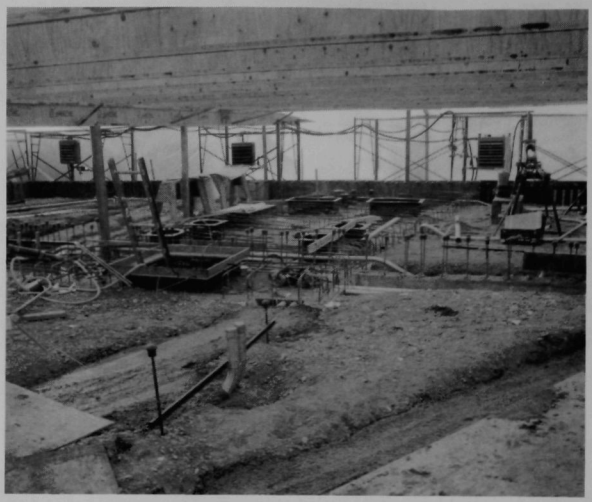

Fig. VI.3. Status of Construction for Safety Equipment Building, December 1990

Fig. VI.4. Preliminary Excavation for Hot Repair Facility

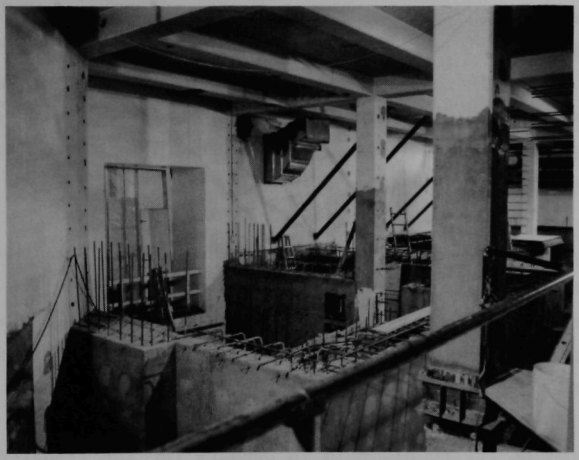

Fig. VI.5. Preliminary Construction for Hot Repair Facility

Fig. VI.6. Installation of Liner for Spray Chamber, December 1990

A variety of work was conducted over the year in the new hot repair facility. Work early in the year included removing some contaminated ductwork from the Suited Entry Repair Area (SERA) and painting the new concrete. A crane was also evaluated and purchased for the SERA. Figure VI.7 shows the crane after installation in October. The SERA bagout system underwent a conceptual design review. In December, orders were placed for the SERA glovewall windows which will be located in the openings shown in Fig. VI.8.

In March, installation of seismic restraints for the hot side of the cell windows started. These modifications were completed in April. In June, work on the new penetrations for cell master slave manipulators in the argon cell started, and they were completed in July. The seismic restraints for the central observation windows were also installed.

A final design review was held in January for the transfer tunnel cart system that will remotely transfer equipment between the cells and the hot repair facility. After preparation of the procurement specifications and solicitation of bids, an order was placed for the transfer tunnel carts in October. The order for the transfer tunnel hydraulic rams was placed in November. An alternate approach for the support of the large lock platen was used to eliminate the need for a safety class hydraulic ram. The movable hatch shield, located under the hatch between air cell and transfer tunnel, was about 30% installed at the end of the year.

The final design review was held for the normal power system in March. By September, work had been completed on the Installation Test Instruction (ITI) for the building feeder changeover. In addition, work was completed for the penetrations through the basement wall for the 4-in. feeder conduits. In October, a preliminary review of the lightning protection system was held (part of the normal power system). An ITI was also completed to install an alternate power source to all condensate and sump pumps. The procurement package for the motor control centers (normal power and non-class 1E components) was completed and issued for procurement in November. Also in November, the installation for the new FCF building feeders from the substation was completed.

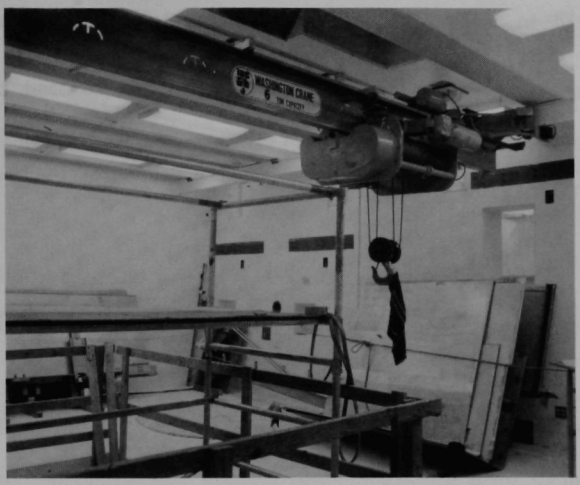

Fig. VI.7. Crane in SERA after Installation

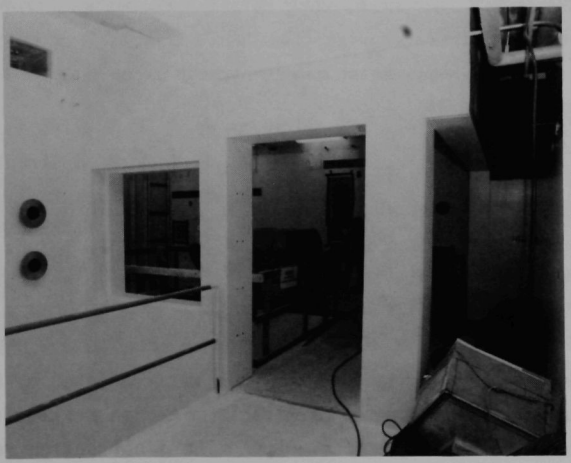

Fig. VI.8. Location of the SERA Glovewall Windows

Phase I and Phase 2 of the final design review for the emergency power system were held in June and November, respectively. The preliminary design review for the facility instrumentation and control was held in August. In September, a preliminary design of the SES sense and command circuitry was completed, and it was reviewed in November.

C. Status of Process Equipment Design and Fabrication

1. Fuel Element Chopper

Fabrication, assembly, prototype testing, and element chopper system improvements were ongoing at ANL-E throughout the year. In August, a system functional test was completed. In September, the fuel element chopper was shipped to Idaho for qualification, and installation. After receipt at ANL-W, the final wiring for the system (radiation resistant wire) started and small modifications were made. Formal qualification will begin in early 1991. The fuel element chopper is shown in Fig. VI.9.

2. Electrorefiner

In addition to the basic research reported in Sect. III Pyro-metallurgical Process Development, work relating to the electrorefiner can be broken down into two main categories: the development of the in-cell apparatus and the operational experience being gained through experiments with the Hot Fuel Dissolution Apparatus (HFDA).

A final design review for the electrorefiner main assembly was held in February. The design review included the primary vessel, support structure assembly, furnace assembly, and associated heater controls. In May, changes to Section 1 of the SDD were submitted. Work on the operations portion of the SDD was also undertaken.

The necessary design and analysis was completed by March for the primary electrorefiner vessel and the contract for design and construction of the primary electrorefiner vessel was awarded. The final design review for the electrorefiner cover and heat shield was held in October.

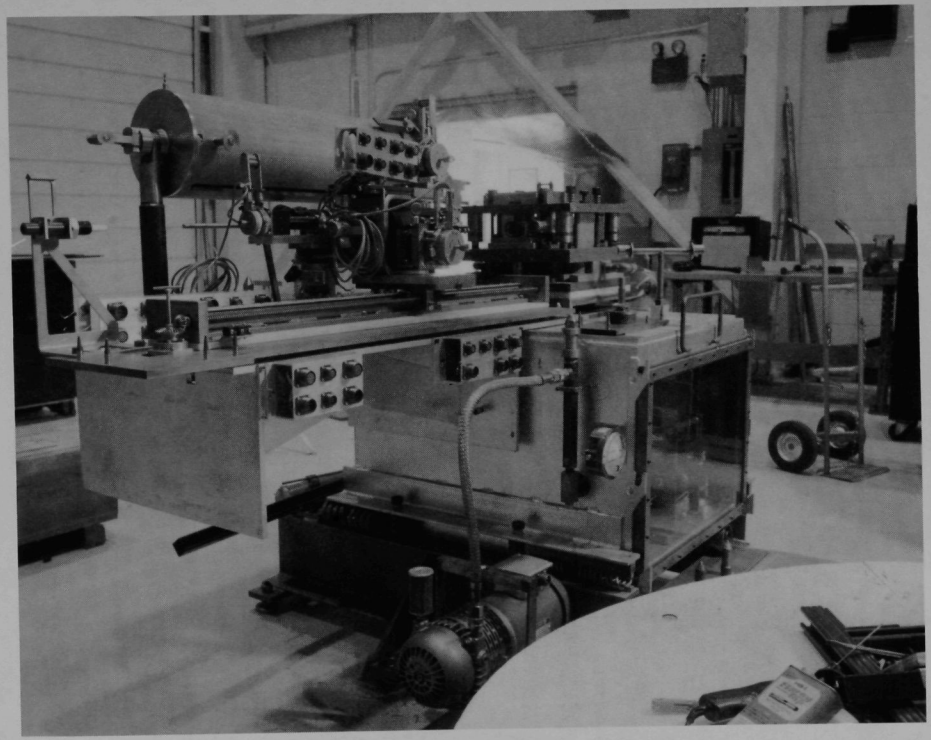

Fig. VI.9. Fuel Element Chopper

Fabrication of the electrorefiner heater modules began in September. The electrorefiner support structure and support ring fabrication were completed and delivered in October (see Fig. VI.10). The primary electrorefiner vessel is scheduled for delivery in February 1991.

The fabrication of the prototype electrode assembly (EA) was completed in September (see Fig. VI.11). In October, all of the major components for the prototype EA, the valve and latch assembly (VLA), and the bracket and latch assembly (BLA) were assembled and test wiring was installed. Mechanical testing of the EA continued through the end of the year.

a. Hot Fuel Dissolution Apparatus (HFDA)

The second thrust for the development of the electrorefiner is the Hot Fuel Dissolution Apparatus (HFDA). The purpose of the HFDA is to help train operators and provide a small-scale data base for irradiated fuel operations.

Although the mechanical items will not be prototypical of the large scale operations, the HFDA should be chemically similar to a larger electrorefiner. The salt and cadmium levels are similar and the mass is scaled down by a factor of 600 from the FCF electrorefiner. Multiple segments (up to 24 g total) of irradiated fuel can be anodically dissolved and deposits 1-1/2-in. long by 1-in. in diameter can be made.

Fabrication and qualification of the new HFDA assemblies and electromechanical equipment was completed in late October 1990. The equipment was placed in HFEF so in-cell testing could begin. Initial operations were outlined in a detailed test plan. The operations were simulated by the PYRO computer code to test the agreement between an actual experiment and the theoretical model. Preliminary testing continued through the end of the year.

Fig. VI.10. Electrorefiner Support Ring

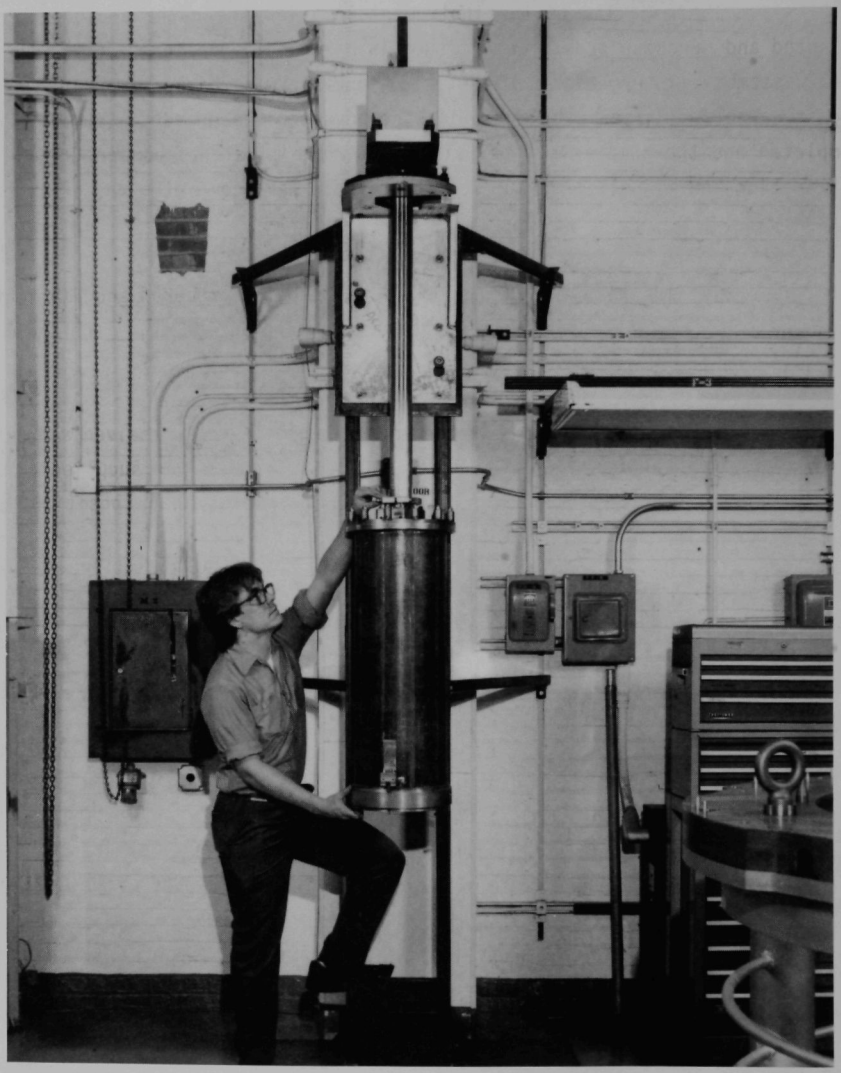

Fig. VI.11. Prototype Electrode Assembly

3. Cathode Processor

The majority of the instrumentation for the cathode processor was selected and purchase orders were issued in March. The designs for the furnace liner assembly, intermediate support ring, and thermal shield were completed in August. The design and fabrication of the advanced design vacuum pump has been completed and the pump should be delivered by the middle of January 1991. The fabrication and inspection plans for the vessels were completed and reviewed by October.

Two identical cathode processors are being procured and fabricated. One of the units will be used for development testing out-of-cell, and the other unit will be for in-cell use.

The power supplies for the induction coils were received and passed the necessary checkout tests. By June 1990, one of the power supplies and the cooling pump, which are needed for development testing, were positioned and installed for later development work.

Design on the crucible assembly was initiated in February 1990. Staged design reviews were conducted throughout the year, with the final design review being completed in December. The crucible hardware was in procurement at the close of the year.

Experience was gained in consolidating the dendritic uranium product in the Cathode Processor Simulation Experiment (CPSE). Experiments have shown that the salt can be efficiently removed by the CPSE process. The batch size of the apparatus was increased to approximately 8 kg. This is 80% of the batch size the FCF cathode processor is designed to handle. Results show that the efficiency of contaminant removal is maintained for the large batch sizes.

4. Injection Casting Furnace

Instrumentation and control schematic drawings, all cabinet wiring drawings, and the wiring specifications for the instrumentation and controls were completed by May 1990. The casting furnace vessel was fabricated and shipped for

inspection and final machining in September. The 30 kW power supply for the injection casting furnace was delivered, tested, and found to be satisfactory.

Qualification testing started in August. The functional checkout of the furnace motors, valves and instrumentation was completed for all in-cell devices. The heatup test plans for the crucible were established in October, all the instruments were calibrated, and the tests started in December. The results to date are satisfactory. The injection casting furnace is shown in Fig. VI.12.

5. Fuel Pin Processor

The final design review process, fabrication, and assembly stages have been completed for the fuel pin processor. The Qualification Plan and SDD have been completed.

Operational demonstrations of the pin processor were conducted to provide information regarding the state of assembling activities and the operational status. Pin processor module fabrication, assembling, alignment, checkout, and software development continued through the end of the year. The fuel pin processor is shown in Fig. VI.13.

6. Vertical Assembler/Disassembler

The Vertical Assembler/Disassembler (VAD) is an existing piece of equipment. The VAD is being modified and improved to meet the goals of the FCF.

Drawings were completed and checked for the VAD Flow Test and Pneumatics Assemblies. Some of the hardware has been purchased for these assemblies. Piping and Installation is expected to begin in February 1991.

The VAD load cell was redesigned to include spring compression in both the tension and compression modes. The hardware has been fabricated, qualified, and will also be installed in February 1991. Bids for the VAD cooling blower assembly were requested and the award of the contract will be made in early 1991. Delivery of the blower assembly is expected in March 1991.

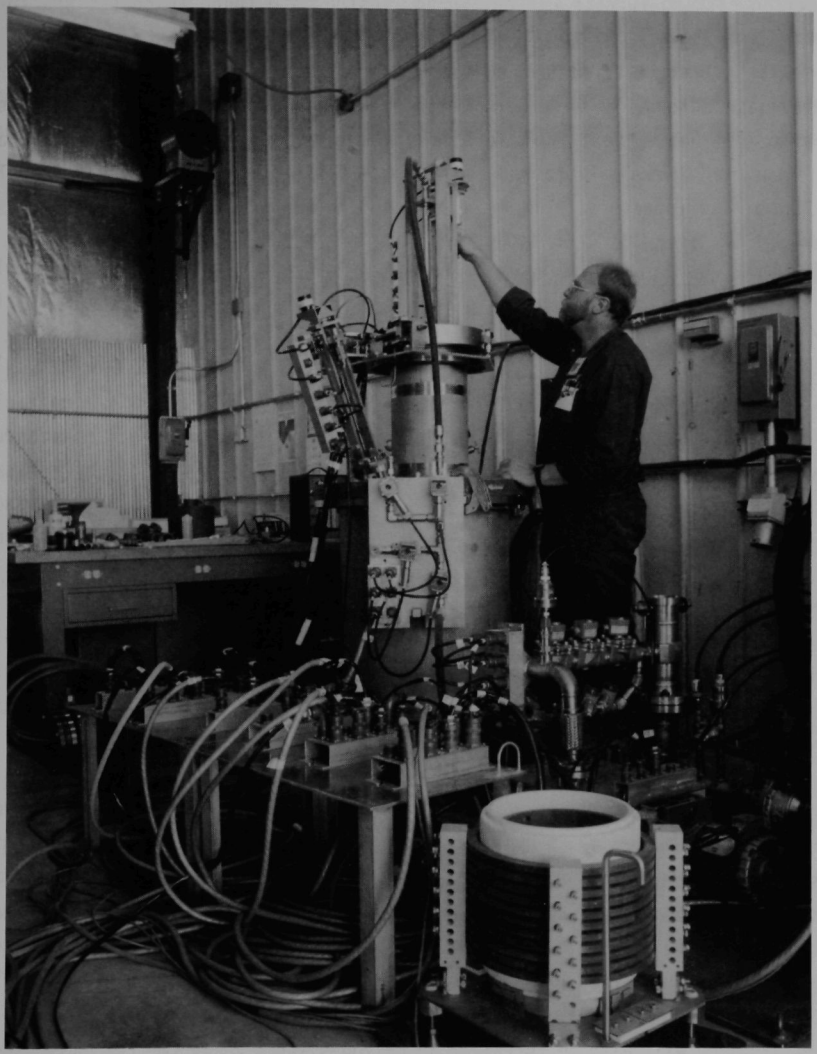

Fig. VI.12. Injection Casting Furnace

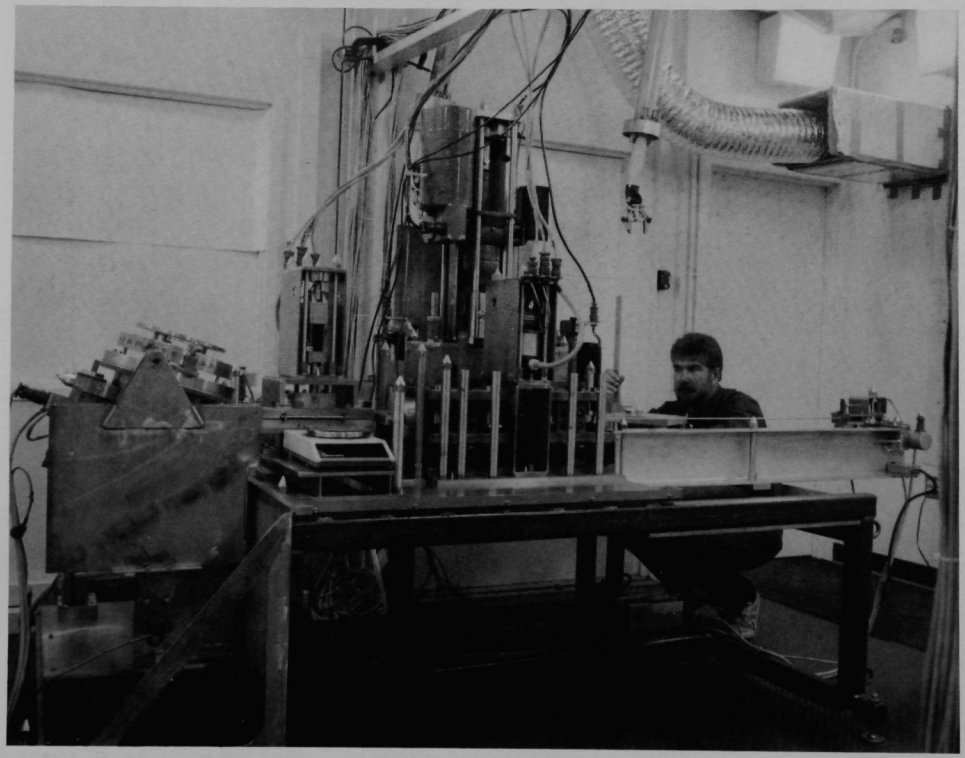

Fig. VI.13. Fuel Pin Processor

D. Waste Handling and Processing

Work has been conducted over the last year to define the process material storage strategy for the IFR project. The work has included identification of the process material streams, thermal modeling of proposed storage schemes, design of the equipment to be used in the argon cell pits, storage strategy definition, and preliminary design of the process material canisters.

The major waste streams include subassembly hardware, element hardware, electrorefiner process materials (salt and cadmium), insolubles, and cathode distillate.

The subassembly hardware is removed at the Vertical Assembler and Disassembler to allow removal of the individual fuel elements from the subassemblies. Once the elements are removed the subassembly hardware is cut into smaller pieces for packing. This process material is packed into shipping containers for transfer to the Radioactive Waste Management Complex (RWMC) at the Idaho National Engineering Laboratory site for interim storage.

The element hardware consists of the structural hardware from the fuel elements (end plugs, cladding hulls, plenums and wire wraps). This will be mixed with broken TRU contaminated hardware to minimize the number of containers to be shipped to RWMC for interim storage.

Electrorefiner process materials consist of salt (lithium chloride and potassium chloride) and cadmium. Typically, the salt and cadmium will be removed from the electrorefiner after most of the uranium and plutonium has been removed. At this time the salt and cadmium are placed into the process material storage canisters. The thermal content of each canister will then be measured to determine the storage options (see the discussion below). Based on the results of the thermal content measurement, the canister will be moved to its storage site.

The electrorefiner insolubles are materials which are not soluble in the electrolyte or cadmium, nor do they oxidize to form a chloride salt which mixes with the electrolyte. This material is removed from the electrorefiner process

materials by passing the salt and cadmium through sintered metal filters. The amount of fission products is assumed to equal the amount of insoluble fission products added to the electrorefiner since the last filtering process. This will be a conservative estimate of the fissile content. Three expended filter cartridges will be strapped together, and four groups of these filters will be placed in a process material canister. To replace the conservative estimate of fissile content, a nondestructive assay device is being developed to measure the fissile content. Once again, the thermal content will also be measured to assist in the storage strategy.

The storage scheme proposed for the process material canisters in the Argon Cell Cooling Pits is shown in Fig. VI.14. The hardware for this storage scheme is currently being evaluated through an experimental program. Natural convective flow through the inner and outer channels passively cools the waste canisters. The system design criteria requires the stored process material to remain solid at all times.

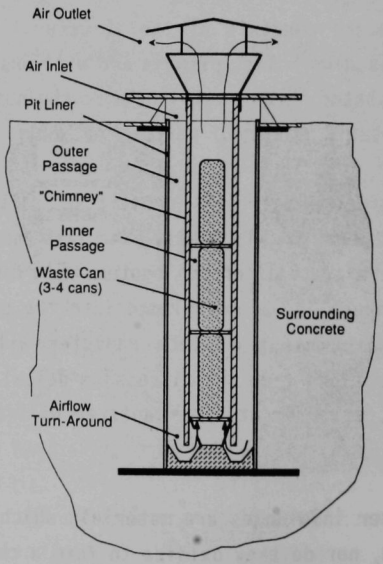

Fig. VI.14. Proposed Process Material Storage in Argon Cell Pits

The sizes of the process material canisters were determined through numerically modeling the proposed storage schemes. The thermal model was used to study various gap sizes, canister sizes, and thermal loads. The results of the analysis indicate two different canister sizes should be used. The first canister is 4.5 in. in diameter and will be used for the higher thermal loadings (cadmium). The second canister is 7.0 in. in diameter and will be used for lower thermal content process materials (salt). Both canisters will be 29.5 in. in length.

Initially, if the thermal loadings are greater than the allowable limits for the Argon Cell storage pits, the process material will be stored in racks above the floor within the Argon Cell. Once the thermal loadings have decreased to an acceptable limit (determined by a thermal model and an experiment), the canisters may be stored in the Argon Cell pits. The thermal loadings will decay over time and finally reach an acceptable level to allow removal from the Argon Cell pits. After removal, the canisters will be transferred to RSWF until process equipment has been developed to remove the remaining actinides.

E. Process Control and Accountability

The automation of the process equipment will be carried out through a distributed control system. The distributed control system approach allows separate central processing units to perform different tasks, while they are interconnected to other central processing units over a data network.

Programmable logic controllers (PLCs) are the primary interface between the process equipment and the overall control system. The operator control stations (OCSs) are used by the operating technicians to control and monitor all important process parameters. All normal control functions will occur through the use of the OCSs.

The mass tracking system (MTG) performs a variety of functions, including materials control and accountability, criticality safety specifications, etc. The PLCs, OCSs, and the MTG will be interconnected on a network to allow communications between the different levels of the control system.

Throughout the year, programmers were trained at Allen-Bradley to learn how to effectively use the programmable logic controllers (PLCs).

The majority of the PLC's and the input/output modules for the electrorefiner, cathode processor, welder, and air cell process equipment were received in January 1990, completing the PLC contract. This equipment was used for programming and system checkout. The equipment and operating system software for the operator control stations underwent a bid and review process. The contract was awarded in August, and the first equipment was received in September. All of the OCS hardware and software was received in 1990, and development of control screens for the element chopper, pin processor, and casting furnace is in progress.

For the fuel element chopper, initial programming of the PLC was completed by August. Programming the OCS started and continued through the year. Startup and debugging of the control system for the fuel element chopper started in November. In parallel, the Software System Design Description (SSDD) was prepared and a final software design review was held in December.

A three phase procedure was written to checkout the PLC cabinet for the cathode processor. The three phases are outlined here: Phase I--inspection and cold checks; Phase II--for energizing selected components; Phase III--PLC simulation checkout. By August, Phase I and Phase II testing was successfully completed. In August, a separate procedure for Phase III was written to check the manual mode of the PLC program for monitoring in-cell and out-of-cell equipment. A review of the SSDD for the cathode processor was also held in December.

Initial checkout of the PLC control system for the pin processor started in September. Software development had been an ongoing effort throughout the year. A review of the SSDD was held for the pin processor in December.

Work was conducted to establish a database for the Material Tracking (MTG) System. A prototype system was developed to test ideas and the full range of software components for MTG system. A Software SDD was prepared for the first phase of the Final Design Review, which was held in September. By December, much

of the programming was completed for the MTG task of checking zone-to-zone transfers and container-to-container transfers against a set of criticality safety rules. Development work began on a method to control the barcode readers and balances from either the MTG computers or the OCSs.

Checkout of MTG-to-OCS communications started when the OCSs were received at ANL-W in September. Five of the OCSs were installed and networked to the MTG computer. Testing showed the MTG could successfully interface with an OCS. This connection is the data transmission link between the OCS and the MTG. OCS-to-PLC communications had been verified earlier.

VII. LIQUID METAL REACTOR TECHNOLOGY RESEARCH AND DEVELOPMENT

A. ALMR Electromagnetic Pump Development

The current ALMR concept being developed by General Electric requires that several large electromagnetic (EM) pumps operate submerged in the reactor vessel to pump the primary system sodium. These pumps are designed to operate without an active cooling system relying instead on the pumped and surrounding sodium to remove internally generated heat. The electrical windings of these self-cooled annular linear induction pumps were estimated to reach temperatures near (538°C) 1000°F. Conventional high voltage coil winding insulation is limited to about 200°C. An insulation system for an EM pump is required that can operate continuously at 538°C for 40 years at 1000 volts A.C., and be commercially available. This insulation system is very sensitive to total insulation thickness, voltage gradient, and mechanical effects (e.g., vibrations) that may cause cracking. A program to develop this insulation system has been in progress since 1985. The program has consisted of the following components:

a) Small bar sample tests for materials evaluations,
b) Oven tests on prototypic EM pump coils, and
c) Prototypic testing of a full diameter-1/4 length EM pump.

Early work centered on the screening of materials by oven testing small bar samples at or beyond the operating temperature and voltage (see Fig. VII.1). As a result of the bar sample tests several promising materials including woven fiberglass-reinforced mica tape and woven ceramic fiber tape were selected. The glass/mica tape was selected for further testing for space and cost reasons. A test program was initiated to determine the estimated lifetime of the glass/mica tape insulation by accelerating the chemical aging of bar samples with the application of over-temperature at voltage. The lifetime at normal operating temperature can be determined by running selected higher temperature accelerated aging tests to failure and using the Arrhenius Principle to predict the lifetime at 538°C.

The thickness of the insulation has been established at about 1.9 mm (0.075 in.). This insulation thickness is a trade-off between an acceptably low

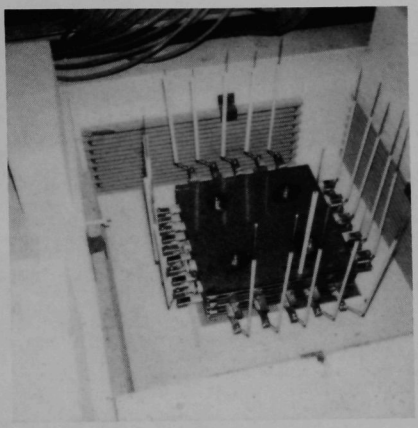

(a)

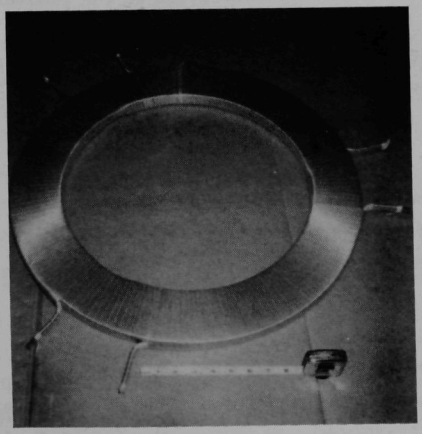

(b)

Fig. VII.1. (a) Photograph of Bar Sample Test
(b) Photograph of Prototypic EM Pump Coil

voltage gradient and adequate heat transfer from the high temperature pump windings to the cooler magnetic iron stator. Mica generally has a poor thermal conductivity. Both bonded and unbonded glass/mica tape layers have been studied. Binders such as mono-aluminum phosphate and ceramic cements have shown acceptable electrical performance. The binders are applied to the tape by brush as the tape is wrapped on the bar sample with up to 15 tape layers on straight test bars of copper. Due to the large water content of these binders care has been taken to slowly heat the insulated bar to remove the water before applying significant voltage to the bar samples. After this curing operation, samples are tested at 680-750°C and a voltage of 1500-2500 volts at 60 Hz applied between the copper bar and an external electrode. Data on the leakage current through the insulation is taken and the time-to-failure recorded. The times-to-failure have extended from a few hundred hours to over 40,000 hours. Based upon the high temperature accelerated aging tests of the bar samples the estimated lifetime at 538°C is estimated to be in excess of 100 years.

The technique was next applied to prototypic EM pump coils having shown the feasibility of glass/mica tape insulation on bar samples. Figure VII.2 shows four small ovens used for testing bar samples and four large ovens used for testing the large prototypic pump coils (see Fig. VII.1). The large size EM pump coils are prototypic of planned ALMR pumps and are about 58.4 cm (23. in.) OD, 40.6 cm (16 in.) ID, and 2.54 cm (1.0-in.) thick. A series of coils were insulated using glass/mica tape and binders of mono-aluminum phosphate and ceramic cement. These coils were tested at both ultra-high temperature (730°C) and at near normal operating temperature (550°C). The results showed that the insulation system tended to crack at the ultra-high temperature but performed satisfactorily at normal temperature.

Oven testing of both bar samples and prototypic coils addressed the chemical effects of high temperature and voltage on the materials but did not address the mechanical stresses imposed on the materials in an actual EM pump. For this reason the General Electric Company designed and built a stator segment test article EM pump which would provide the mechanical stress conditions expected in an ALMR. The test article EM pump was 1/4 the length of a prototypic pump but of full-diameter. The pump was tested in a sodium test facility

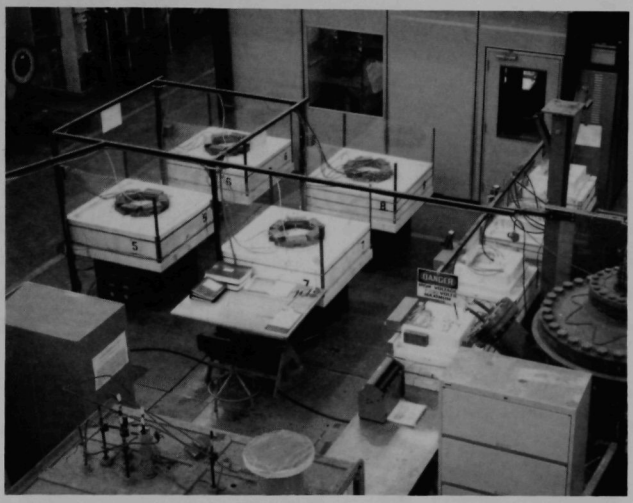

Fig. VII.2. Full Size Coil and Bar Sample Test Ovens

constructed of 50.8 cm (2-in.) diameter pipe at ANL-E. The pump operated at prototypic current density and magnetic flux density; subsequently, each of the 24 coils in the pump was subjected to the proper electrical, thermal, and mechanical stresses. Figure VII.3 shows the stator segment test article EM pump. Unlike conventional annular linear induction pumps, the coils of this pump can be easily replaced. The initial coils were insulated with unbonded glass/mica tape. A test of 2047 hours between August 1988 and March 1989 showed that this unbonded insulation system was unsatisfactory due to shrinkage. This resulted in loosening of the coils in the pump stator and subsequent coil vibration, insulation abrasion, and coil failure. Shrinkage was caused by the loss of the fiberglass woven backing for the mica at temperatures higher than normally allowable for fiberglass.

The pump was re-built with a second set of coils. These coils were insulated at ANL with glass/mica tape bonded with a ceramic cement which does not shrink at high temperature. Earlier ANL oven tests had confirmed the good electrical performance and stability of the ceramic cement bonded coils. The

Fig. VII.3. Stator Segment Test Article Pump

ceramic cement is applied to fill all the voids in the open fiberglass woven fabric backing of the tape. When cured and operated at high temperature the fiberglass deteriorates but the multi-layered tape structure remains intact due to the solid ceramic cement. Other improvements were made to the pump including additional ground fault insulation and better radial and axial clamping arrangements to reduce stator vibrations. All the work related to these pump modifications was performed by ANL with GE consultation.

The test of the modified pump started in July 1989 on a 24-hour per day, 5-day per week schedule. With the exception of two visual examinations of the stator, this schedule was continued through March 1990 with a total accumulation of 3611 hours of operation. There was no evidence of any electrical fault or malfunction during this time. The ground leakage current, an important measure of coil performance, did not vary indicating no observable aging effects. Visual examinations also showed no significant deterioration of the insulation. Some loosening of the radial clamping bands was observed but pump vibrations were minimal. Due to the magnetic saturation of the stator iron, the windings could not be operated above 900°F. The weekly schedule of pump operation required a temperature cycle once per week between 200°C and 482°C (400 and 900°F) with a total of 33 thermal cycles over the testing period. The severe thermal cycling (33 cycles) represented a very significant mechanical stressing of the pump. These tests have successfully demonstrated the feasibility of fully developing a high temperature electromatic pump without an active cooling system.

B. RVACS Experiments

Using a naturally circulating air stream to remove shutdown decay heat from a nuclear reactor vessel is a key feature of the advanced liquid metal reactor (ALMR). This decay heat removal scheme has been called the Reactor Vessel Air Cooling System (RVACS). The RVACS method of shutdown heat removal employs a totally passive cooling system that rejects heat from the reactor containment (guard) vessel by natural convection and by radiation to air. The system is inherently very reliable since it is not subject to failure modes associated with active decay cooling systems. The RVACS is designed to assure adequate cooling of the reactor in the event of loss of decay heat removal from all other heat transfer paths.

Although calculations indicated the viability of this air-cooled shutdown heat removal method, uncertainties remained with respect to particular designs. In addition, the effects of changing environmental conditions and material properties on the performance of the RVACS system were not clearly understood. These uncertainties prompted the design, and fabrication of the Natural Convection Shutdown Heat Removal Test Facility (NSTF) at ANL. The facility can simulate the air-side, full-scale performance of a segment of either the General Electric/PRISM or Rockwell International/SAFR reactor systems.

Facility Description

The basic assembly configuration of the NSTF[1] consisting of an inlet section followed by a heated zone and an unheated stack or chimney is illustrated in Fig. VII.4. All sections, except the inlet, are thermally insulated to hold parasitic heat losses to 2% or less. The heated zone flow channel measures

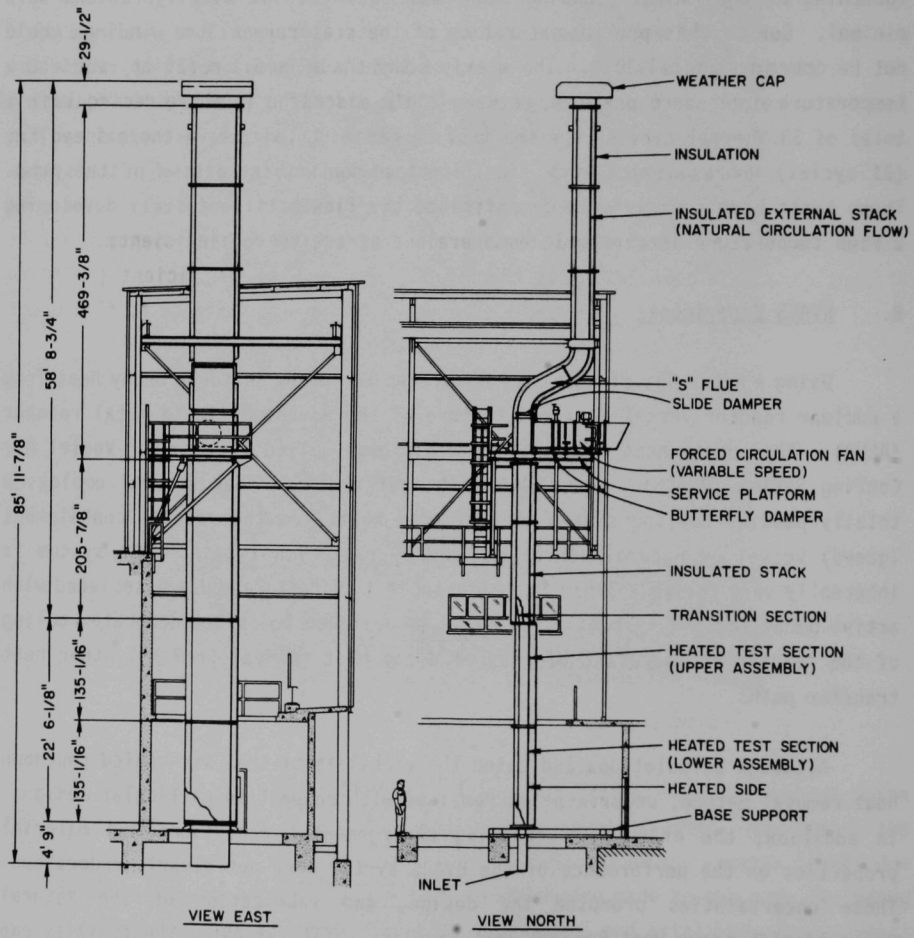

Fig. VII.4. Basic Configuration of the Natural Convection Shutdown Heat Removal Test Facility at ANL-W

1.32 m (52 in.) x 0.304 m (12 in.) in cross section and is 6.7 m (22 ft) tall. Figure VII.5 shows a cross section of the heated zone. Provision is made to expand the 0.304 m dimension up to 0.456 m (18 in.) or reduce it to any desired value.

Above the heated zone the flow channel expands to 1.52 m (60 in.) x 0.456 m (18 in.) and two flow paths are provided. The main path for the experiments is upward through an "S" curve and then vertically through the building roof. This provides a stack for natural convection nearly 17.9 m (58-3/4 ft) in vertical length. The top of the stack is 6.1 m (20 ft) above the roof; this height was chosen to ensure that the discharge is above recirculating winds caused by the building. The second flow path contains a variable speed fan and damper. This feature is provided for forced convection tests when the system is at very low temperature and a controlled air flow rate is desired. The open system was designed with a very low overall pressure loss coefficient; K = 1.5. The pressure loss coefficient is the overall system loss coefficient (inlet to exit) in terms of velocity head at the inlet. Variable resistance to flow under

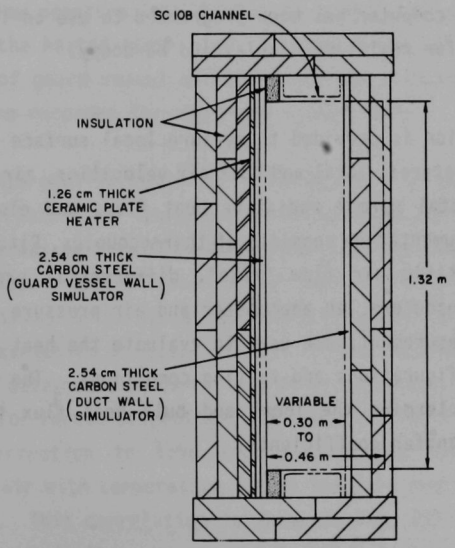

Fig. VII.5. Cross Section of the Heated Zone of the ANL NSTF Assembly

natural circulation conditions can be investigated by using various orifice plates inserted in the slide damper. The guard wall and duct wall simulator surfaces are smooth carbon steel plates 2.54 cm (1 in.) thick.

Heat input to the simulated guard vessel wall is provided by an assembly of electrical heaters that are fastened to a 0.635 cm (0.25 in.) stainless steel plate. Heat is transferred through the plate and then radiated/conducted across a small air gap to the simulated guard vessel surface. Power to the heaters is computer controlled based either on signals from system thermocouples or from prescribed power demand (uniform heat flux) setting. In general, the system operates in either one of two thermal modes: (1) constant (uniform) guard vessel wall temperature to 650°C (1200°F) or (2) constant (uniform) heat flux to 21.5 kW/m^2 (2.0 kW/ft^2). In addition, the system accommodates stepwise variation of either mode singly or in combination.

The data acquisition system (DAS) is capable of sampling 300 channels, most of which are dedicated to thermocouples located in the heated zone. The DAS stores all its data on disk and selected channels may also be displayed on CRTs and hardcopy. The computer has been programmed to use on-line data to compute system parameters for real-time display and hardcopy.

Instrumentation is provided to measure local surface temperatures, local and bulk air temperatures, local and bulk air velocities, air volumetric and mass flow rates, the total normal radiative heat flux, and electric power to the heaters. The instrumentation consists of thermocouples, Pitot-static traversing probes, a Pitot-static air flow "rake", differential pressure transducers, radiation flux transducers, an anemometer and air pressure and humidity gages. Data from these measurements are used to evaluate the heat removal performance for particular configurations and testing conditions. The primary measurement objective is to determine the local and bulk heat flux transport rates and associated heat transfer coefficients.

Experimental Results

During the course of the experimental test program a total of 71 equilibrium runs for the open channel (PRISM design) and 41 equilibrium runs for the finned channel (SAFR design) were performed. The open channel runs were analyzed to extract convection heat transfer coefficients. Heat transfer coefficients were not extracted for the finned channel runs due to the added complexity of the radiation heat transfer term in the total heat balances among the various heat transfer surfaces. The overall performance, however, improved with the addition of the fins. Specifically, the guard vessel temperature was reduced by 83°C (150°F) at a power level of 10.8 kW/m^2 (1 kW/ft^2) and an overall loss coefficient K of 10.

For the open channel runs, the power was varied up to approximately 16 kW/m^2 (1.5 kW/ft^2) and the pressure loss coefficient was varied from 1.5 to 20. Inlet velocities for the system as high as 5.2 m/s (17 ft/sec) were recorded for the high power input, low loss coefficient runs. The high values of velocity were due primarily to the very large vertical height of the chimney. The chimney presented a very low pressure loss due to its larger equivalent diameter. The total height of the heated riser plus the chimney was of the order of 26.2 m (86 ft). Values of guard vessel surface temperature as high as approximately 650°C (1200°F) were recorded for the higher power runs.

For each of the equilibrium runs, it was possible to extract the convection heat transfer coefficient for the guard vessel wall and the duct wall. The data conversion process was performed by a computer program that essentially solved the steady state heat transfer equations for both radiation and convection for the various heat transfer surfaces and the flowing air stream. It was noted during the data extraction process that all of the runs were in the turbulent range and that the data could be correlated by an equation similar to the Dittus-Boelter[2] equation for forced convection heat transfer with a correction for inlet effects and a correction to take into account the variation in physical properties of the air with temperature across the film next to the wall for high wall temperatures. This correlation is shown in Fig. VII.6. The data for the 71 equilibrium runs over the experimental Reynolds Number range correlates as:

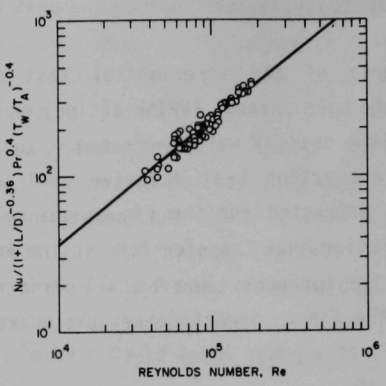

Fig. VII.6. Heat Transfer Correlation for the NSTF Data

$$Nu = 0.0229\left[1+\left(\frac{L}{D}\right)^{-0.36}\right]Re^{0.8}Pr^{0.4}\left(\frac{T_w}{T_a}\right)^{-0.4} \quad (1)$$

where the Nusselt (Nu), Reynolds (Re), and Prandtl (Pr) Numbers are evaluated at the local bulk air temperature. The ratio of the local absolute wall temperature, T_w, to the local air absolute temperature, T_a, is used to account for the large range of temperature differences encountered during the experiments. The negative value of 0.4 for the exponent on the temperature ratio term was suggested by Barnes and Jackson[3] as the value to be used for air. The range of Reynolds Number is 30,000 to 210,000 and the range of the L/D ratio (length to hydraulic diameter) is 0.56 to 13.35.

Application of Results to Reactor Systems

The air flow was in the turbulent range for the test runs and the system performance (i.e., flow rates vs. power input) could be reasonably predicted using standard textbook equations. This result led to an investigation of RVACS design improvements through the use of roughened surfaces and the use of fins

and/or ribs on the air path surfaces to enhance the heat transfer performance for the case of turbulent air flow.

The impact of a number of design parameters on the performance of the RVACS system of a pool LMR was analyzed.[4] These parameters were: (a) the stack height, (b) the size of the air flow gap, (c) the system pressure loss, (d) fins on the guard vessel or the duct wall, and (e) the geometric roughness on the air flow channel walls. Reactor designs ranging from 400 MWth to 3500 MWth were considered. The peak sodium pool temperature during the transient following reactor scram from full power was used as a measure of RVACS system performance.

To identify the most promising of these parameters, a parametric study was first performed with a simple lumped parameter model. The most promising configuration determined from this study for the 3500 MWth design was analyzed further with the SASSYS code. The air flow gap size was found to affect the RVACS performance more strongly than variations in stack height or system pressure loss. A gap reduction from 0.152 to 0.0508 m (6 to 2 in.) reduced the peak sodium pool temperature by 25°C (45°F). Placement of fins on the guard vessel was more effective than placement of fins on the duct wall. Fins on the guard vessel reduced the peak sodium pool temperature by 85°C (153°F). Roughness on the air-flow channel walls, in the form of ribs, improved RVACS performance even further. Horizontal ribs having a height of 0.0032 m (0.125 in.) and a pitch of 0.0152 m (0.6 in.) gave the best performance. They reduced the sodium pool temperature by 110°C (198°F).

To obtain a more realistic measure of the improvement that can be achieved with the best ribbed configuration, its performance was also analyzed with the SASSYS code. The optimum ribbed configuration reduced the peak hot pool temperature and the peak cladding temperature by 52°C (94°F). The peak hot pool temperature was reduced from 735 to 683°C (1354 to 1261°F), and the peak cladding temperature was reduced from 741 to 689°C (1365 to 1272°F). Finally, the comparison of reactor sizes from 400 MWth to 3500 MWth showed that although the use of ribs improved the performance for all sizes, the improvement was less for the smaller sizes.

C. Seismic Isolation

From a seismic design point of view, there are significant differences between ALMR plant and LWR plants even though the seismic loads involved in the design of an ALMR plant are the same as those used in LWR plants. These differences are due to the distinguishing structural characteristic of ALMR plants in the use of thin-walled vessels and pipes as opposed to the thick-walled vessels and pipes used in LWR plants. Components and pipes in ALMR plants cannot accommodate the seismic loads as readily as comparable LWR components and pipes. As a result, considerable design effort and increased capital costs are required to specifically meet the seismic design requirements in the ALMR plants, particularly when the ground acceleration is high and the soil is stiff. To reduce the seismic loads, it is necessary that the plant layouts and structural designs be carefully planned so that fundamental frequency of structures lies outside the region of the most damaging earthquake frequencies. Furthermore, seismic analysis must be rigorously performed on ALMR components and pipes so that design conservatism is reduced. A seismically well designed ALMR plant not only saves capital costs, but also increases design margins for seismic events and thereby has a favorable impact on safety and risk.

In view of the sensitivity of the ALMR components, pipes, and structures to earthquake loads and the need to design future ALMRs to site conditions which have higher ground accelerations and higher shear wave velocities, it is necessary that new seismic design technology be developed so that the costs of ALMR plants can remain competitive with other energy sources. Due to recent developments in elastomer technology, seismic isolation using elastomer bearings is rapidly gaining acceptance as a design tool to enhance structural seismic margins and to protect people and equipment in aseismic-designed buildings in large magnitude seismic events. Seismically isolated structures transform the range of high-energy seismic input motions into low-frequency harmonic motions with significantly reduced accelerations. Thus, the use of seismic isolation has become an alternate strategy for U.S. ALMRs. It could lead to substantial savings in component and equipment design by filtering out high frequency seismic motions. It may also provide an economical means to increase design margins for seismic events. The application of this technology to ALMRs offers additional advantages over conventional seismic-hardening design. They are: (1) enhancement

of plant safety and reliability; (2) insensitivity to type of earthquakes; (3) potential cost-effectiveness; (4) protection of equipment investment; (5) permitting a standard design application to most available reactor sites; and (6) ability to cope with seismic design basis changes.

The goal of the ANL Seismic Isolation Program is to use base isolation as a new seismic design strategy for future ALMRs. The program has five elements: (1) to develop computer codes to simulate the response of isolator bearings and to evaluate the seismic response of isolated structures; (2) to develop an experimental test program for isolator bearings; (3) to perform material testing on elastomer compounds; (4) to study the effects of long period ground motions on the response of base isolated structures; and (5) to study effects of aging, temperature and other environment service conditions on the performance of isolator bearings.

Development of Computer Codes

A three-dimensional finite element code is under development for analyzing the laminated elastomer bearings that are being considered for use in the ALMR plant seismic isolation system. The code can be used to optimize the design of isolators with respect to the thickness of the rubber and steel layers, the bearing mounting method, and aspect ratio. It can also be used to identify needed experiments to validate the bearing design and to provide realistic force-displacement relations for use in global modeling of seismically isolated reactor plants. New elements, nonlinear material laws, and solution algorithms are being incorporated into the NEPTUNE code[5] to provide proper representation of the laminated elastomer bearing subjected to seismic loadings. The code can be used to predict transient stress and strain within the elastomer, and to determine the ultimate strength of the elastomer to establish safety margins. Figure VII.7 illustrates the mathematical model of a steel plate laminated elastomer bearing.

In addition, a Seismic Isolation Evaluation Code (SISEC)[6] has been developed for analyzing the response of seismically isolated structures. It can be used to study the effects of basemat flexibility, spatial variation of ground motion, effects of long-period excitation, and the vertical response of the structure. It can also be used to study ground settlement effects, overturning

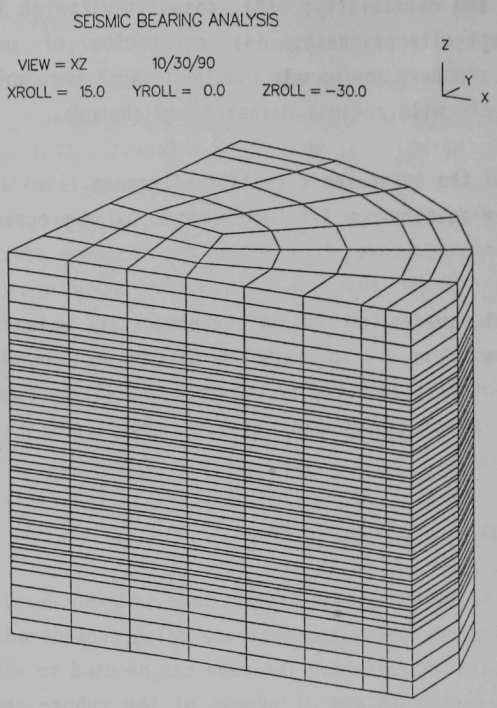

Fig. VII.7. Mathematical Model of Steel Plate Laminated Elastomer Bearing (only 1/4 of bearing is shown)

and liftoff effects, effects of seismic input at different elevations, effects of torsion, and effects of permanent displacements.

The shear stiffness of rubber decreases with increased shear strain. This reduction of shear stiffness has been observed experimentally. This effect must be taken into account in the mathematical modeling so that the response of elastomer bearings can be accurately predicted. The model used in the SISEC code for simulation of the behavior of isolator bearings is based upon the Simo and Taylor viscoelastic model.[7,8] This relation replicates many of the relevant features of typical isolation bearings in existence and can capture the softening effects of rubber in shear.

The constitutive relation assumes that the material is isotropic in both the original state and the deformed state. The volumetric response of the material is thus taken to be purely elastic, and damage or degradation of the material is only assumed in the shear (volume preserving) response. The degradation of the material is modeled by a function that depends on the strain history. This provides for the variation of material stiffness with increased strain. The degradation is also influenced by the conventional relaxation function.

The constitutive relation uses six parameters which can be derived from experimental data. Two of the parameters relate experimental storage and loss moduli of the material as a function of maximum strain. The two parameters deal with the short-term and the long-term shear moduli of the material and the last two parameters pertain to the time constant of the relaxation process and the fatness of the hysteresis loop.

The selected six parameters describe the response of the experimental data of the bearings quite well. An example of hysteresis loops due to sinusoidal loading for a bolted bearing determined experimentally is shown in Fig. VII.8. The corresponding analytical hysteresis loops with the appropriate values of parameters are provided in Fig. VII.9. As can be seen, the agreement between the two figures is quite good.

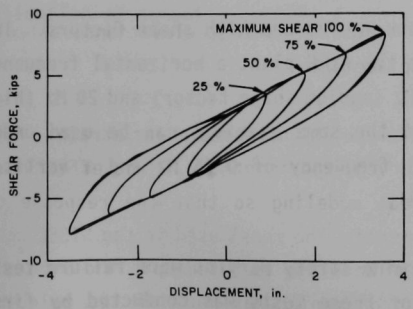

Fig. VII.8. Horizontal Shear Tests of Bolted Bearings, Axial Load = 208 kips

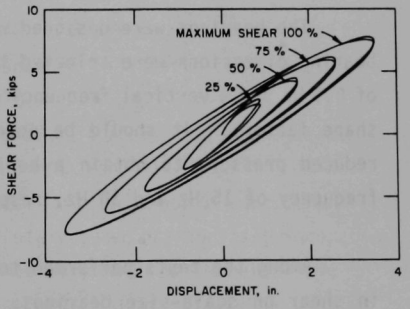

Fig. VII.9. Analytical Simulation of Horizontal Shear Tests

Experimental Test Program

An experimental test program was developed to establish the viability of using laminated elastomer bearings for base isolation of ALMR plants. The goal of the program is to determine the performance characteristics of laminated seismic isolation bearings under a wide range of loadings. Tests were performed on scale-size laminated seismic isolators and on small elastomer specimens (e.g., 2.54 cm (1 in.) x 2.54 cm (1 in.) x 0.5 cm (0.2 in.) elastomer pads). Tests were performed both within the design shear strain range to determine the response of the bearing under expected earthquake loading conditions and beyond the design range to determine failure modes and to establish safety margins.

The bearings tested consisted of a solid cylinder composed of alternate layers of elastomer and thin steel shims. The top and bottom ends of the bearing consist of thick steel plates. The method of connecting the bearings to the structures was investigated. Two types of connections were considered: dowel- and bolted-type. In the dowel-type connection, mounting plates containing dowel pins were bolted to the structure and the foundation. The dowel pins fit inside dowel holes located in end plates of the bearing. This design tends to minimize the occurrence of tension in the elastomer, but allows the bearing to roll out under large displacements. In the bolted-type connection, the mounting plates were bolted to the bearing, the structure and the foundation. Tensile stresses can develop in certain regions of the bearing, but the bearing cannot roll out.

The bearings were designed with both medium and high shape factors. The bearing dimensions were selected to give the ALMR plant a horizontal frequency of 0.5 Hz and a vertical frequency of 10 Hz (medium shape factor) and 20 Hz (high shape factor). It should be noted that the same bearings can be used under reduced pressure to obtain a horizontal frequency of 0.75 Hz and a vertical frequency of 15 Hz and 30 Hz, respectively.

Among the tests performed to determine safety margins were failure tests in shear on scale-size bearings. One of these tests was conducted by first applying an axial pressure of 6.9 MPa (1000 psi) and then shearing the bearing at a quasi-static shear strain rate to failure. Figures VII.10 and 11 show the deformed shape of the bearing during the test. Figure VII.11 shows the bearing

just prior to failure, which occurred at about 600% shear strain. The maximum design strain was 100%, which indicates a very high margin of safety.

Elastomer Specimen Tests

Testing of elastomeric specimens was performed at ANL to determine basic material properties: elastic constants, viscoelastic constants, damage parameters. The tests were conducted at strain ranges up to failure and at frequencies relevant to a seismic events. Shear tests on standard three-bar lap elastomer specimens were conducted using the INSTRON 8500 series testing machines. A computer program was developed to control the INSTRON machine tests. The program provides a sinusoidal loading to the elastomer and allows the user to specify the frequency, percent strain and number of load cycles.

A three-bar lap shear specimen (resembling a tuning fork configuration) was subjected to a series of sinusoidal displacements, as shown in Fig. VII.12. Figures VII.13 and VII.14 show the average value for the shear modulus, G, and the damping, characterized by tan δ, for each series of three cycles. The results show that the shear modulus decreases and the damping increases during cycling.

The results of the bearing tests and the elastomer specimen tests will contribute to the establishment of the data base needed for bearing design and validation of computer models.

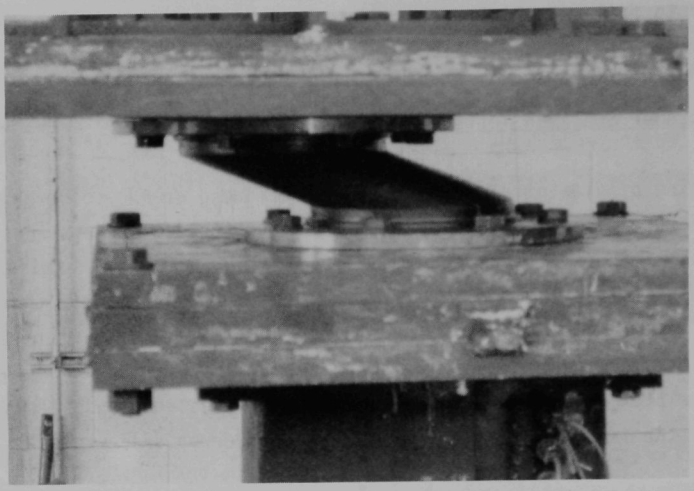

Fig. VII.10. Deformed Shape of Laminated Isolation Bearing at about 280% Shear Strain

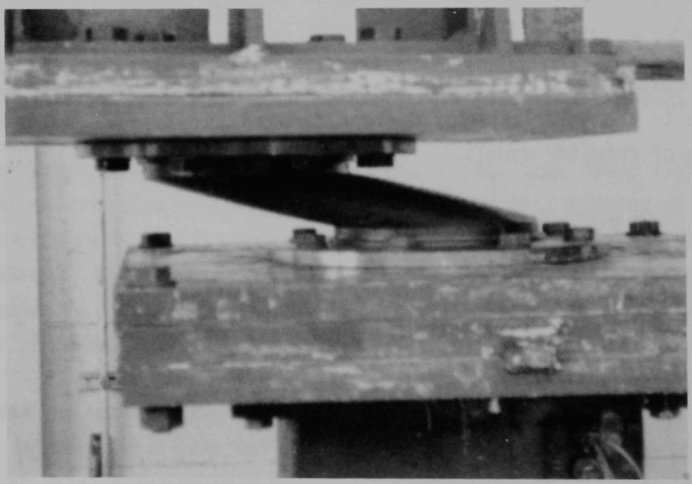

Fig. VII.11. Deformed Shape of Laminated Isolation Bearing Just Prior to Failure (approximately 600% shear strain)

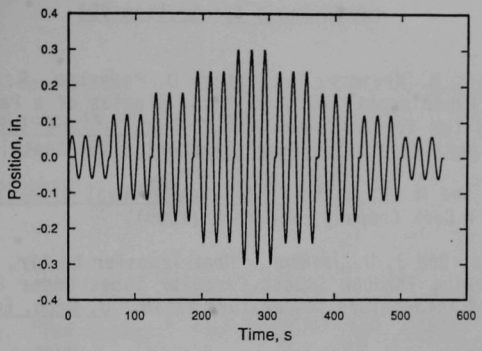

Fig. VII.12. Prescribed Series of Sinusoidal Displacements

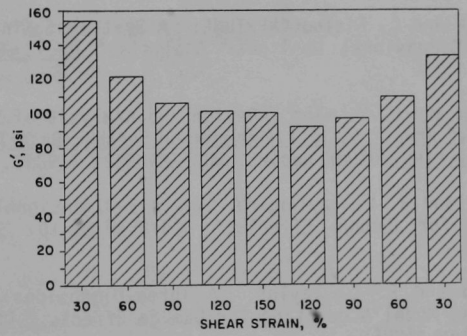

Fig. VII.13. Average Value of Shear Modulus

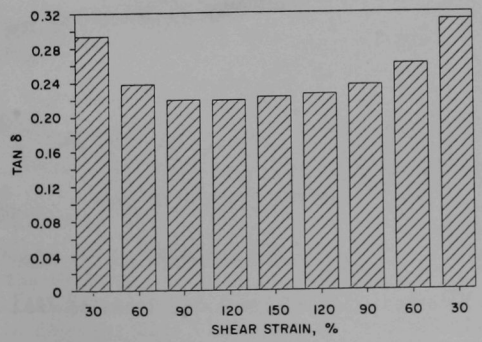

Fig. VII.14. Average Value of Damping

References for Section VII

1. J. Heineman, M. Kraimer, P. Lottes, D. Pedersen, R. Stewart, and J. H. Tessier, "Experimental and Analytical Studies of a Passive Shutdown Heat Removal System for Advanced LMRs," Proc. of the Intl. Topical Mtg. on Safety of Next Generation Power Reactors, 715, Seattle, WA (1988).

2. F. Kreith and M. S. Bohn, Principles of Heat Transfer, Second Edition, McGraw-Hill Book Company, New York (1986).

3. J. F. Barnes and J. D. Jackson, "Heat Transfer to Air, Carbon Dioxide, and Helium Flowing Through Smooth Circular Tubes Under Conditions of Large Surface/Gas Temperature Temperature Ratio," J. Mech. Eng. Sci., 3, 4, 303, (1961).

4. C. P. Tzanos, J. H. Tessier and D. R. Pedersen, "An Investigation of RVACS Design Improvements," Fifth Proc. of Nuclear Thermal Hydraulics, 58, San Francisco, CA (November 26-30, 1989).

5. R. F. Kulak and C. Fiala, "NEPTUNE: A System of Finite Element Programs for Three-Dimensional Nonlinear Analysis," Nucl. Eng. & Des., 106:47 (1988).

6. R. F. Kulak and C. Y. Wang, "Design and Analysis of Seismically Isolated Structures," Proc. 1st Intl. Seminar on Seismic Base Isolation for Nuclear Power Facilities, USDOE Report, CONF-8908221 (1989).

7. J. C. Simo and R. L. Taylor, "A Simple 3-Dimensional Viscoelastic Model Accounting for Damage Effects," UCB/SESM/83-10, SESM, U.C. Berkeley (1983).

8. J. C. Simo and R. L. Taylor, "A Three-Dimensional Finite Deformation Viscoelastic Model Accounting for Damage Effects," UCB/SESM/85-02, SESM, U.C. Berkeley (1985).

VIII. LIST OF PUBLICATIONS

The technical papers on the IFR Program activities, which have been published through the end of FY 1990 are listed below. The publications are categorized into the following subject areas: IFR Concept, Metal Fuel Performance, Pyroprocessing, Safety, Neutronics and Core Design, and Fuel Cycle Demonstration.

IFR Concept

1. Y. I. Chang, "The Integral Fast Reactor Fuel Cycle," Trans. Am. Nucl. Soc., 90:73 (1990).

2. Y. I. Chang, "The Total Nuclear Power Solution," The World and I, 288 (April 1991).

3. Y. I. Chang, "Use of Fast-Spectrum Reactors for Actinide Burning," First MIT Intl. Conf. on the Next Generation of Nuclear Power Technology, Cambridge, MA (October 4-5, 1990).

4. Y. I. Chang and C. E. Till, "Actinide Recycle Potential in the Integral Fast Reactor (IFR) Fuel Cycle," LMR: A Decade of LMR Progress and Promise, American Nuclear Society, La Grange Park, IL, 129 (November 1990).

5. Y. I. Chang and C. E. Till, "Advanced Breeder Cycle Uses Metallic Fuel," Modern Power Systems, 59 (April 1991).

6. Y. I. Chang and C. E. Till, "Economic Prospects of the Integral Fast Reactor (IFR) Fuel Cycle," to be presented at the Intl. Conf. on Fast Reactors and Related Fuel Cycles, Kyoto, Japan (October 28-November 1, 1991).

7. C. E. Till and Y. I. Chang, "Progress and Status of the Integral Fast Reactor (IFR) Fuel Cycle Development," to be presented at the Intl. Conf. on Fast Reactors and Related Fuel Cycles, Kyoto, Japan (October 28-November 1, 1991).

Metal Fuel Performance

1. G. L. Batte', "Safety Assessment of the Fuel Manufacturing Furnace," to be presented at the Intl. Conf. on Nuclear Criticality Safety, Oxford, England (September 9-13, 1991).

2. G. L. Batte' and G. L. Hofman, "Run-Beyond-Cladding Breach (RBCB) Test Results for the Integral Fast Reactor (IFR) Metallic Fuel Program," Proc. of the Intl. Fast Reactor Safety Meeting, IV:207, Snowbird, UT (August 12-16, 1990).

Metal Fuel Performance (Contd.)

3. G. L. Batte', R. G. Pahl, and G. L. Hofman, "Current Status of the Run-beyond-Cladding Breach (RBCB) Tests for the Integral Fast Reactor (IFR) Metallic Fuels Program," Nucl. Tech., in press (1990).

4. S. P. Henslee, C. E. Lahm, and D. L. Porter, "Fabrication of LMR Metallic Fuel Containing Minor Actinide Additions," to be presented at the Intl. Conf. on Fast Reactors and Related Fuel Cycles, Kyoto, Japan (October 28-November 1, 1991).

5. G. L. Hofman, R. G. Pahl, C. E. Lahm, and D. L. Porter, "Swelling Behavior of U-Pu-Zr Fuel," Metall. Trans. A, **21A**:517 (March 1990).

6. C. E. Lahm, J. F. Koenig, and B. R. Seidel, "Consequences of Metallic Fuel-Cladding Liquid Phase Attack During Over-temperature Transient on Fuel Element Lifetime," Proc. of the Intl. Fast Reactor Safety Meeting, **IV**:139, Snowbird, UT (August 12-16, 1990).

7. L. Leibowitz, R. Blomquist, and A. D. Pelton, "Thermodynamics and Phase Equlibria of the Plutonium and Uranium System," J. Nucl. Mat., in press (1990).

8. R. G. Pahl, C. E. Lahm, H. Tsai, and M. C. Billone, "Irradiation Experience with HT9-Clad Metallic Fuel," to be presented at the Intl. Conf. on Fast Reactors and Related Fuel Cycles, Kyoto, Japan (October 28-November 1, 1991).

9. R. G. Pahl, D. L. Porter, C. E. Lahm, and G. L. Hudman, "Experimental Studies of U-Pu-Zr Fast Reactor Fuel Pins in the Experimental Breeder Reactor II," Metall. Trans. A, **21A**:1863 (July 1990).

10. R. G. Pahl, G. L. Batte', R. Makaili, J. D. B. Lambert, and G. L. Hofman, "The Characterization and Monitoring of Metallic Fuel Breaches," to be presented at the Intl. Conf. on Fast Reactors and Related Fuel Cycles, Kyoto, Japan (October 28-November 1, 1991).

11. R. G. Pahl, R. S. Wisner, M. C. Billone, and G. L. Hofman, "Steady-state Irradiation Testing of U-Pu-Zr Fuel to >18 at.% Burnup," Proc. of the Intl. Fast Reactor Safety Meeting, **IV**:129, Snowbird, UT (August 12-16, 1990).

12. D. R. Pedersen and B. R. Seidel, "A Status Report on the Integral Fast Reactor Fuels and Safety Program," Trans. Am. Nucl. Soc., **61**:300, Nashville, TN (June 1990).

13. D. R. Pedersen and B. R. Seidel, "The Safety Basis of the Integral Fast Reactor," J. Nucl. Safety, in press (1990).

14. D. L. Porter, C. E. Lahm, and R. G. Pahl, "Fuel Constituent Redistribution during the Early Stages of U-Pu-Zr Irradiation," Metall. Trans. A, **21A**:1871 (July 1990).

Metal Fuel Performance (Contd.)

15. B. R. Seidel and L. C. Walters, "A Decade of Advances in Metallic Fuel," Trans. Am. Nucl. Soc., 62:260, Washington, DC (November 11-15, 1990).

16. B. R. Seidel, G. L. Batte', N. E. Dodds, C. E. Lahm, R. G. Pahl, and H. Tsai, "Recent Progress in the Development of Metallic Fuel," Proc. of ANS Topical Meeting on Safety, Status, and Future of Non-commercial Reactors and Irradiation Facilities, Boise, ID, 359 (September 30-October 4, 1990).

17. B. R. Seidel, G. L. Batte', N. E. Dodds, G. L. Hofman, C. E. Lahm, R. G. Pahl, D. L. Porter, H. Tsai, and L. C. Walters, "A Decade of Advances in Metallic Fuel," LMR: A Decade of LMR Progress and Promise, American Nuclear Society, La Grange Park, IL, 196 (November 1990).

18. H. Tsai, "Fuel/Cladding Compatibility in Irradiated Metallic Fuel Pins at Elevated Temperatures," Proc. of the Intl. Fast Reactor Safety Meeting, **IV**:257, Snowbird, UT (August 12-16, 1990).

19. H. Tsai, Y. Y. Liu, D. Wang, and J. M. Kramer, "Behavior of Low-burnup Metallic Fuels for the Integral Fast Reactor at Elevated Temperature in Ex-reactor Tests," to be presented at the Intl. Conf. on Fast Reactors and Related Fuel Cycles, Kyoto, Japan (October 28-November 1, 1991).

20. L. R. Zirker, C. L. Tsai, and D. C. Hall, "Fabrication of Oxide Dispersion Strengthened Ferritic Clad Fuel Pins," to be presented at the Intl. Conf. on Fast Reactors and Related Fuel Cycles, Kyoto, Japan (October 28-November 1, 1991).

Pyroprocessing

1. T. R. Johnson, M. A. Lewis, and D. F. Fischer, "Treatment of Wastes from Fuel Cycle of Integral Fast Reactor," Waste Management Research Abstracts, IAEA, Issue No. 20 (1990).

2. M. A. Lewis and T. R. Johnson, "A Study of the Thermodynamic and Reducing Properties of Lithium in Cadmium at 773 K," J. Electrochem. Soc., 137(5), 1414 (May 1990).

3. J. R. Liaw and J. P. Ackerman, "PYRO-New Capability for Isotopic Mass Tracking in Pyroprocess Simulation," Intl. Conf. on the Physics of Reactors: Operation, Design, and Computation, Marseille, France, 2:XI-33 (April 23-27, 1990).

Safety

1. T. H. Bauer, A. E. Wright, W. R. Robinson, J. W. Holland, and E. A. Rhodes, "Behavior of Modern Metallic Fuel in TREAT Transient Overpower Tests," Nucl. Tech., 92:325 (1990).

2. E. E. Gruber and J. M. Kramer, "Gas-Bubble Growth Mechanisms in the Analysis of Metal Fuel Swelling," Radiation-Induced Changes in Microstructure, ASTM STP 955, 1:432 (1987).

3. E. E. Gruber and J. M. Kramer, "Modeling of Fission-Gas Behavior in Metallic Fuels," J. Am. Ceram. Soc., 70(10):699 (1987).

4. J. M. Kramer and T. H. Bauer, "Fuel Damage during Off-Normal Transients in Metal-Fueled Fast Reactors," Proc. of the Intl. Fast Reactor Safety Meeting, IV:145, Snowbird, UT (August 12-16, 1990).

5. Y. Y. Liu, et al., "Whole-pin Furnace System: An Experimental Facility for Studying Irradiated Fuel Pin Behavior under Potential Reactor Accident Conditions," Proc. of the Intl. Fast Reactor Safety Meeting, I:491, Snowbird, UT (August 12-16, 1990).

6. J. A. Morman, P. H. Froehle, J. W. Holland, and J. D. Bennett, "Tomographic Imaging of Severely Disrupted Fuel Assemblies Tested in TREAT," Proc. of the Intl. Fast Reactor Safety Meeting, I:441, Snowbird, UT (August 12-16, 1990).

7. C. J. Mueller et al., "A Risk Characterization of Safety Research Areas for Integral Fast Reactor Program Planning," Nucl. Tech., 91:226 (1990).

8. C. J. Mueller and J. M. Kramer, "Cladding Failure Probability Modeling for Risk Evaluations in Fast Reactors," Res Mechanica, 24:1 (1988).

9. D. R. Pedersen et al., "Overview of Fast Reactor Safety Research and Development in the USA Since Guernsey," Proc. of the Intl. Fast Reactor Safety Meeting, I:1, Snowbird, UT, (August 12-16, 1990).

10. D. R. Pedersen and B. R. Seidel, "A Status Report on the Integral Fast Reactor Fuels and Safety Programs," Proc. ANS Annual Meeting, 61:300 Nashville, TN (June 10-14, 1990).

11. H. Tsai, "Fuel/Cladding Compatibility in Irradiated Metallic Fuel Pins at Elevated Temperature," Proc. of the Intl. Fast Reactor Safety Meeting, II:257, Snowbird, UT (August 12-16, 1990).

12. C. P. Tzanos and D. R. Pedersen, "Analysis of A DRACS Test for COMMIX Validation," Proc. of the Intl. Fast Reactor Safety Meeting, II:351, Snowbird, UT (August 12-16, 1990).

13. C. P. Tzanos and D. R. Pedersen, "Analysis of a DRACS Test for COMMIX Validation," Proc. ANS Annual Meeting, 61:448, Nashville, TN (June 10-14, 1990).

14. C. P. Tzanos and D. R. Pedersen, "Analysis of RVACS Test for COMMIX Validation," Nucl. Eng. Des., 121:59 (1990).

Neutronics and Core Design

1. J. E. Cahalan et al., "Performance of Metal and Oxide Fuels During Accidents in a Large Liquid Metal Cooled Reactor," Proc. of the Intl. Fast Reactor Safety Meeting, **IV**:73, Snowbird, UT (August 12-16, 1990).

2. J. E. Cahalan and T. Y. C. Wei, "Modeling Developments for the SAS4A and SASSYS Computer Codes," Proc. of the Intl. Fast Reactor Safety Meeting, **II**:123, Snowbird, UT (August 12-16, 1990).

3. E. Depiante and J. E. Meyer, "Light Water Reactor Thermal Hydraulics Modeling Using Parity Simulation," ENC '90 Poster Session Conf., Berne, Switzerland (September 23-26, 1990).

4. F. E. Dunn and J. P. Herzog, "Thermal-Hydraulic Impact of Failure of Slightly Irradiated Fuel Pins on LMR Passive Safety," Trans. Am. Nucl. Soc., 62:673, Washington, DC (November 11-15, 1990).

5. P. J. Finck, J. R. Deen, and J. L. Vujic, "Evaluation of MHTGR-NPR Computational Needs," DOE-RPIWG-ANL (July 1990).

6. E. K. Fujita and D. C. Wade, "The Neutronic and Fuel Cycle Performance of Interchangeable 3500 MWth Metal and Oxide Fueled LMRs," Intl. Conf. on the Physics of Reactors: Operation, Design and Computation, **I**:II.54, Marseilles, France (April 23-27, 1990).

7. K. N. Grimm and D. Meneghetti, "Power-Induced Power and Power-to-Flow Transfer Functions for EBR-II Subassemblies," Annals of Nuclear Energy, 17(4):173 (1990).

8. K. C. Gross, R. E. Hawkins, and W. K. Nickless, "Expert System for Delayed-Neutron Surveillance in LMRs," Presented at the 5th Annual Conf. on AI in the DOE Complex, Idaho Falls, ID (October 1990).

9. K. C. Gross, R. M. Singer, and K. E. Humenik, "Automated Surveillance of Reactor Coolant Pump Performance," to be presented at the Fourth Intl. Workshop on Main Coolant Pumps, Phoenix, AZ (April 16-19, 1991).

10. K. C. Gross, R. M. Singer, K. E. Humenik, and M. Walsh, "Expert System for Reactor Coolant Pump Surveillance," Proc. of the Intl. Fast Reactor Safety Meeting, **III**:359, Snowbird, UT (August 12-16, 1990).

11. K. C. Gross, R. V. Strain, and J. D. B. Lambert, "Analysis of Fission-Product Release Mechanisms Using Bifrequency Reactivity-Oscillation Tests in EBR-II," Proc. of the Intl. Fast Reactor Safety Meeting, **III**:197, Snowbird, UT (August 12-16, 1990).

12. R. N. Hill, "Hazard Quantification for LWR Spent Fuel," Presented at the Nuclear Energy Agency Committee on Reactor Physics Conference, NEACRP-A-1090, Paris, France (October 15-19, 1990).

13. R. N. Hill and H. S. Khalil, "An Evaluation of LMR Design Options for Reduction of Sodium Void Worth," Intl. Conf. on the Physics of Reactors: Operation, Design and Computation, **I**:II.19, Marseille, France (April 23-27, 1990).

Neutronics and Core Design (Contd.)

14. R. N. Hill, D. C. Wade, E. K. Fujita, and H. S. Khalil, "Physics Studies of Higher Actinide Consumption in an LMR," Intl. Conf. on the Physics of Reactors: Operation, Design and Computation, I:I.83, Marseilles, France (April 23-27, 1990).

15. K. E. Humenik and K. C. Gross, "Sequential Probability Ratio Tests for Sensor Operability Surveillance in Nuclear Reactors," Proc. SIAM Conf. on Applied Probability in Science and Engineering, A22, New Orleans, LA (March 5-7, 1990).

16. K. E. Humenik and K. C. Gross, "Sequential Probability Ratio Tests for Reactor Signal Validation and Sensor Surveillance Applications," Nucl. Sci. and Engng., 105:383 (August 1990).

17. K. E. Humenik and K. C. Gross, "SPRTs for Reactor Signal Surveillance," presented at the IEEE Nucl. Sci. Symp., San Francisco, CA (January 15-19, 1990).

18. R. N. Hwang and E. M. Gelbard, "Resonance Computations for Cells with Fuel Annuli," Intl. Conf. on the Physics of Reactors: Operation, Design and Computation, II:IX.50, Marseilles, France (April 23-27, 1990).

19. L. C. Leal, R. N. Hwang, and C. N. Stenberg, "Computation of Multipole Parameter Using Preliminary ENDF/B-VI Data," Trans. Am. Nucl. Soc., 62:573 (November 11-15, 1990).

20. J. R. Liaw and J. P. Ackerman, "PYRO-New Capability for Isotopic Mass Tracking in Pyroprocess Simulation," Intl. Conf. on the Physics of Reactors: Operation, Design and Computation, II:XI.33, Marseilles, France (April 23-27, 1990).

21. J. T. Madell, E. M. Dean, D. Mohr, and T. C. Hung, "Dynamic Analysis of the EBR-II Plant with the DSNP-ND Simulation Package," Proc. ANS Intl. Topical Meeting on The Safety, Status and Future on Non-commercial Reactors and Irradiation Facilities, 2:705, Boise, ID (September 31-October 4, 1990).

22. D. Meneghetti and D. A. Kucera, "Delineations of Power, Power-to-Flow, and Inlet-Temperature Feedbacks of EBR-II," Ann. Nucl. Engy., 17(1):19 (January 1990).

23. D. Meneghetti and D. A. Kucera, "Feedback Components of a Pu-Fueled Compared to a U-Fueled 900 MWt LMR," Ann. Nucl. Engy., 17(7):353 (July 1990).

24. D. Meneghetti and D. A. Kucera, "Reactivity Feedback Components of a Homogeneous U10Zr-Fueled 900-MW (Thermal) Liquid-Metal Reactor," Nucl. Tech., 91:139 (August 1990).

Neutronics and Core Design (Contd.)

25. P. J. Persiani, R. G. Bucher, R. B. Pond, and R. J. Cornella, "Fuel Reprocessing Data Validation Using the Isotope Correlation Technique," Intl. Conf. on the Physics of Reactors: Operation, Design and Computation, II:XI-108, Marseilles, France (April 23-27, 1990).

26. J. Reifman, L. L. Briggs, and T. Y. C. Wei, "A First-Principles Generic Methodology for Representing the Knowledge Base of a Process Diagnostic Expert System," to be presented at the Fourth Intl. Conf. on Industrial and Engineering Applications of Artificial Intelligence and Expert Systems, Kauai, HI (June 2-5, 1991).

27. J. Reifman, L. L. Briggs, and T. Y. C. Wei, "Nuclear Power Plant Diagnostic Using Qualitative Analysis," submitted to the AI91: Frontiers in Innovative Computing for the Nuclear Industry, Jackson, WY (September 15-18, 1991).

28. R. M. Singer, K. C. Gross, and K. E. Humenik, "Pumping System Fault Detection and Diagnosis Utilizing Pattern Recognition and Fuzzy Inference Techniques," to be presented at the Fourth Intl. Conf. on Industrial and Engineering Applications of Artificial Intelligence and Expert Systems, Kauai, HI (June 2-5, 1991).

29. R. M. Singer, K. C. Gross, K. E. Humenik, and M. Walsh, "Reactor Coolant Pump Monitoring and Diagnostic System," Proc. 2nd Intl. Machinery Monitoring and Diagnostic Conf., 19, Los Angeles, CA (October 1990).

30. R. M. Singer, K. C. Gross, and R. W. King, "Advanced Condition Monitoring Techniques for Predictive Maintenance Applications," to be presented at the Intl. Conf. on Plant Life Extension, Berlin, Germany (December 2-4, 1991).

31. R. M. Singer, R. W. King, and J. Mott, "An Analysis Approach to Achieving Fault Tolerance in Nuclear Power Plant Sensors," Trans. Am. Nucl. Soc., 60:190, San Francisco, CA (November 26-30, 1989).

32. R. V. Strain, K. C. Gross, J. D. G. Lambert, and T. Odo, "Mixed-Oxide Fuel Pin Behavior During High-Temperature RBCB Operation in EBR-II," Proc. of the Intl. Fast Reactor Safety Meeting, IV:197, Snowbird, UT (August 12-16, 1990).

33. A. Tentner, Kalimullah, and K. Miles, "Analysis of Metal Fuel Transient Overpower Experiments with the SAS4A Accident Analysis Code," Proc. Intl. Fast Reactor Safety Meeting, III:141, Snowbird, UT (August 12-16, 1990).

34. R. B. Vilim, "A Measurement-based Method for Predicting Margin and Uncertainties for Unprotected Accidents in the Integral Fast Reactor Concept," Proc. of the Intl. Fast Reactor Safety Meeting, IV:289, Snowbird, UT (August 12-16, 1990).

35. R. B. Vilim, "The Passive Response of the Integral Fast Reactor Concept to the Chilled Inlet Accident," Proc. of the Intl. Fast Reactor Safety Meeting, III:89, Snowbird, UT (August 12-16, 1990).

Neutronics and Core Design (Contd.)

36. R. B. Vilim and H. P. Planchon, "Design of a Reactor Inlet Temperature Controller for EBR-II Using State Feedback," Proc. of the Intl. Fast Reactor Safety Meeting, III:309, Snowbird, UT (August 12-16, 1990).

37. J. L. Vujic and R. N. Blomquist, "Collision Probability Method in Arbitrary Geometries-Preliminary Results," Trans. Am. Nucl. Soc., 62:286, Washington, DC (November 11-15, 1990).

38. J. L. Vujic and W. R. Martin, "Solution of Two-dimensional Boltzmann Transport Equation on a Multiprocessor IBM 3090," Proc. of the 1990 ASME Intl. Computers in Engineering Conference and Exposition, 2:545, Boston, MA (August 5-9, 1990).

39. J. L. Vujic and W. R. Martin, "Two-dimensional Collision Probability Method with Anisotropic Scattering for Vector and Parallel Processing," Intl. Conf. on the Physics of Reactors: Operation, Design, and Computation, III:PIV.104, Marseille, France (April 23-27, 1990).

40. J. L. Vujic and W. R. Martin, "Vectorization and Parallelization of a Production Reactor Assembly Code, " Proc. of the Third Intl. Seminar on Finite Element and Allied Methods in Radiation Transport: Shielding, Reactor Physics and Geophysics Application, in press, London, UK (April 19-20, 1990).

41. A. M. White, "A Summary of the FLOWTRAN Code," ANL-FRA-166, Argonne National Laboratory Report (1990).

42. R. A. Wigeland et al., "Influence of Metal and Oxide Fuel Behavior on the ULOF Accident 3500 MW Heterogeneous LMR Cores and Comparison with Other Large Cores," Proc. Intl. Fast Reactor Safety Meeting, IV:83, Snowbird, UT (August 12-16, 1990).

43. R. A. Wigeland et al., "Performance of Metal and Oxide Fuels During Accidents in a Large Liquid Metal Cooled Reactor," Proc. Intl. Fast Reactor Safety Meeting, IV:83, Snowbird, UT (August 12-16, 1990).

44. W. S. Yang, P. J. Finck, and H. S. Khalil, "Reconstruction of Pin Burnup Characteristics from Nodal Calculations in Hexagonal Geometry, Proc. Intl. Conf. on the Physics of Reactors: Operation, Design and Computation, II:VIII.22, Marseille, France (April 23-27, 1990).

Fuel Cycle Demonstration

1. J. P. Bacca and E. K. Sherman, "An Improved Out-Cell Rapid Transfer System at the HFEF/South," Proc. of Remote Systems Technology Division, in press (1990).

2. J. C. Courtney, M. D. Carnes, C. C. Dwight, and R. J. Forrester, "Radiological Safety Modifications for the Demonstration Integral Fast Reactor Fuel Cycle Facility," Health Physics Journal, in press (1990).

3. J. C. Courtney and C. C. Dwight, "Radiation Shielding Design for a Hot Repair Facility," Health Physics Journal, in press (1990).